

ABSTRACT

FRACTURE NETWORKS AND MECHANICAL STRATIGRAPHY IN THE  
MONTEREY-EQUIVALENT PISMO FORMATION AND ITS  
RELATIONSHIP TO PRIMARY SEDIMENTOLOGY AND  
STRATIGRAPHY AT MONTAÑA DE ORO  
STATE PARK, CALIFORNIA

By

Heather M. Strickland

August 2013

The Monterey-equivalent Miguelito Member of the Pismo Formation at Montaña de Oro State Park displays four orders of fracture length from several cm to tens of meters and three sets of fracture orientation in a ~200-m-thick stratigraphic section north of Spooner's Cove. Characterization of fractures such as these is crucial to understanding reservoir behavior in low-permeability, fine-grained rocks that require natural or induced fractures for economic hydrocarbon production. Fracture spacing and fracture trace length are related to primary sedimentary lithologic cycles and vary with bed-thickness and lithologic composition. Three distinct fracture sets reflect the regional maximum horizontal stress direction and their frequency and length are affected by pre-existing fractures, tuffaceous horizons, and mudstone-dominated lithostratigraphic packages

greater than 10 meters in thickness. The fracture networks differ from north to south and show significantly different manifestations of strain expressed in all orders of fractures.



FRACTURE NETWORKS AND MECHANICAL STRATIGRAPHY IN THE  
MONTEREY-EQUIVALENT PISMO FORMATION AND ITS  
RELATIONSHIP TO PRIMARY SEDIMENTOLOGY AND  
STRATIGRAPHY AT MONTAÑA DE ORO  
STATE PARK, CALIFORNIA

A THESIS

Presented to the Department of Geological Sciences  
California State University, Long Beach

In Partial Fulfillment  
of the Requirements for the Degree  
Master of Science in Geology

Committee Members:

Richard J. Behl, Ph.D, (Chair)  
Tom Kelty, Ph.D.  
Michael R. Gross, Ph.D.

College Designee:  
Robert D. Francis, Ph.D.

By Heather M. Strickland

B.S. 2011, California State University, Long Beach

August 2013



## ACKNOWLEDGEMENTS

I would like to take this opportunity to extend a very heartfelt “Thank you” to everyone who offered their support and direction throughout the numerous phases of this thesis project.

To Dr. Richard Behl, a very sincere thank you for the opportunity to work with you on this incredible project and to be a part of the Monterey and Related Sediments (MARS) consortium. You have been an inspiration to me in so many ways since I decided to change my major to geology. You have shown me how to be a great student, from how to do research, to leading field trips, to giving presentations, and so much more. I am so grateful for your guidance throughout my undergraduate and graduate degrees and you have been instrumental in my development as a geologist and a person.

To Dr. Michael Gross, a warm and heartfelt thank you for taking me under your wing. I had not even heard of the fascinating subject of mechanical stratigraphy before hearing your talk in the summer of 2011, and had no idea when I asked you countless questions on our field trip that we would do great work together. Words cannot explain how much I have learned and how appreciative I am of your mentorship through my thesis research and my summer internship at Shell Exploration and Production.

To my Dad, a special thank you for all your encouragement during my journey through life, your help as a field assistant, for letting me use your camping trailer during field work, and especially for your support during the past few years of my studies. I had

no idea that taking your advice, “just make school number one,” would lead me on such a great adventure. I guess you do know what you are talking about, Dad.

Thank you Tom Kelty and Richard Heermance III at CSUN for your time and guidance through my research and data collection. I would also like to thank all of the affiliate members of the Monterey and Related Sedimentary Rocks (MARS) consortium members for their support and membership. With your support I was able to focus on my research and not have to work another job, something I could not have done otherwise. A special acknowledgement goes to ExxonMobil for lending CSULB the hand-held gamma-ray spectrometer, without which the correlation between primary stratigraphy and fracture networks would not have been as quick to determine.

I would like to bestow a very, very special thank you to all of my field assistants that were involved in this project. The data from this study was 100% field data and required an incredible amount of time and effort by myself and my field partners to collect. I would like to thank all of my field partners for the help and a job well done, Pam Hill, Annie Mosher, Nawaf Al Shammari, Eric Arney, Jeanette Harlow, David Dillon, Bryan Petry, Paul Allesio, Karissa Huey, Jeremy Strickland, and Dave Strickland. Without your help, this project would have taken months longer because of the intensive data collection. Thank you David and Bryan for carrying the heavy LiDAR equipment up and down the sand dunes and across the slippery outcrop, you two made that part of the project so much less painful.

## TABLE OF CONTENTS

	Page
ACKNOWLEDGEMENTS .....	iii
LIST OF TABLES .....	vi
LIST OF FIGURES .....	vii
CHAPTER	
1. INTRODUCTION .....	1
Objective .....	3
Geologic Setting.....	5
Monterey Formation .....	10
Pismo Formation.....	13
Description of Major Faults .....	14
Fracture Networks and Mechanical Stratigraphy .....	18
Previous Geologic Studies of the Field Area.....	20
2. METHODS .....	23
Selection of Study Area .....	23
Major and Minor Lithostratigraphic Unit Designation.....	26
Hand-Held Spectral Gamma-Ray .....	27
Fracture Data.....	29
3. DATA AND RESULTS .....	36
Stratigraphic Analysis.....	36
Major and Minor Lithostratigraphic Units.....	36
Gamma-Ray Stratigraphy .....	46
Structural Analysis.....	51
Fourth-Order Fractures .....	52
Fractures in Orders 1-3 .....	59

CHAPTER	Page
Fracture Termination-Orders 1-3 .....	80
4. DISCUSSION .....	86
Effect of Lithology .....	87
Stratigraphy and Fracture Development .....	88
Fracture Development and Regional Tectonic Strain .....	95
Mechanical Layer Boundaries .....	104
5. CONCLUSIONS .....	113
6. FUTURE WORK .....	115
APPENDICES .....	117
A. MAJOR AND MINOR LITHOSTRATIGRAPHIC UNIT MEASUREMENTS .....	118
B. STEREO PLOT OF BEDDING .....	121
C. RESULTS OF 4 <sup>TH</sup> -ORDER SCANLINE DATA FOR PORCELANITE AND MUDSTONE .....	123
D. SUMMARY OF 4 <sup>TH</sup> -ORDER SCANLINE DATA IN THE NORTHERN (UPPER) AND SOUTHERN (LOWER) SECTIONS .....	126
E. MEASUREMENTS OF FEATURES IN FRACTURE ORDERS 1-3 .....	128
F. RESULTS OF SCANLINE MEASUREMENTS FOR FRACTURE ORDERS 1-3 .....	135
G. SUMMARY OF SCANLINE MEASUREMENTS FOR FRACTURES IN ORDERS 1-3 FOR THE NORTHERN AND SOUTHERN SECTIONS .....	137
H. LIST OF UPPER AND LOWER FRACTURE TERMINATIONS IN ORDERS 1-3 .....	139
I. SUMMARY OF FRACTURE TERMINATIONS FOR ORDERS 1-3 .....	144
J. STRESS DATA FROM WORLD STRESS MAP PROJECT .....	146
REFERENCES CITED .....	148

## LIST OF TABLES

TABLE	Page
1. Summary of Data in the Northern and Southern Sections .....	86

## LIST OF FIGURES

FIGURE	Page
1. Fracture architecture in mechanically layered rocks .....	2
2. Location map of study area.....	4
3. Onshore sedimentary basins in central California .....	7
4. Schematic cross-section through the Pismo Syncline.....	7
5. Stereonets of regional maximum horizontal stress from Middle Miocene to Quaternary .....	9
6. Fault map of the area surrounding Montaña do Oro State Park .....	16
7. Map of southern central California’s kinematic domains.....	17
8. Fracture spacing ratio and fracture spacing index plots from the Monterey Formation .....	19
9. Composite diagram of preliminary field mapping.....	25
10. Field photograph of gamma-ray spectrometer.....	28
11. Description of 1 <sup>st</sup> , 2 <sup>nd</sup> , 3 <sup>rd</sup> , and 4 <sup>th</sup> order fractures with corresponding photos.....	30
12. Field photograph of large feature scanline.....	31
13. Field photographic of 4 <sup>th</sup> -order fracture scanline.....	32
14. Aerial photograph of field area indicating scanline locations .....	35
15. Photograph of major lithostratigraphic units .....	38

FIGURE	Page
16. Stratigraphic columns .....	40
17. Field photographs of bedding .....	42
18. Field photograph of massive mudstone with a phosphatic pebble conglomerate at its base .....	47
19. Field photograph of tuff horizon near the base of 6C .....	48
20. Field photograph of fracture terminations .....	48
21. Graphical representation of the gamma-ray survey .....	50
22. Correlation of total gamma-ray to major and minor units .....	51
23. Mudstone and porcelanite stereoplots.....	54
24. Histograms of fracture data in mudstone and porcelanite .....	56
25. Scatter plot of 4 <sup>th</sup> -order porcelanite scanline data.....	57
26. Scatter plot of 4 <sup>th</sup> -order mudstone scanline data.....	57
27. Scatter plots of 4 <sup>th</sup> -order fracture spacing and bed thickness by upper and lower sections.....	58
28. Fracture spacing ratio plotted with stratigraphic position.....	59
29. Base map for the following fracture maps in Figures 30, 31, 32, and 33 .....	61
30. Fracture map of major unit 2 .....	62
31. Fracture map of major unit 4 .....	63
32. Fracture map of major unit 4-8 .....	65
33. Fracture map of major unit 8-9 .....	67
34. Composite fracture map of features in orders 1-3 .....	68
35. Histogram of measured trace length of fractures in orders 1-3 .....	69

FIGURE	Page
36. Histogram of corrected stratigraphic stratigraphic length of fractures in orders 1-3 .....	69
37. Orientation data of features belonging to fracture orders 1-3 for the entire field area .....	70
38. Fracture set analysis of features in fracture orders 1-3 .....	71
39. Linear rose diagram and poles to fracture planes of the upper (top) and lower (bottom) section .....	73
40. Bar plot illustrating the normalized cumulative fracture length per meter scanline.....	76
41. Bar plot showing the average normalized cumulative corrected fracture length by major unit.....	76
42. Bar plot showing the average cumulative corrected fracture length per meter scanline in the upper and lower sections .....	77
43. Graph of cumulative measured trace length per 5 degree orientation between 0 and 180° .....	78
44. Graph of cumulative corrected stratigraphic length per 5 degree orientation between 0 and 180°.....	78
45. Graph of cumulative corrected stratigraphic length per 10 degree orientation between 0 and 180° in the upper section and lower section.....	79
46. Bar plot showing the frequency of fracture orders 1-3 by major unit .....	80
47. Field photograph illustrating “unknown” and “rock mass” fracture terminations in Major Unit 2.....	83
48. Field photograph of “set A” and “tuff” termination .....	83
49. Pie chart of fracture termination horizons as a percent of the total number of terminations measured.....	84



FIGURE	Page
50. Histogram of number of fracture terminations plotted in stratigraphic depth.....	85
51. Mechanical stratigraphic column.....	87
52. Scatter plot of porcelanite FSR and calculated average porcelanite:mudstone .....	91
53. Composite fracture continuum diagram.....	94
54. World Stress Map (World Stress Map Project, 2013) and regional fault map of the area surrounding the study site .....	98
55. Stereoplot showing the angular relationships of average bedding fracture sets A, B, and C, and regional maximum horizontal stress .....	99
56. Stereoplot of the all features with offset relative to $SH_{max}$ .....	99
57. Composite diagram of fracture data in all four orders throughout the field area and their relationship to structural position.....	102
58. Sketch of multilayer fracture “swarm” .....	103
59. Field photograph and sketch of fracture damage zone associate with tuff horizons .....	108
60. Composite diagram of fracture data relative to major lithostratigraphic and mechanical units.....	110
61. Conceptual model of the fracture network at Montana de Oro .....	112

## CHAPTER 1

### INTRODUCTION

Exploration and exploitation of hydrocarbons increasingly includes “tight” (low permeability) reservoirs and other unconventional plays to address meeting the world’s growing energy demands (USGS, 2012). These unconventional petroleum reservoirs do not just store and produce hydrocarbons from intergranular pores, but rely on fractures and faults in the rock for their permeability. Consequently, characterization of natural fractures is a key component to understanding connectivity and fluid flow behavior in petroleum reservoirs, hydrothermal systems, fractured aquifers, and also for understanding the behavior of artificially induced fractures in the subsurface. How fracture development is related to variation in a number of factors, and how they interrelate in space and time are critical to understanding the fracture network and resulting mechanical stratigraphy.

Critical factors known to control natural fractures in sedimentary rocks include structural position (e.g., proximity to faults or degree of curvature in a fold), physical properties of the rocks (e.g., Young’s modulus, Poisson’s ratio, brittleness), lithology, and bed thickness (Finn et al., 1993; Wu and Pollard, 1995; Gross, 1995; Gross et al., 1995; Bai and Pollard, 2007; Hennings et al., 2000; Schwalbach et al., 2007; Ghosh and Shankar, 2009). In the case of California’s Monterey Formation, silica diagenetic grade is also of major significance (Snyder et al., 1984). Several of these variables are

integrated in the framework of “mechanical stratigraphy,” defined as the subdivision of a rock section into discrete units by their deformational style, structures, or mechanical properties (Laubach et al., 2009). Each mechanical stratigraphic unit is defined by mechanical layers in which the structures, deformational style and/or mechanical properties do not propagate through the layer boundaries (Figure 1). Understanding the development of fracture networks and the resulting mechanical stratigraphy can aid in the prediction of subsurface flow in hydrocarbon reservoirs and aquifers.

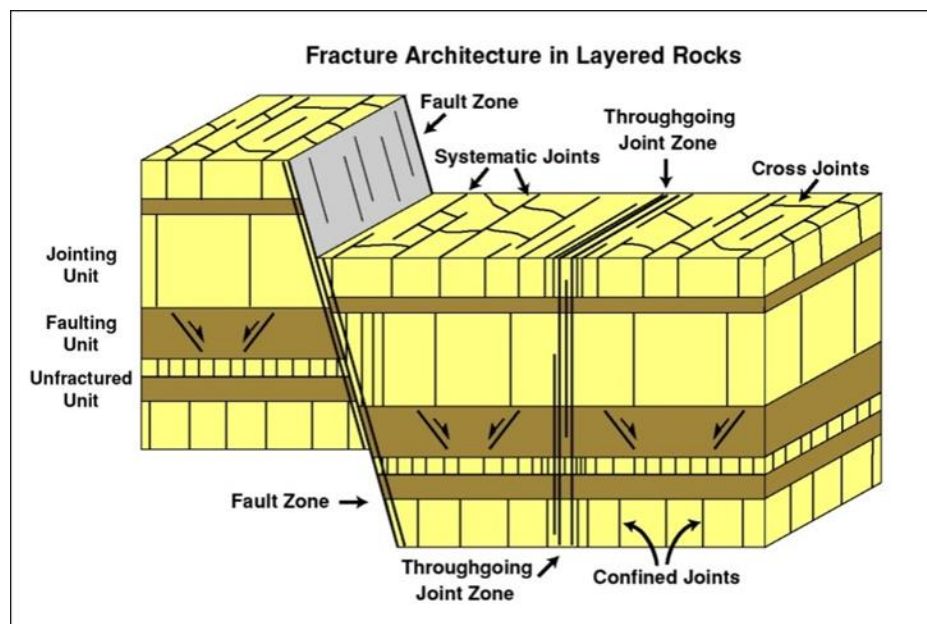


FIGURE 1. Fracture architecture in mechanically layered rocks (Gross, 1995). Generalized schematic representing fracture geometry, distribution and hierarchy that can be found in layered rocks. Interbedded lithologies that have contrasting mechanical properties can express deformation differently in response to the same applied strain.

This study attempts to understand how primary stratigraphy—including sedimentary cycles at several scales—relates to lithology and fracture architecture in the upper Monterey Formation-equivalent rocks at Montaña de Oro State Park, San Luis

Obispo County, in an effort to better understand naturally fractured reservoirs in fine-grained rocks. The Miocene Monterey Formation is well exposed in coastal outcrops across California and has been intensely studied for its complex silica diagenesis, hydrocarbon potential, stratigraphy, and unique structural deformation. This formation contains many distinctive reservoir facies that can have additional complication from the presence of natural fractures (Schwalbach et al., 2007). Many studies have focused on fracture spacing in units of different silica phases and lithology (Narr and Suppe, 1991; Gross et al., 1995) and have shown that the fractures often express different modes of displacement based on their lithology (Gross, 1995).

These rocks are especially well suited for this kind of study because of their high degree of natural fracturing within alternating beds of contrasting physical properties. Also, rocks equivalent to those at Montaña de Oro State Park are similar to subsurface hydrocarbon reservoirs in the San Joaquin, Santa Barbara, and Santa Maria basins (Schwalbach et al., 2007) and the presence of natural fractures are often pivotal to the “plumbing” of the hydrocarbon system.

### Objective

The objective of this study is to measure and describe the fracture network at Montaña de Oro and determine how variations in fracture orientations and dimensions may relate to primary sedimentology and stratigraphy. To investigate the relationship between structural deformation and stratigraphy, this study integrates both structural and stratigraphic/sedimentologic data. The fracture network is defined by photo-based mapping and measurement of the spacing, dimensions, and orientations of fractures and faults within a four-order framework developed specifically for this study. Sedimentary

cyclicality is characterized by direct description, measurement, and collection of gamma-ray spectrographic data. This study examines the fracture network and fracture population statistics as they relate to the stratigraphy at the reservoir scale, specifically as shown by natural spectral gamma-ray response. The area under investigation is approximately 400 meters of exposed section (200 m of stratigraphic section) north of Spooner's Cove (Figure 2) consisting of thinly bedded opal-CT-phase porcelanite, siliceous mudstone, and dolostone.

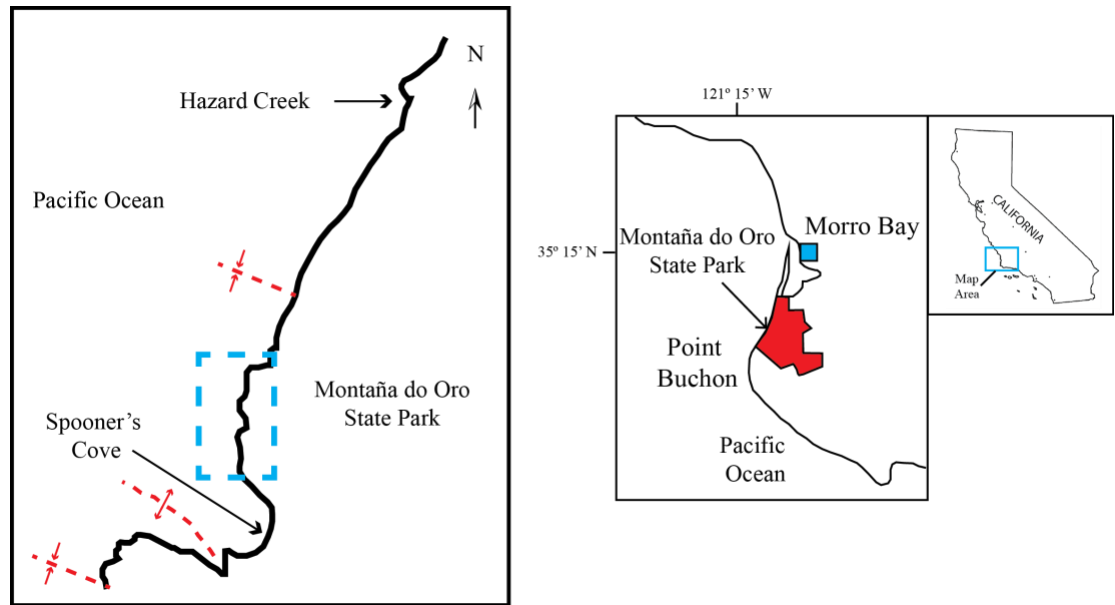


FIGURE 2. Location map of study area. Inset map showing Montaña de Oro State Park in red (right). The blue box indicates the location of field area within the state park (Modified from Keller, 1992).

## Geologic Setting

Numerous sedimentary basins—including the Pismo basin, site of this study—formed in conjunction with reorganization of the North American and Pacific plate margin as the oceanic spreading center between the Farallon and Pacific plates collided with the western margin of the North American plate approximately 29 Ma (Blake et al., 1978; Hall, 1981a, 1981b; Sedlock and Hamilton, 1991; Titus et al., 2007). The late Cenozoic (or Neogene) tectonic evolution of central California was dominated by the interactions between ancient oceanic plates and the continental margin, in particular, changes in the relative vector between the Pacific and North American plates and translation and rotation of several microplates (McCroory et al., 1999). Basin formation along the margin was time-transgressive both north- and southward as the two newly formed triple junctions migrated away from the point of original contact (Blake et al., 1978). Southern California basins began to form from the late Oligocene to early Miocene, while the central and northern California basins mainly formed over a shorter period of time in the mid-to-late Miocene (Atwater, 1980).

The transition from subduction to strike-slip tectonics, as the Monterey spreading ridge ceased, likely caused widespread late Early Miocene subsidence and volcanism. Miocene subsidence occurred in two stages: (1) an initial rapid phase (approximately 18-16 Ma) caused by extreme local extension of the continental crust triggered by the Monterey Microplate capture and related to the rotation of the Western Transverse Ranges; (2) a slower phase (approximately 1-7 Ma) attributed to thermal subsidence as the underplated young oceanic crust cooled (McCroory et al., 1999).

Subsidence diminished in the late Miocene and uplift began around 5.5 Ma in the Santa Maria Basin, just south of the study area. This transition is attributed to the reorientation of the Pacific plate velocity vector resulting in the development of regional fold and thrust belts, as well as the continued rotation of the Western Transverse Ranges. Since the middle Pliocene (3 Ma), strike-slip along the San Andreas fault system and compression along reverse faults and associated folds on either side of the San Andreas fault has accommodated motion along the plate boundary (McCroory et al., 1999).

The tectonism of the late Cenozoic is recorded in the tertiary strata of these sedimentary basins (McCroory et al., 1999). The modern sedimentary basins are characterized by elongated shapes with parallel to subparallel orientations to the San Andreas fault (Crowell 1987; Miller, 1992). Montaña de Oro State Park lies within the Pismo-Huasna basin (Figure 3) and is part of the Santa Maria Basin province. The Pismo-Huasna basin lies mainly onshore, with only its northwesternmost section offshore. It is a pull-apart basin bounded by the West Huasna fault to the east and the Hosgri fault system to the west and is underlain by the Miocene Obispo Formation consisting of mainly volcanic rocks. One of the major structural features in the Pismo basin is the Pismo Syncline (Figure 4), which served as the depositional basin for the majority of the Miocene and Pliocene (Surdam and Stanely, 1984).

In the Pismo basin, the stratigraphy consists of Mesozoic basement rocks overlain by Cenozoic formations that show a transition from non-marine to marine sedimentation. The Mesozoic Franciscan assemblage is a *mélange* of various lithologies, such as claystone, greenstone, schist, metavolcanic rocks, serpentinite, and chert resulting from accretion during oblique subduction of the Farallon plate.

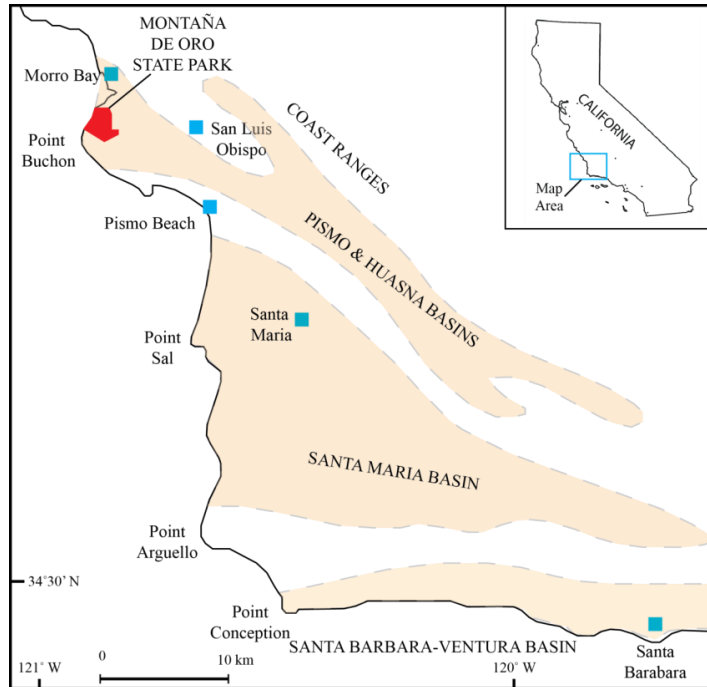


FIGURE 3. Onshore sedimentary basins in central California. Index map of southern central California showing the location of Montaña de Oro State Park (in red) and the onshore extent of Neogene sedimentary basins (shaded in orange). Modified from Keller (1992).

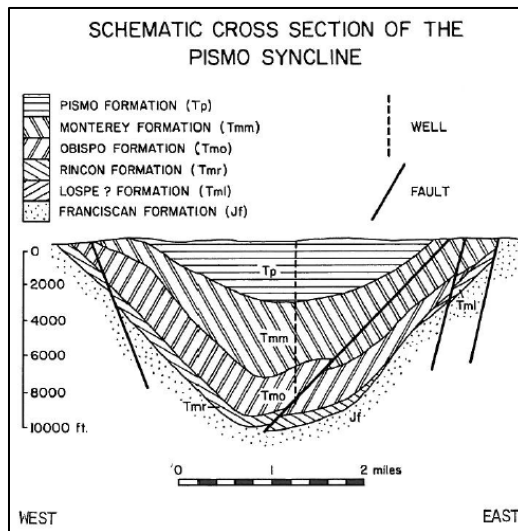


FIGURE 4. Schematic cross-section through the Pismo Syncline (Surdam and Stanley, 1984).



Outcrops in the Pismo basin show that the contact between basement and Cenozoic strata is characterized either by onlap of the Sespe Formation, Vaqueros Sandstone and Rincon Shale, or an intrusive contact between Obispo Formation diabase and basement rocks (15.5 Ma; Surdam and Stanley, 1984).

Coeval to the formation of the Pismo-Huasna basin were bimodal basalt-rhyolite volcanism and development of paleobathymetric volcanic highs, which subsequently influenced the distribution of diatomaceous sedimentation that makes up the Monterey Formation and related sedimentary units (Surdam and Stanley, 1984). During the middle Miocene, a zone of wrench faulting formed seaward of the San Andreas fault and a series of right-lateral, strike-slip faults formed, including the San Gregorio-Hosgri and Rinconada fault systems. These right-lateral, major fault systems with related small faults created structurally controlled blocks that underwent rapid uplift and subsidence, controlling the geometry of sedimentary basins in the Coast Ranges, including the Pismo-Huasna basin, and contributing to rapid vertical and lateral changes in lithofacies.

Miocene tectonics in the Los Osos domain was initially dominated by extensional forces through the middle to late Miocene which are reflected in interpreted offshore seismic data as high angle normal faults and growth faults, faults mapped through well control (Namson and Davis, 1990), and syn-compactional normal faults mapped in coastal outcrops in the Santa Maria Basin (Gross, 1995; Gutierrez-Alonzo and Gross, 1997). A change to compression in the late Pliocene-Quaternary is characterized by west-northwest to northwest fold axes and thrust faults, which advocates northeast-southwest shortening (Vittori et al., 1994). Figure 5 compares stereonet diagrams of the

regional fold axes in the Middle Miocene-Oligocene to the Late Pliocene-Quaternary calculated by Vittori et al. (1994).

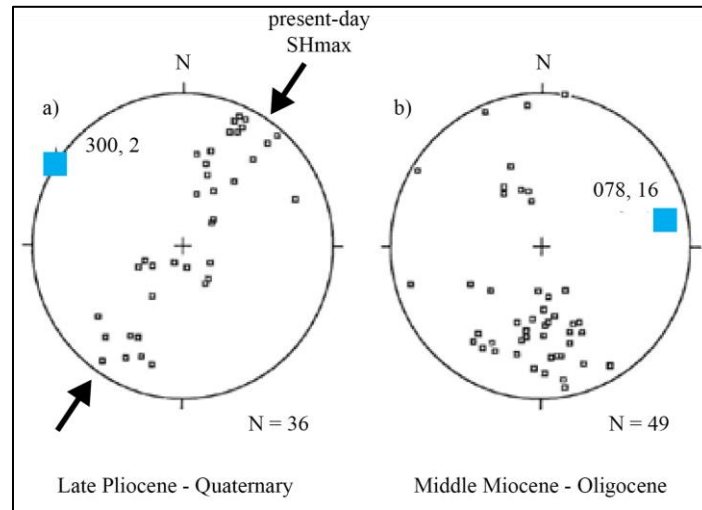


FIGURE 5. Stereonets of regional maximum horizontal stress from middle Miocene to Quaternary. (A) Poles to bedding in the late Pliocene-Quaternary (empty squares) and calculated best-fit fold axis is  $300^{\circ}$  (blue squares). (B) Poles to bedding in the middle Miocene-Oligocene and the calculated best-fit fold axis is  $78^{\circ}$  (Modified from Vittori et al., 1994).

The mean maximum horizontal stress direction ( $SH_{max}$ ) of NNE-SSW in the Santa Maria Basin Province (southern structural blocks in the Los Osos Domain) has been addressed by several workers. Vittori et al. (1994) calculated mean  $SH_{max}$  in the San Luis Obispo-Santa Maria area to be  $202^{\circ}$  from fault slip data in the region. Finkbeiner et al. (1997) calculated the mean regional  $SH_{max}$  to be  $213^{\circ}$  using borehole breakout data from four wells in the offshore Santa Maria basin provided by Chevron. The World Stress Map Project yields a mean  $SH_{max}$  of  $42^{\circ}$  (equivalent to  $222^{\circ}$ ), from stress data from

borehole breakouts and focal mechanisms (formal inversion and single) in the region surrounding the study area.

### Monterey Formation

The Miocene Monterey Formation was syn-and-post-tectonically deposited from approximately 16-4 Ma following the transition from a convergent to a transform margin along the coast of California (Behl, 1999). During the time of Monterey Formation deposition, tectonic, climatic, and oceanographic changes created high biologic productivity in the surface water along the California coast, and water conditions were favorable to the preservation of siliceous, calcareous, and organic matter within the sediments (Pisciotta & Garrison, 1981). The Formation, or its stratigraphic equivalents, are distributed both on- and offshore, with thickest accumulations in sedimentary basins that extend from north of San Francisco to south of Los Angeles (Behl, 1999). Across coastal California, the Monterey Formation has an average thickness of 300-500 meters, but the thickness can be tremendously variable, locally exceeding 2,000 meters or pinching out entirely (Bramlette, 1946).

In general, the Monterey Formation represents the deep-water basinal facies of the Tertiary basin cycle. Internally, the Monterey consists of a lower calcareous facies, a middle phosphatic facies, and an upper siliceous facies—the latter being the context for this study. The highly silica- and organic-rich deposits of the Monterey Formation record a combination of tectonic, oceanographic, and climatic events during the Miocene (Ingle, 1981; Pisciotta and Garrison, 1981; Barron, 1986; Behl, 1999). Pelagic deposits dominated the deposition throughout the time of the Monterey Formation due, in large part, to margin-wide subsidence and the consequent reduction in clastic input (Ingle,

1981; Surdam and Stanley, 1984). The Monterey Formation has a distinctive upper siliceous facies that is expressed as interbedded diatomite or diatomaceous mudstone (opal-A phase), porcelanite or chert in opaline silica (cristobalite-trydimite (CT) or quartz phase), depending on the degree of diagenetic alteration and primary composition (Issacs, 1981a; Behl, 1998). Porcelanite is a rock that has been diagenetically altered from diatomite and is composed of 50-80% biogenic silica (opal-CT or quartz phase) and has a blocky-to-hackly fracture (Behl and Garrison, 1994).

The siliceous facies of the Monterey Formation and its equivalent rocks often express rhythmic bedding at a variety of scales. The alternations can be sub-millimeter-scale laminations, 5-10 cm beds, and alternations up to 4-meters thick (Pisciotta and Garrison, 1981). Bramlette (1946) first described the rhythmic bedding as “rythmites,” in which each unit consists of a coupling of a clastic or terrigenous unit and a siliceous or biogenic member. Pisciotta and Garrison (1981) was the first to describe the rhythmic bedding in detail and designated 3 different types of alternations: (1) clastic-biogenic cycles; (2) massive-laminated cycles; and (3) diagenetically enhanced cycles. These cycles are generally, but not always related, in the sense that clastic-diagenetic cycles are often associated with massive-laminated cycles and influence the development of diagenetically enhanced cycles. These cycles affect lithology, bed thickness, and brittleness of the strata, which are key factors that affect how the rocks will respond to brittle deformation (i.e., fracturing and faulting). It is reasonable to speculate that the different cycles in the Monterey Formation may affect the subsequent fracture development as strain is applied to the rocks. A brief summary of Pisciotta and Garrison’s (1981) description of the cycles are described in the following 2 paragraphs.

Estimates of the duration of time represented by these intervals may vary by 1- to 2-orders of magnitude depending on location and changes of the dating and age model of a studied section and the level of compaction as highly porous diatomaceous rocks transform to less porous opal-CT and quartz equivalents.

First-order clastic-biogenic cycles are caused by seasonal upwelling and runoff and express laminated yearly couplets of clay and biogenic silica with accumulation rates of approximately 0.8 mm/yr (compacted thickness). Second-order clastic-biogenic cycles are couplets that range from 1-20 cm thick and are composed of a clastic unit and a siliceous member, massive or laminated, and represent 12-200 years of time. Third-order clastic biogenic cycles are couplets of clastic and siliceous rocks superimposed on 1<sup>st</sup>- and 2<sup>nd</sup>-order cycles, generally range from 2-5 m, and represent approximately 1,800-2,100 years.

Second-order massive-laminated cycles are couplets of siliceous rocks, ranging from 5-15 cm thick, that alternate between massive and laminated. Pisciotto and Garrison (1981) interpreted that massive intervals represent roughly 125 years and laminated intervals represent approximately 60 years. Third-order massive-laminated cycles are alternations of massive and laminated layers (several meters thick) in diatomites and each member represents 1,800-3,750 years. Second-order diagenetically-enhanced cycles are porcelanite and chert of 2<sup>nd</sup>-order clastic-biogenic and 2<sup>nd</sup>-order massive-laminated cycles. Third-order diagenetically-enhanced cycles are alternations of chert and porcelanite strata with diatomite or mudstone, are roughly 3-m thick, and represent approximately 3,750 years.

The cyclity described by Pisciotto and Garrison (1981) ranges from the seasonal to the multi-millennium-scale. The cycles described above reflect changes in deposition of the Monterey Formation, influenced by climate, sea level, terrestrial runoff, and oceanic upwelling. “Milankovitch” orbital cycles—eccentricity, obliquity, and precession—are known to affect the Earth’s climate and sedimentary record in form many times and places ways (Imbrie et al., 1992). As in other sedimentary records, it is likely that Milankovitch cycles are a driving force in the development of multi-meter-scale rhythmic bedding of the Monterey Formation as shown by Hill (2005) to be detectable by gamma-ray logs in the offshore Monterey and Sisquoc formations equivalents. It is an intriguing possibility that the architecture of fracture networks and mechanical stratigraphy may follow a template of predictable, universal climatic cycles that are expressed throughout time and across the Earth’s surface.

#### Pismo Formation

The Pismo Formation overlies the Monterey Formation in the Pismo basin and is upper Miocene to Pliocene in age (Surdam and Stanely, 1984). The Pismo Formation consists of five members, in ascending order: the Miguelito, Edna, Gragg, Belleview and Squire. The Miguelito Member, which is the focus of this study, is dominated by porcelanite-mudstone (diatomite-mudstone prior to diagenesis) or sandstone and is thought to represent basinal mudstone and diatomaceous sedimentation. Inner shelf deposition is recorded by the Edna Member (partially time-equivalent to the Miguelito Member) and both the Edna and Miguelito members are overlain by the dominantly sandstone Gragg Member. The Belleview Member overlies the Gragg member and consists of diatomaceous mudstone and sandstone. The youngest member, Squire,

represents the final stage of Pismo deposition and is dominantly sandstone (Stanley and Surdam, 1981).

The Miguelito Member at Montaña de Oro has an estimated total thickness between 2,250 ft. and 2,900 ft. and has been dated by Keller (1992) to be 9-10 Ma in the basal strata and 6 Ma in the youngest strata. Keller (1992) used silicoflagellates and diatom assemblages in 20 dolostone beds between Coon and Hazard creeks (Figure 2) to date the Miguelito Member. Keller states that because the youngest strata in the Miguelito section are no younger than 6 Ma, and the basal Sisquoc Formation is no older than 6 Ma, the Miguelito section at Montaña de Oro is chronostratigraphically equivalent to the upper Monterey Formation in the neighboring Santa Maria and Santa Barbara-Ventura basins. Its thin-bedded and laminated succession is also lithologically equivalent to the upper Monterey Formation in those areas.

#### Description of Major Faults

Montaña de Oro is in a region of California that is characterized by transpressional deformation between the overall right-lateral San Gregorio-San Simeon-Hosgri fault system to the west and the San Andreas fault system to the east (Figure 6). According to Lettis et al. (1992) and other workers, the transpressional deformation is driven by separate but interlinked processes being: (1) northward transfer of slip from the San Andreas fault system to the Rinconada and West Huasna fault zone to the Hosgri fault system; (2) northward direction strain as a result of the rotation of the western Transverse Ranges; and (3) potential plate-normal convergence in this geographical region.

Transpression in this region has caused several discrete and related crustal domains and tectonic structures (Pacific Gas and Electric Company, 1988; Lettis et al., 1992), which include the Los Osos domain, western Transverse Ranges, and the Santa Lucia-San Rafael Ranges. Montaña de Oro is located in the Los Osos domain, which is a triangular area characterized by a northwest structural grain of reverse, strike-slip, and oblique faults bordering uplifted blocks and subsiding basins within the domain. The Los Osos domain encompasses the Santa Maria Basin Province and Los Osos Valley and Cambrian structural blocks (Figure 7). The domain is bordered by the Hosgri-San Simeon fault zone on the west, the West Huasna fault zone on the east and the western Transverse Ranges to the south and encompasses the entire Santa Maria and Pismo-Huasna basins (Lettis et al., 1990).

Within the Los Osos domain, there are influential faults surrounding the study area that should be considered when interpreting structural data: the Los Osos fault zone, the Hosgri fault zone, and the Shoreline fault (Lettis and Hanson, 1992; Hardebeck, 2013). The fault most proximal to Montaña de Oro is the Los Osos fault, which is a series of steeply dipping, *en echelon* fault segments with both strike-slip and reverse components, striking west-northwest (Lettis and Hall, 1994) and is roughly 3 km north of the study area. The dip of the fault is not well constrained due to its complexity and has been referred to as normal, reverse, and oblique-slip (PG&E, 2011; Southern California Earthquake Data Center, 2013). The Los Osos fault zone terminates to the east when it meets the west Huasna fault and on the west when it intersects the Hosgri fault zone. The Los Osos fault zone is approximately 50 km in length and 2-km wide with a slip rate of approximately 0.2 mm/yr (Lettis and Hall, 1994).



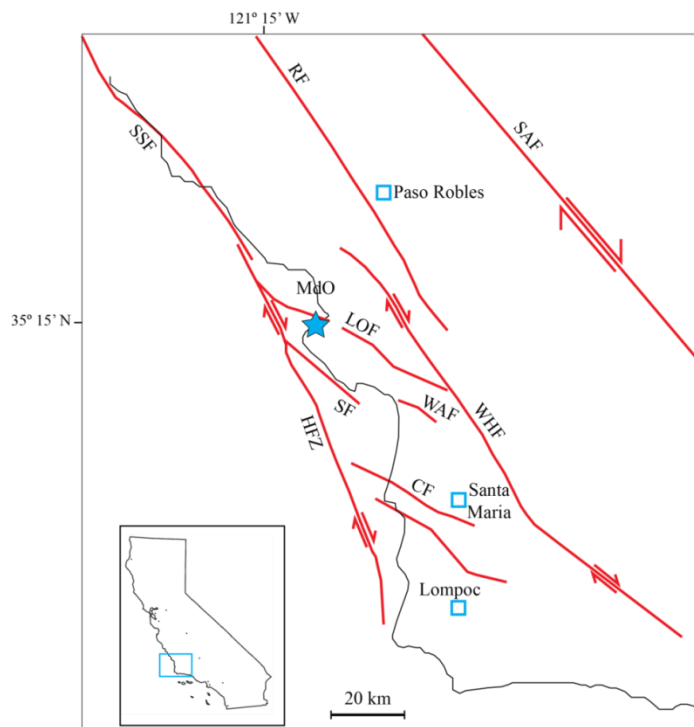


FIGURE 6. Fault location map of the area surrounding Montaña de Oro (MdO). San Andreas fault (SAF); West Huasna fault (WHF); Rinconada fault (RF); Los Osos fault zone (LOF); shoreline fault (SF); Hosgri fault zone (HFZ); San Simeon fault (SSF). Modified from Hardebeck (2010).

This fault zone separates the uplifting San Luis Range from the southwestern tilting Cambrian block to the north (Figure 7).

The Hosgri fault borders the Los Osos domain to the west and is the southernmost segment of the San Gregorio-San Simeon-Hosgri fault system that splays off the San Andreas fault just north of San Francisco (Hall, 1975; Lettis et al., 1992; Sorlein et al., 1999). The fault system is roughly 5 km west of the study area and is mainly strike-slip with some areas of reverse movement, is 410 km in length, strikes between N25°W and

N30°W and has a maximum vertical offset of 400 meter (Hanson et al., 1995). Strain is partitioned across the Hosgri fault and results in different structural deformation on either side of the fault.

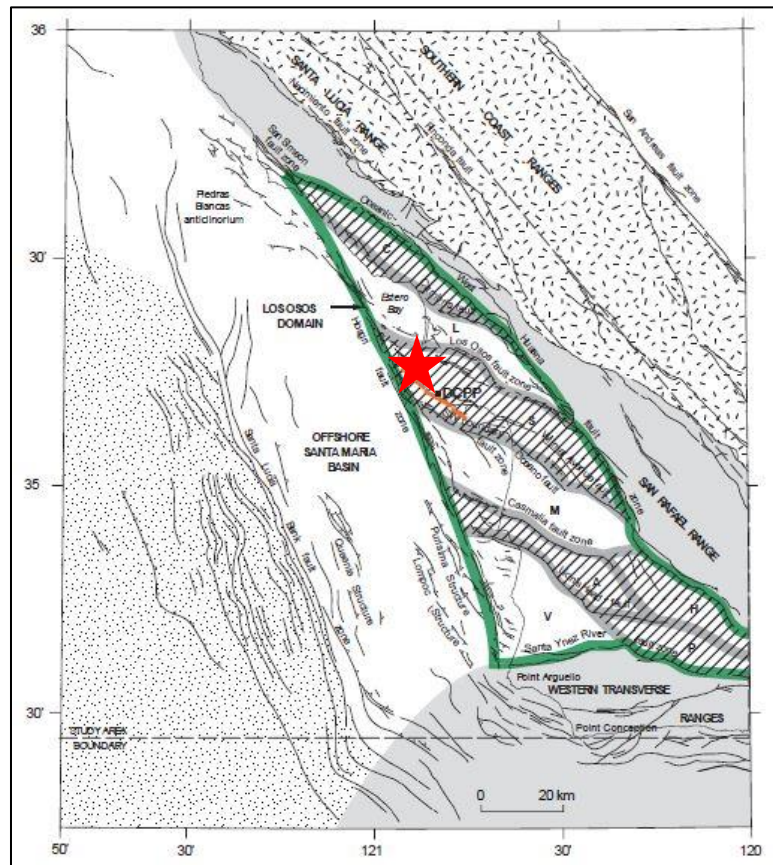


FIGURE 7. Map of southern central California's kinematic domains. These include the Los Osos domain, offshore Santa Maria basin domain, Southern Coast Ranges domain, and the Western Transverse Ranges domain. The Los Osos domain is separated into several distinct structural blocks: C-Cambria, L-Los Osos Valley, S-San Luis/Pismo, M-Santa Maria Valley, A-Casmalia, H-Solomon Hills, V-Vandenberg/Lompoc, P-Purisima. Red star is location of Montaña de Oro State Park (modified from PG&E, 1988).

West of the Hosgri fault, the compression direction is perpendicular to the fault with relatively little deformation when compared to the east side of the fault. East of the fault, the compression direction is NNE-SSW and the related folds are at a high angle to the fault (Sorlien et al., 1999). The interaction between the San Andreas and San Gregorio-Hosgri fault systems was crucial to the formation and subsequent deformation of the Neogene Pismo-Huasna basin.

The Shoreline fault is roughly 5 km south of the field area, is vertically oriented with right-lateral strike-slip offset and its northwestern end extends to the Hosgri fault (Hardebeck, 2010). There are 3 segments to the Shoreline fault—and the average strike of the 3 segments is  $300^\circ$  (PG&E, 2011). The studies of Hardebeck (2010) and the Pacific Gas and Electric Company (2011) focus on the seismic risk of the Shoreline fault, as it is less than 1 km from the Diablo Canyon Power Plant. There is much unknown about the Shoreline fault, as it was first recognized in 2010.

#### Fracture Networks and Mechanical Stratigraphy

Fracture architecture at Montaña de Oro has been discussed in a qualitative manner in many published and unpublished guidebooks associated with professional field trips, but to date there is no quantitative study that describes the fractures and faults. Elsewhere in the Monterey Formation, several previous studies have addressed failure mode as a function of lithology (fracture partitioning) (Gross, 1995), fracture spacing (Narr and Suppe, 1991; Gross et al., 1995) and development of throughgoing features (Finn et al., 2003).

Fracture spacing ratios (mechanical layer thickness divided by median joint spacing) vary with lithology, and that the more brittle lithologies will have a higher

fracture spacing ratio than less competent lithologies (Figure 8; Gross et al., 1995). In addition to fracture studies in the Monterey Formation, studies show a positive correlation between fracture spacing and bed thickness in rocks of the same lithology (Ladiera & Price, 1981; Wu & Pollard, 1995; Narr & Suppe, 1991) in layered sedimentary rocks. Throughgoing fractures (those that span multiple stratigraphic beds) in the Monterey Formation often develop by the coalescence of pre-existing fractures (Finn et al., 2003).

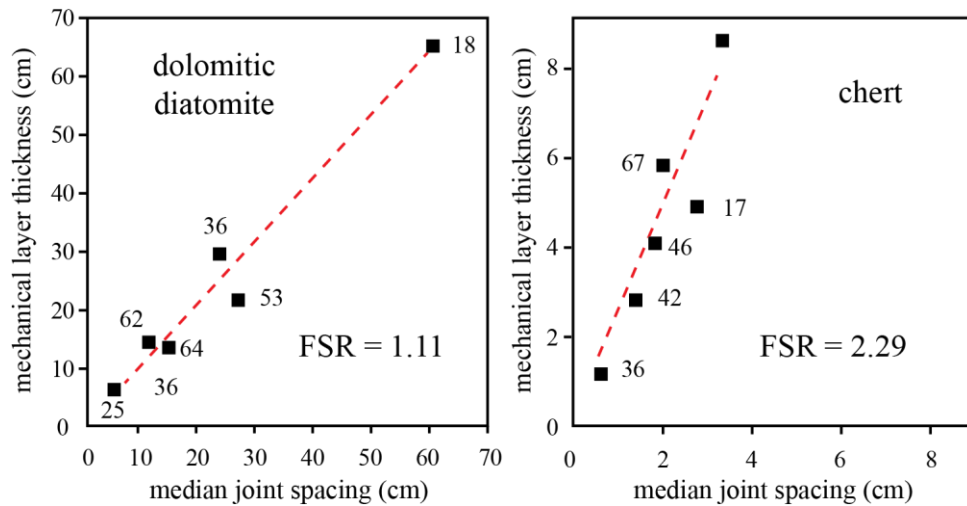


FIGURE 8. Fracture spacing ratios (FSR) previously calculated for different lithologies in the Monterey Formation. Chert is the more brittle lithology and has a higher FSR (2.29) than the dolomitic diatomite (1.11). This indicates that chert will have nearly twice as many fractures than the dolomitic diatomite in a bed of the same thickness (modified from Gross et al., 1995).

A similar study of how mechanical stratigraphy relates to sedimentary lithology was done by Underwood et al. (2003), focusing on the Silurian dolomite of northeastern Wisconsin. The study addressed the effectiveness of different types of stratigraphic

horizons in terminating opening mode fractures. After quantitative data collection, they used a stochastic predictive model to predict mechanical stratigraphy and fracture patterns from empirical relationships between sedimentary stratigraphy and the interpreted mechanical stratigraphy.

Their data show that only 63% of mud horizons interbedded within the Silurian Dolomite acted as mechanical layer boundaries. Also, that correlating mechanical interfaces with stratigraphic layering yields a range of error from 13 to 33%. This study showed that not all lithologic units of different mechanical properties functioned as a mechanical layer boundary. Rijken and Cooke (2001) applied the finite element method (FEM) to evaluate the influence of shale ductility within the Austin Chalk, Texas on the vertical connectivity of fractures. Their model predicts that for any chalk thickness, there is a critical shale thickness below which fractures will abut against shale, and above which fractures will propagate through the shale layer.

#### Previous Geologic Studies of the Field Area

The strata comprising coastal outcrops at Montaña de Oro State Park have been referred to as both the Monterey Formation and the Pismo Formation; however, it is officially designated as the Miguelito Member of the Pismo Formation (Stanley and Surdam, 1984). This study follows the nomenclature of Stanley and Surdam (1984) and refers to the studied section as the Miguelito Member of the Pismo Formation. Early studies of the Pismo Formation and surrounding sedimentary basins were published by Fairbanks (1904), Hall (1973a), Stanley and Surdam (1984), and Chipping (1987) and provided the structural and stratigraphic framework for later workers.

The most recent geologic investigation completed along the California coast in the San Luis Obispo region was done by PG & E in 2011, and focused on the major faults and geologic hazards that surround the Diablo Canyon Power Plant south of Point Buchon. The report compiled several different types of data, including aerial LiDAR (light detection and ranging), geodetic, magnetic, gravity, multibeam seafloor bathymetry, seismic reflection, and earthquake focal mechanisms to assess geologic hazards in the vicinity of the El Diablo Canyon nuclear power plant. The PG & E (2011) report reviewed the local geology and tectonic setting, but the main focus was on the potential seismicity of local faults, as well as mapping a previously unknown fault proximal to the power plant named the Shoreline fault zone.

Most of the detailed work accomplished at Montaña do Oro can be found in field guides which provide detailed descriptions of sedimentologic, stratigraphic, and structural features. Keller's (1992) study focused on the stratigraphy and sedimentology at Montaña de Oro in the Miguelito Member of the Pismo Formation and was the first to date the strata within the park. Approximately 280 meters out of 360 meters of section were measured and described north of Spooner's Cove to a synclinal axis roughly 0.9 km south of Hazard Creek (Figure 2).

Schwalbach and Bohacs (1992) described approximately 328 meters of stratigraphic section at Shell Beach and Point Buchon. This study focused on illustrating a fine-grained sequence stratigraphic analysis framework. Magnetostratigraphic, micropaleontologic, spectral gamma-ray data, and field observations were used to place hemipelagic deposits into a chronostratigraphic framework to better understand environments with time-transgressive lithofacies. Integrating these types of data can aid

in understanding the distribution of sedimentary rocks as a function of subsidence, sediment supply, and relative eustatic sea level. Field techniques described by Schwalbach and Bohacs (1995) provide a model of how sequence stratigraphy in the Monterey Formation can be interpreted by understanding the depositional environment defined by vertical succession of strata linked with biofacies analysis. The cycles present within the rocks at Montaña de Oro State Park likely reflect a combination of sequence stratigraphic cycles along the continental margin and Milankovitch scale climatic cycles.

## CHAPTER 2

### METHODS

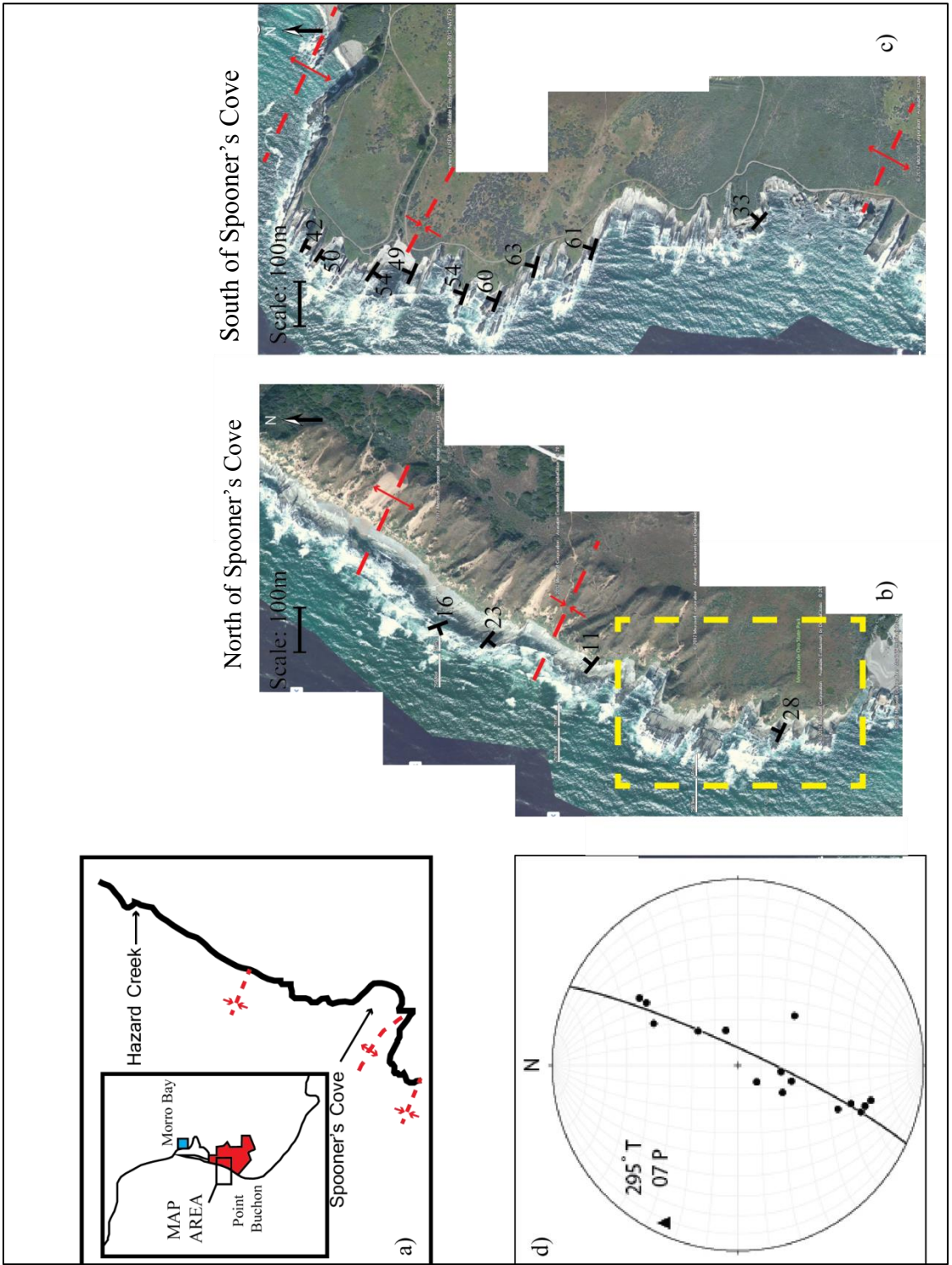
#### Selection of Study Area

Montaña de Oro State Park, Los Osos, California was chosen to study well-exposed fracture networks within the Monterey Formation-equivalent rocks. Montaña de Oro has been the site of many professional and educational field trips in the past to examine both the stratigraphy of these Monterey-equivalent rocks and their style of deformation. The first step was to find an area that was satisfactory to study the relationship between variations in stratigraphy and fracture networks.

Because fracture density and mechanical stratigraphy can vary with lithology, brittleness, diagenetic grade, bed thickness, and structural position (Gross et al., 1995), evaluation of the importance of individual variables can be difficult. To minimize the effect of structural position on fracture development, a structurally simple, well-exposed area was identified by mapping bedding orientation and structural features within and adjacent to the Montaña de Oro area (Figure 9). A section was chosen north of Spooner's Cove that rests on the north limb of a WNW-ESE-trending anticline. The approximately 200 meter-thick stratigraphic section (about 400 meters of surface exposure) is homoclinally dipping 25°-30° to the north throughout the study area. Bedding data plotted as poles in a stereonet indicate a regional fold axis of 295°, 07° (trend, plunge) (Figure 9d).



FIGURE 9. Composite diagram of preliminary field mapping. (A) Index map showing mapped area within Montaña de Oro. (B) Preliminary field map of bedding measurements and fold axes north of Spooner's Cove on collected satellite images from Bing.com. (C) Preliminary field map of bedding measurements and fold axes south of Spooner's Cove on collected satellite images from Bing.com. (D) Stereonet of the regional fold axis calculated from bedding measurements taken during preliminary mapping.



### Major and Minor Lithostratigraphic Unit Designation

In order to address the effect of stratigraphy on fracture populations at different scales, both major and minor lithostratigraphic units were defined. The major lithostratigraphic unit division was done using coastal air photos (from the California Coastline Project) in which the units were defined by erosional patterns of the coastline. The coastal erosion reflects the overall porcelanite-to-mudstone ratio in the stratigraphy because porcelanite is much more resistant to weathering in comparison to mudstone. After the major units were defined, they were then subdivided into minor lithostratigraphic units (or subunits).

The minor unit division was based on changes in characteristic bed thickness of mudstone or porcelanite, and the relative amount of porcelanite to mudstone ratio. For example, if a major unit was dominated by thin-bedded cherty porcelanite interbedded with thin mudstone and the section just below was medium-bedded porcelanite interbedded with thin-medium bedded mudstone, then that major unit would have two subunits. The subunit designation reflects changes in the lithostratigraphy at the meter scale. Approximately ten bed thickness measurements of both porcelanite and mudstone were made in each subunit in order to calculate the minimum, maximum, average, and median for each lithology. To calculate an estimate of the porcelanite to mudstone ratio (porcelanite:mudstone) in each subunit, the average porcelanite bed thickness was divided by the average mudstone thickness.

The total stratigraphic thickness of the field area was approximately 200 m as measured by tape measure and trigonometrically corrected. Each subunit was measured with a tape measure held horizontal and perpendicular to the strike of bedding. To

correct for true stratigraphic thickness, a sine correction of the average dip angle ( $28^\circ$ ) was calculated from the horizontally measured length. The true stratigraphic thickness of each subunit was then summed in each unit, defining the stratigraphic thickness of the major units. However, major units 3 and 7 do not have subunits, and their thickness was measured in the same way as the individual subunits.

#### Hand-Held Spectral Gamma-Ray Data

Gamma-ray spectrometers designed for the mining and petroleum industry measure radiation in three energy windows characteristic for the decay emission from uranium, thorium and potassium. The measured energy is calibrated at the factory to be indicative of concentration of the three elements in ppm for uranium and thorium and weight percent for potassium levels present within the surrounding rock, depending on the morphology of the bedding surfaces. The unit used for the survey is a Radiation Solutions, Inc. BGO Super Spec RS 230 (Figure 10) on loan courtesy of ExxonMobil. This machine measures omnidirectionally in a sphere with a diameter of approximately one-half meter (Kevin Bohacs, written comm., 2012). The elemental data from the gamma ray survey was used to interpret lithologic variation and stratal stacking, which influences the subsequent expression of deformational style and the resulting mechanical stratigraphy (Schwalbach and Bohacs, 1995). In addition, the gamma-ray survey is the only lithologic data collected in the study that can be directly correlated to the subsurface in onshore and offshore oil wells in the region for future study.

In order to capture the elemental variation of uranium, thorium, and potassium at high resolution, measurements were taken every 25 stratigraphic-centimeters throughout the field area in traverses parallel to the dip direction. The distance was measured either

horizontally, correcting for the sine of the dip angle, or by summation of stratigraphic heights of beds, depending on the morphology of the ground surface. For every station measured, the machine was oriented parallel to the strike of the beds, facing east in order to try to minimize the error associated with changing orientation.



FIGURE 10. Field photograph of the gamma-ray spectrometer. Recorded measurements were oriented parallel to the strike of bedding and facing east.

Using the values of uranium, thorium, and potassium, a total gamma-ray curve was calculated in API units using the formula  $(8 \times U) + (4 \times Th) + (16 \times K)$  according to Ellis (2007). There are a few sections in the field area that were not accessible for gamma-ray measurements and are represented by gaps in the gamma-ray data.

## Fracture Data

Natural fractures in rock occur at many scales, from the microscopic as observed in thin section to megascale features identifiable on air photos and satellite images. For this study, a four-order fracture designation has been constructed to help define the elements of fracture architecture and mechanical stratigraphy (Figure 11). First-order features are fractures and faults that span the length of one or more first-order major lithostratigraphic units (tens of meters). Second-order features are linked multilayer features (third-order) that cross-cut the stratigraphy on the meter scale to tens of meter scale. Third-order features are those that span multiple beds by the linkage of bed-confined fractures. Fourth-order features are bed-confined fractures, meaning that the height of the fracture is equal to the lithologic thickness of a single bed.

In order to accurately characterize the fracture network at Montaña de Oro, the following procedure was developed: (1) measure and number features (orders 1–3), measurements include orientation, length, width, offset, fracture type and order and map them on a photographic base; (2) measure a scanline parallel to bedding strike approximately every 15–20 meters throughout the study area to intersect previously mapped high order features to capture their frequency and cumulative length of features intersected (Figure 10); and (3) measure at least one scanline of bed-confined fractures in each subunit, one in mudstone and one in porcelanite (if possible), parallel to bedding strike focusing only on the fourth-order features (Figure 11). Measurements taken include scanline trend and plunge, local bedding orientation, bed thickness, fracture orientation, height, and distance along the scanline.





Rank	Photo	Description
1st Order		Fractures and faults that span the length of an ocean-cut platform or greater.
2nd Order		Fracture networks that have formed through the linkage of multilayer fractures that cross-cut the stratigraphy at a meter scale.
3rd Order		Fractures that have grown to span multiple beds through the initial linkage of bed-confined fractures.
4th Order		Fractures that initiate and terminate in a single bed, so that the height of the fracture is the same as the bed thickness.

FIGURE 11: Description of 1<sup>st</sup>, 2<sup>nd</sup>, 3<sup>rd</sup>, and 4<sup>th</sup> order fractures with corresponding photos.

The length measurements of the large features (fracture orders 1–3) were measured *in situ*, which is their measured trace length. Because the beds are dipping, the length measured of the features was corrected for stratigraphic length (height). To calculate the corrected stratigraphic height of the large fractures or faults, a two-step angular correction was necessary. First, the features had to be corrected so that their



orientation was perpendicular to the average strike of the bedding throughout the field area, which is  $297^\circ$ ,  $28^\circ$ NE. The perpendicular direction to bedding in the first quadrant is  $297^\circ + 90^\circ = 27^\circ$ ; therefore, the angle between the perpendicular direction of bedding is the difference between the orientation of the feature and  $27^\circ$  (or  $\alpha$ ).

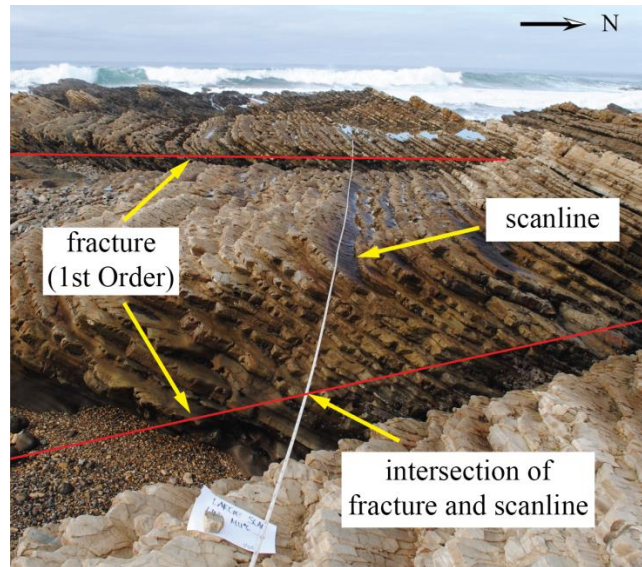


FIGURE 12. Field photograph of a large feature scanline. Annotated photograph of scanline MU6\_1 targeting fractures in orders 1–3. Scanlines were measured from east to west with a tape measure parallel to the strike of bedding.

Scanlines were measured parallel to strike and any fracture that crossed the scan line and was equal to the height of the bed was measured. The angle between feature strike and average bedding orientation ( $\alpha$ ) was used for the cosine correction for the length.  $\text{Cosine}(\alpha) * L_1$  (measured trace length) =  $L_2$ . Second, to account for the dip of the beds, the sine of the dip angle ( $\beta$ ) was then multiplied by the previous corrected



length to calculate the corrected stratigraphic height.  $\text{Sine } (\beta) * L_1 = L$  (stratigraphic length).

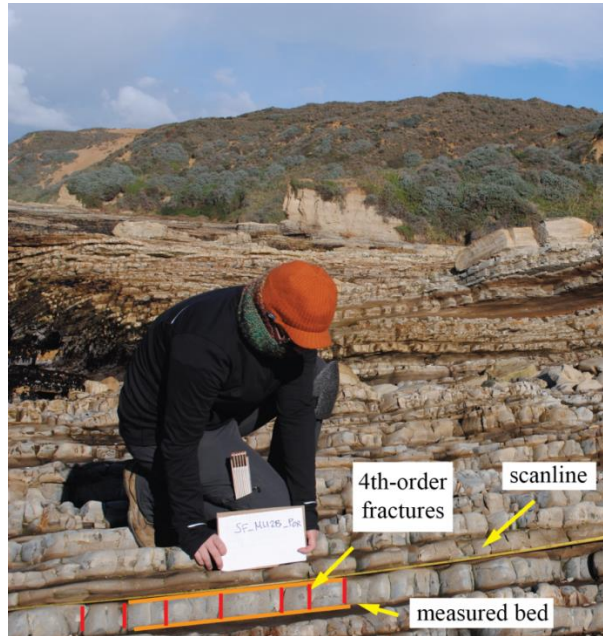
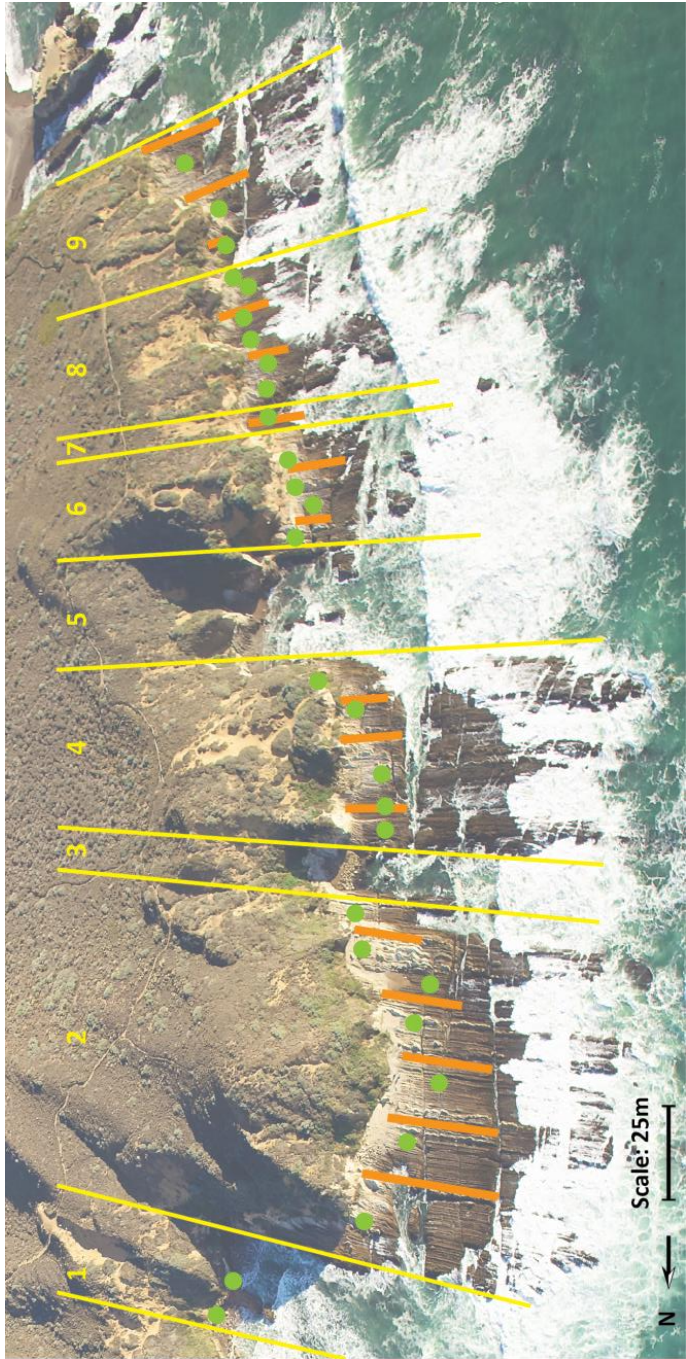


FIGURE 13. Field photograph of 4<sup>th</sup>-order scanline. Annotated photograph illustrating scanline MU2B\_Porcelanite defining the measured bed, scanline and 4<sup>th</sup>-order fractures.

In order to correct for true spacing of the fourth-order fractures, each scanline also needed an angular correction to account for the difference between the scanline trend and plunge and the average fracture strike. First, the average fracture orientation and corresponding pole along each scanline were calculated. The angle between the pole to average fracture strike and the trend and plunge of the scanline was calculated and used for a cosine correction. The cosine of the angle between the two lines was multiplied by the apparent spacing along each scan line and the result is the true spacing between each

fracture along each individual scanline. The location of each scanline is illustrated in Figure 14.

FIGURE 14. Aerial photograph of field area indicating scanline locations. Yellow lines indicate major unit boundaries, green dots are 4<sup>th</sup>-order scanline locations, and orange lines are scanline locations targeting fracture orders 1–3.



CHAPTER 3  
DATA AND RESULTS  
Stratigraphic Analysis

Major and Minor Lithostratigraphic Units

The field area spans approximately 200 meters of stratigraphic section with nine major lithostratigraphic units defined (Figure 15). The major lithostratigraphic units reflect an alternation from mud- or mudstone-dominated (odd-numbered units, except unit 9) to more siliceous packages of interbedded porcelanite and mudstone (even-numbered units). All units except units three and seven have subunits assigned to them. Units are numbered (and subunits lettered) from the top of the stratigraphic section downward. A simple stratigraphic column was created and then compared with the detailed stratigraphic column of Keller (1992) in Figure 16. Each unit and subunit was measured for length and minimum, maximum, and average bed thickness of mudstone and porcelanite. The results are listed in Appendix A. In general, porcelanite beds range from 3 to 13 cm thick (4.8 cm average) and mudstone beds range 1-105 cm thick (7.8 cm average). Figure 17 illustrates various types of stratal stacking and examples of “mudstone-dominated” intervals.

FIGURE 15. Photograph of major lithostratigraphic units. Major unit designation was done using coastal air photos from the California Coastline Project. There are 9 major units delineated within approximately 400 m of exposures, equating to approximately 200 m of stratigraphic section.



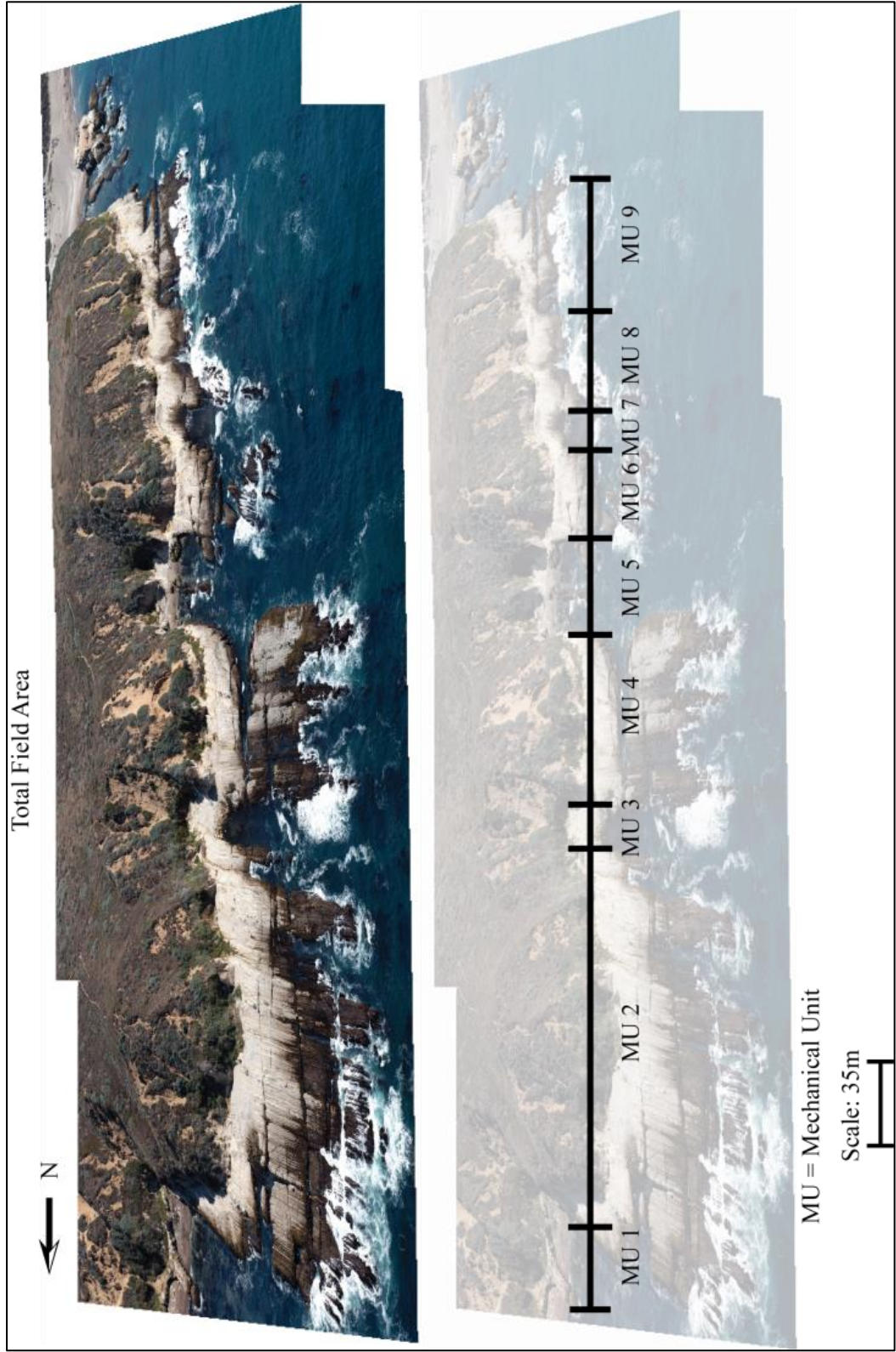


FIGURE 16. Stratigraphic columns. Measured stratigraphic column of the field area illustrating major and minor lithostratigraphic units and lithology (left). The measured section was then correlated to Keller's (1992) detailed stratigraphic section (Keller, 1992).



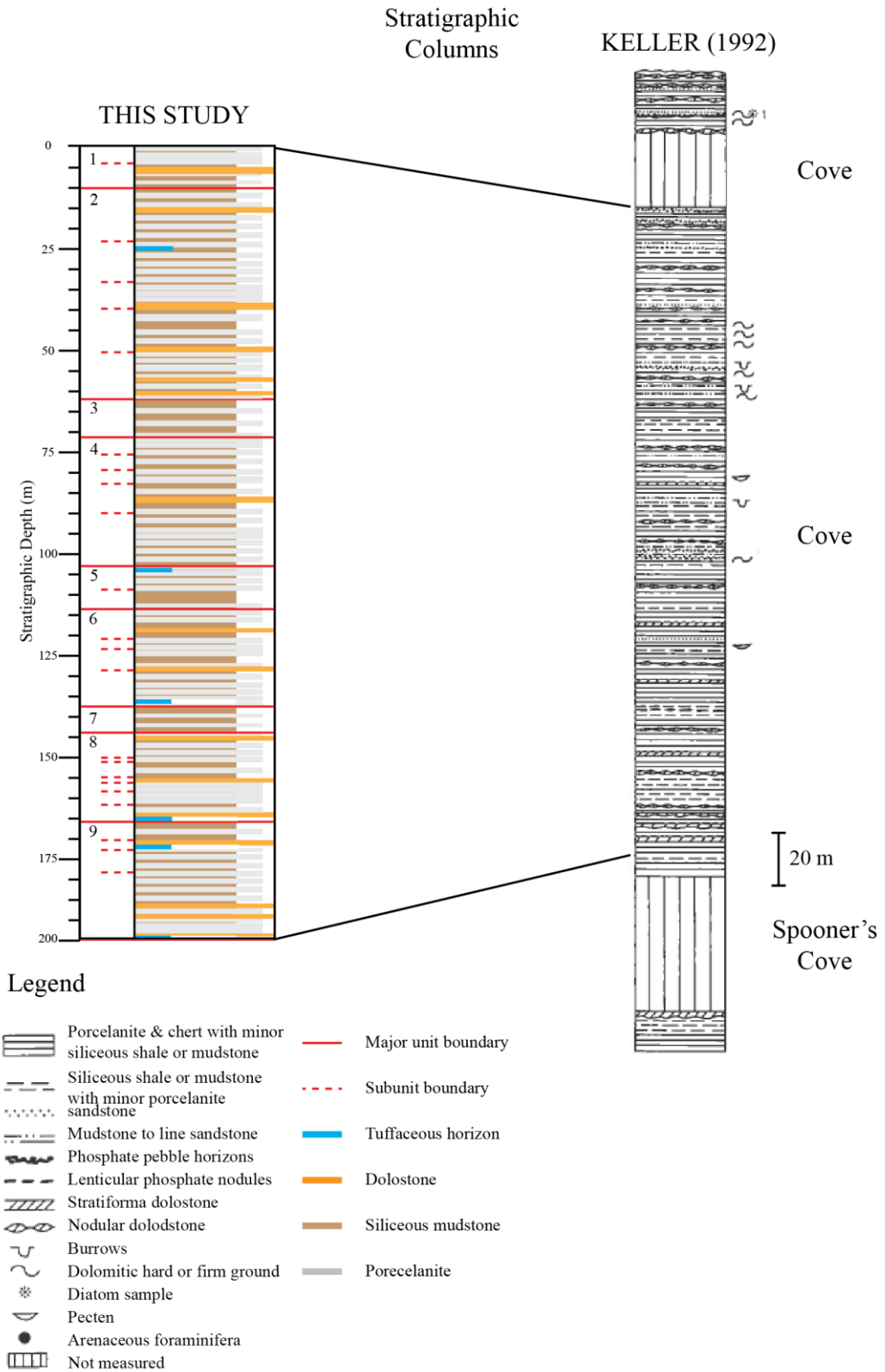
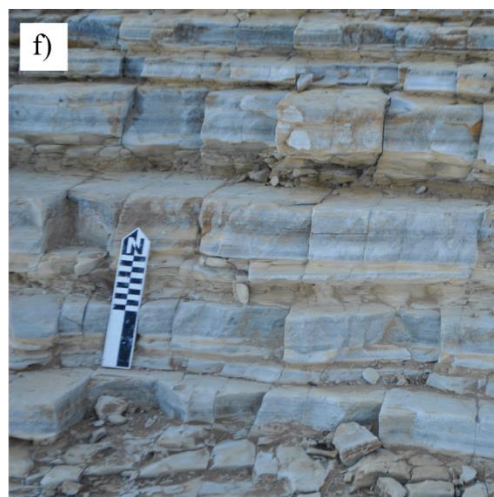
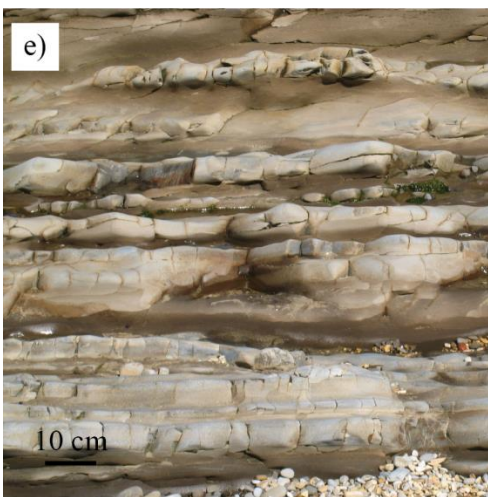
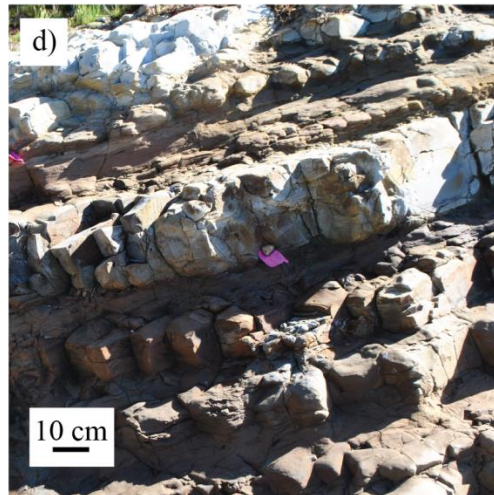
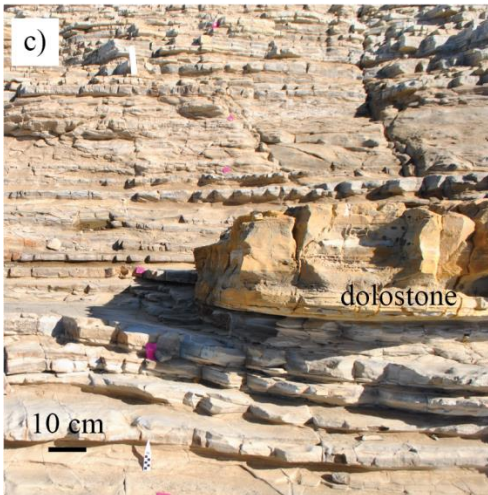
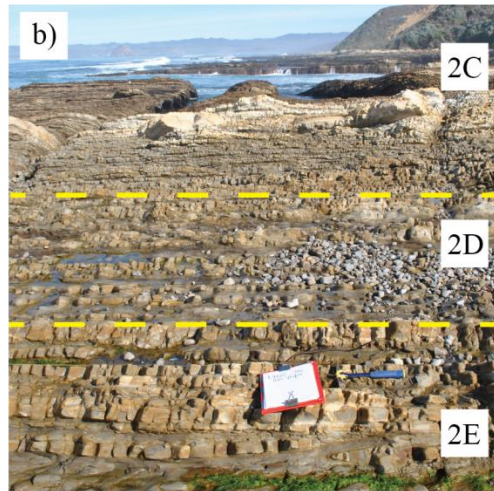
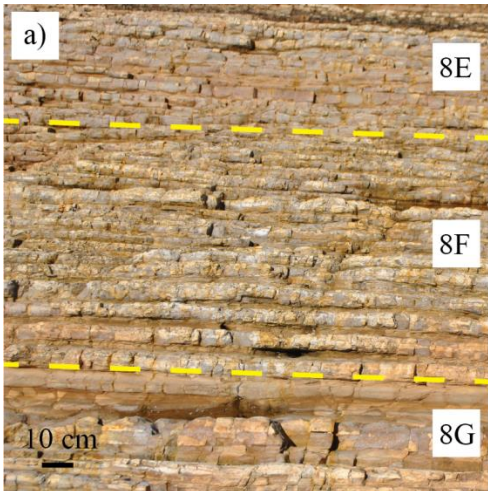


FIGURE 17. Field photographs of bedding. A) Field photograph illustrating subunits 8E-G. 8F is thin-bedded cherty porcelanite with thin interbedded mudstone, while 8E and 8G is thin-bedded porcelanite with thin interbedded mudstone. B) Field photograph illustrating subunits 2C-E. 2C and 2E is thin-bedded porcelanite and cherty porcelanite with thin interbedded mudstone. 2D is mud-dominated, with thin- to medium-bedded mudstone and thin-bedded porcelanite. C) Thin- to medium-bedded mudstone interbedded with thin porcelanite. Note nodular dolostone. D) Medium-bedded porcelanite interbedded with medium-bedded mudstone. E) Photographic example of a “mudstone-dominated” interval. F) Photographic example of a “porcelanite-dominated” interval.



Major unit 1 is approximately 13 meters thick (stratigraphically), is mudstone-dominated and has medium-bedded porcelanite with slightly thicker medium-bedded intervening mudstone. Subunit 1A has thicker porcelanite and interbedded mudstone than subunit 1B. 1A has an average porcelanite thickness of 11.3 cm and the average mudstone thickness is 13.9 cm, while 1B has averages of 7.4 cm and 8 cm, respectively. There is one thick-bedded dolomite in the central area of the unit, forming a prominence within the unit.

Major unit 2 is the thickest defined major lithostratigraphic unit with a total stratigraphic thickness of approximately 52 meters. There are five subunits within major unit two: A, B, C, D, and E. Subunit 2A has a few thick-bedded (approximately one-half meter) mudstone beds with a phosphatic pebble conglomerate at the base, thin-to medium-bedded porcelanite, and a few nodular dolostone horizons. The average porcelanite bed thickness is 5.8 cm and the average mudstone thickness is 11 cm. Subunit 2B has thin-bedded cherty porcelanite, porcelanite, mudstone, and a few nodular dolostone horizons. The average porcelanite thickness is 5.5 cm and the average mudstone thickness is 3.8 cm. Subunit 2C has thin-bedded porcelanite (mainly cherty) having consistent bed thickness (5.7 cm average), interbedded with slightly thicker mudstone (5.9 average) than subunit 2B, and more dolostone horizons than 2A and 2B.

Subunit 2D is the only mud-dominated subunit in unit 2, meaning that mudstone comprises greater than 50% of the thickness of the unit. The majority of the mudstone beds are thin-to medium-bedded (9.7 cm average) with thin-bedded porcelanite layers (5.9 cm average), and has less cherty porcelanite than unit 2C. Subunit 2E has the “chertiest” or most siliceous porcelanite in unit two, characterized in the field by closely

spaced, conchoidal and chaotic fracturing. The average porcelanite thickness is 5.8 cm and the average mudstone thickness is 2.7 cm. There is one thick-bedded mudstone with a basal phosphatic pebble conglomerate at the base of the subunit; however the majority of the mudstone beds within the unit are very thin-to thin-bedded.

Unit 3 is mudstone-dominated with a thickness of nine meters. This unit is one of the thinnest major lithostratigraphic units and does not have any associated subunits. There is a thick mudstone (approximately 1 m) at the top of the unit. It is poorly exposed due to erosion and coverage by beach sand therefore average beds thicknesses for mudstone and porcelanite were not measured.

Unit four has four subunits: A, B, C, and D. Subunit 4A is the “chertiest” subunit within unit four. It has thin to medium-bedded cherty porcelanite (4.9 cm average) with thin interbedded mudstone (2.3 cm average). Subunit 4B is the only mud-dominated subunit within unit four, and consists of thin-to medium-bedded mudstone (6.8 cm average) and thinly bedded intervening porcelanite (4.9 cm average). Dolostone beds are not present in 4B, however there is one dolomitic horizon in 4A. Unit 4C has thin-bedded porcelanite (5.5 cm average) gradually becoming more cherty near the top of the unit and has thin interbedded mudstone (3.75 cm), and a few nodular dolostone horizons. Near the top of 4D there is a thick mudstone with a thin, irregular basal phosphatic pebble conglomerate and this is the thickest mudstone bed in the unit. Subunit 4D is a mixture of porcelanite and cherty porcelanite (5.3 cm average), the mudstone thickness is highly variable, ranging from 4-80 cm and there is one dolostone horizon. Subunit 4E is mainly thin-bedded porcelanite and cherty porcelanite (4.4 cm average) with thin interbedded mudstone (3.2 cm average).

Major unit 5 is the thickest mudstone-dominated unit at approximately 12 meters and is divided into two subunits. Subunit 5A has a thick-bedded mudstone near the top and two smectitic and illitic altered tuff horizons that are approximately 1–2 cm thick. The mudstone (4.2 cm average) is highly burrowed and the porcelanite in 5A is thin to medium-bedded (2.8 cm average). Subunit 5B has a thick mudstone in the upper section and is the thickest mudstone (approximately 1 m) in the entire field area. Mudstones in this unit have highly variable thickness, ranging from 6 to 105 cm (27 cm average), can be massive or burrowed and the porcelanite is thin-to medium-bedded (5.6 cm average).

Unit 6 has subunits A, B and C. Subunit A contains two thick mudstone beds with a basal phosphatic pebble conglomerate (Figure 18). The main difference between unit five and 6A is that the porcelanite has relatively consistent thin bed thicknesses (5 cm average). Subunit 6B is mud-dominated with thin-to medium-bedded mudstone (7.7 cm average) and thin-bedded porcelanite (5.6 cm average). Subunit 6C is slightly more mudstone-rich near the upper part of the subunit. The majority of subunit 6C has consistent thicknesses of thin-bedded porcelanite (4.6 cm average) with thin-bedded mudstone (3.2 cm average), and a few nodular dolostone horizons. There is a tuff horizon 2 cm thick near the base of 6C that serves as a mechanical layer boundary to many fractures in orders 1–3 (Figure 19).

Six-meter-thick unit 7 is mudstone-dominated and the thinnest major lithostratigraphic unit. Mudstone beds are medium-bedded (4.5 cm average) with thin interbedded porcelanite (4.9 cm average), and there are no dolostone horizons. Unit 8 has seven subunits: A, B, C, D, E, F, and G. Subunit 8A has a few nodular dolostone horizons and is dominated by thin-to medium-bedded porcelanite (6.6 cm average) with

thin-bedded mudstone (2.6 cm average). Unit 8D is the only mudstone-dominated subunit within unit 8. The average mudstone thickness is 10.8 cm and porcelanite thickness averages 4 cm. Most of the unit contains relatively consistent thin-bedded porcelanite (4.3 cm average) and thin-bedded mudstone (4.2 cm average), however, subunit 8F is markedly more siliceous consisting of cherty porcelanite. Subunit 8G contains a thin (~ 1 cm) tuff near the base that is a very effective mechanical layer boundary (Figure 20).

The southernmost unit, unit 9, consists of three subunits: A, B, and C. Subunit 9A is mudstone-dominated (16.2 cm average bed thickness) and has a thick mudstone with a basal phosphatic pebble conglomerate near the base of the subunit. The porcelanite average bed thickness is 4.5 cm. Subunit 9B, however, has consistent thin-bedded porcelanite (5.9 cm average) and thin-bedded mudstone (5.5 cm average) throughout. The mudstone beds gradually become thicker near the base of subunit 9B. Subunit 9C has thin-bedded mudstone (4 cm average) with thin-bedded porcelanite (7 cm average) throughout the section and the base contains many thin-bedded dolomitic horizons.

### Gamma-Ray Stratigraphy

The results of the spectral gamma-ray survey and the calculated total gamma-ray are shown in Figure 21. The averages of uranium, thorium, potassium and total gamma-ray in API units throughout the survey are 4.6 ppm, 4.6 ppm, 1.1 %, and 73 API, respectively. These averages are closely representative of the mean throughout the succession as it does not display any gross secular trends. Nonetheless, the upper (northern) 100 meters of the stratigraphic section have slightly lower average values in total gamma-ray than the lower (southern) 100 meters of the section.



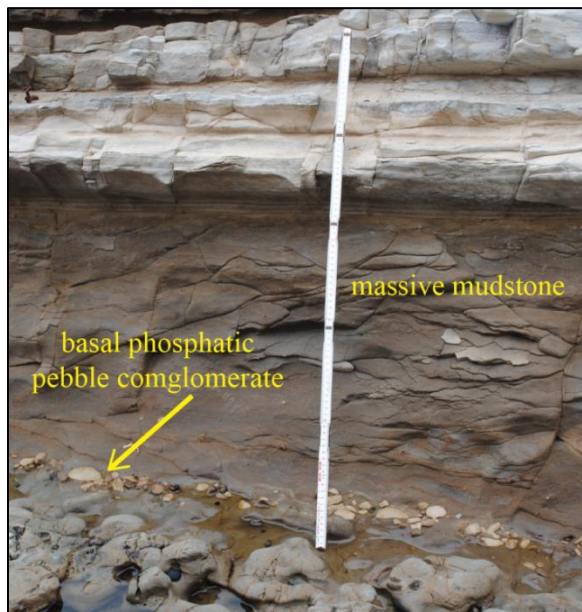


FIGURE 18. Field photo of massive mudstone with a phosphatic pebble conglomerate at its base in subunit 6A. Meter stick for scale.





FIGURE 19. Field photograph of tuff horizon near the base of 6C. This tuff horizon terminates feature #'s 8, 9, 10, 11, 70, 85, 86. It likely terminates features 60, 61, 63, 106 as well, however the exact terminations of those features could not be traced.

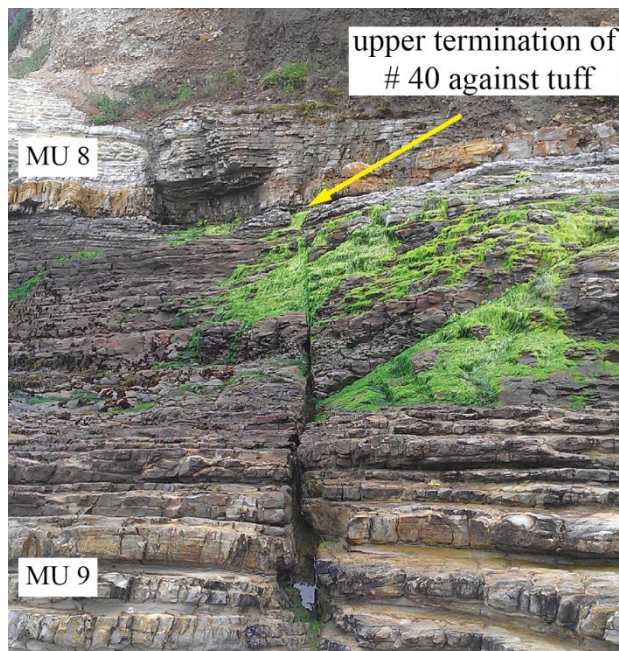


FIGURE 20. Field photograph of fracture terminations. The upper terminations of feature #40 is at a tuff horizon near the base of unit 8.

Average values of uranium, thorium, potassium, and total gamma-ray of the upper section are 4.4 ppm, 4.3 ppm, 0.99 % and 68 API, respectively, compared to averages of 4.8 ppm, 4.9 ppm, 1.1 % and 76 API, in the lower section.

The lower-100-m section is also characterized by greater variability with many more intervals of higher gamma-ray. To quantify the difference in gamma-ray values between the upper and lower sections, a baseline of 80 API units was applied. Because the section has a predominance of porcelanite beds, the baseline was chosen to be slightly higher than the average of 73 API total gamma-ray value to more clearly delineate the clay- and organic-rich mudstones from the more siliceous intervals.

The upper-section has a total of 11 m of section with values greater than 80 API units. The lower section has a total 30.25 m of section with values greater than 80 API units. Because the upper and lower sections have different stratigraphic thicknesses (upper section is 96.5 m, lower section is 92.75 m) the ratio of stratigraphic thickness greater than 80 API to total stratigraphic thickness was calculated. The upper section (96.5 m thick) has a ratio of 0.11; the lower section (92.75 m) has a ratio of 0.33. This indicates that the lower section has greater stratigraphic proportion of mudstone intervals containing detrital clay and organic matter than the upper section.

The gamma-ray results were then compared to the initial major unit designation. Figure 22 shows the major (and minor) unit-to-gamma-ray correlation using the calculated total gamma-ray curve. The areas of the curve that have higher API readings correspond to the major units that are mudstone-dominated (units 3, 5, and 7). The subunits generally correspond with the higher gamma-ray values; however there are a few exceptions in subunits 2A and 9C.

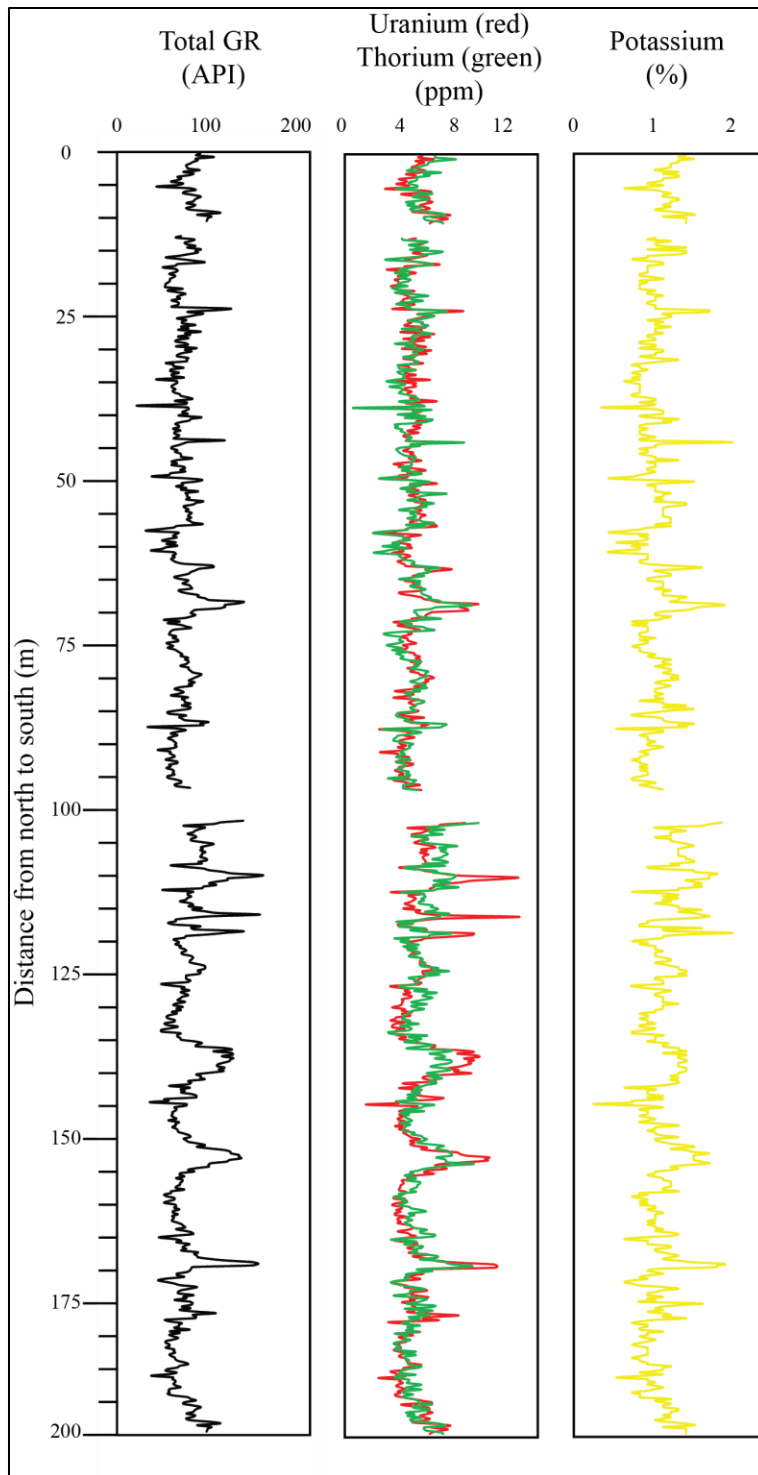


Figure 21: Graphical representation of the gamma-ray survey. From left to right: total calculated gamma-ray in API units; uranium and thorium readings in ppm; potassium in total percent of readings.

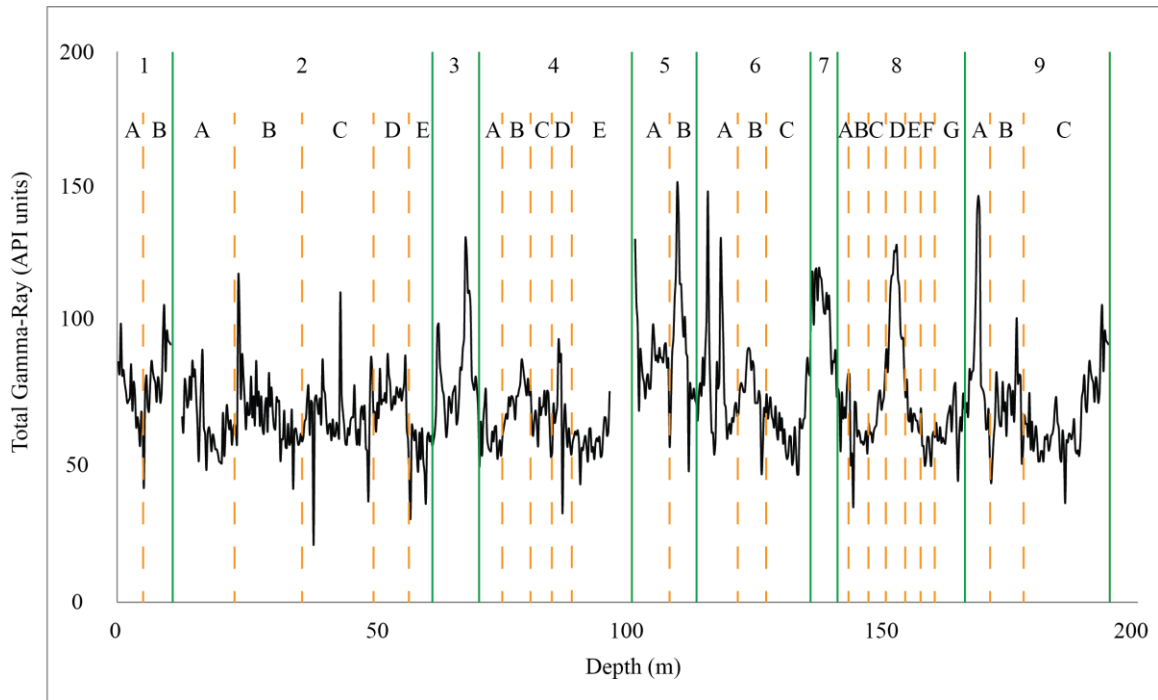


FIGURE 22. Correlation of total gamma-ray to major and minor units. Total gamma-ray curve with major units (in green) and subunit (dashed orange lines) boundaries.

### Structural Analysis

Four orders of fractures were measured in the field. For the following spatial and statistical analysis, I measured the following features: one-thousand 4<sup>th</sup>-order features (bed-confined fractures), fifty-seven 3<sup>rd</sup>-order features (linked multilayer fractures), forty-six 2<sup>nd</sup>-order features (meters to tens of meters), and eight 1<sup>st</sup>-order features (span an entire major lithostratigraphic unit). The following data and results are separated into 4<sup>th</sup>-order fracture analyses and larger feature (fracture orders 1–3) analysis. All feature orientations were measured using the right hand rule (the dip directions is in the quadrant to the right when looking in the direction of the strike azimuth). Stereoplots of all

fractures are shown in the following sections and the stereoplot of bedding measurements can be found in Appendix B.

#### 4<sup>th</sup>-Order Fractures

The 4<sup>th</sup>-order (bed-confined) fractures were measured independently of fracture orders 1-3. The scanlines were not measured adjacent to higher order fractures because large fractures and faults often have a zone of higher fracture intensity surrounding them. In order to acquire more accurate 4<sup>th</sup>-order fracture population statistics, the larger fractures were thus avoided in scanline measurements. In each scanline, the average fracture orientation, average spacing, median spacing, mechanical layer thickness (or equivalent to fracture height), and the number of fractures per scan line were determined. The fracture spacing ratio (FSR) was then calculated for each bed, which is the mechanical layer thickness divided by the median value of fracture spacing for that bed (Gross et al., 1997; Gross and Eyal, 2007).

The FSR provides a quantitative measure of fracture intensity that normalizes for bed thickness (similar to the FSI of Narr and Suppe, 1991), and has been used to evaluate effects of lithology on fracture spacing (Gross et al., 1995) as well as to map variations in fracture strain for the same lithology as a function of structural position or tectonic stress (Becker and Gross, 1996; Gross et al., 1997; Eyal et al., 2001; Gross and Eyal, 2007). Results from each scanline are shown in Appendix C. The average FSR for porcelanite scanlines is 0.79, and the average FSR for mudstone scanlines is 0.61. There are many more scanlines in porcelanite beds than mudstone beds because the mudstone beds in the field area are recessively eroded and highly weathered, making it difficult to collect fracture data.

Orientation data of the 4<sup>th</sup>-order fractures in both porcelanite and mudstone are shown in Figure 23 (mudstone data is brown, porcelanite data is light blue). Data for 4<sup>th</sup>-order fractures are separated by lithology to address the effect of lithology on orientation and fracture spacing. The average orientation of bed-confined (4<sup>th</sup>-order) fractures in porcelanite throughout the field is 209°, 84°W, striking roughly parallel to the regional NNE-SSW  $SH_{max}$  direction (Vittori et al., 1994; Finkbeiner et al., 1997) and perpendicular to local bedding strike and the calculated regional fold axis for Montaña de Oro (Figure 9d). Mudstone bed-confined fracture orientation is much more variable than those in porcelanite. However, the mean orientation of 4<sup>th</sup>-order fractures in mudstone is 219°, 82°W, which is within 10° of the orientation of the 4<sup>th</sup>-order fractures in porcelanite.

Histograms of fracture spacing for combined data for all porcelanite and mudstone beds are shown in Figure 24. Fracture spacing in porcelanite has an average, median, and standard deviation of 9.02 cm, 7.76 cm, and 6.07 cm, respectively. Fracture spacing in mudstone has an average, median and standard deviation of 20.11 cm, 13.81 cm, and 22.15 cm, respectively. Both the average and median fracture spacing in the mudstone is approximately twice the value found in the porcelanite. Furthermore, the standard deviation of fracture spacing in the mudstone is nearly 4 times greater than for the porcelanite, showing that the fractures in the mudstone are much more broadly and irregularly distributed.

In previous studies of fracture spacing in layered rocks (Narr and Suppe, 1991; Gross et al., 1995; Wu and Pollard, 1995; Bai and Pollard, 2000) median fracture spacing is plotted against bed thickness and the data usually fall around a “best-fit” line.

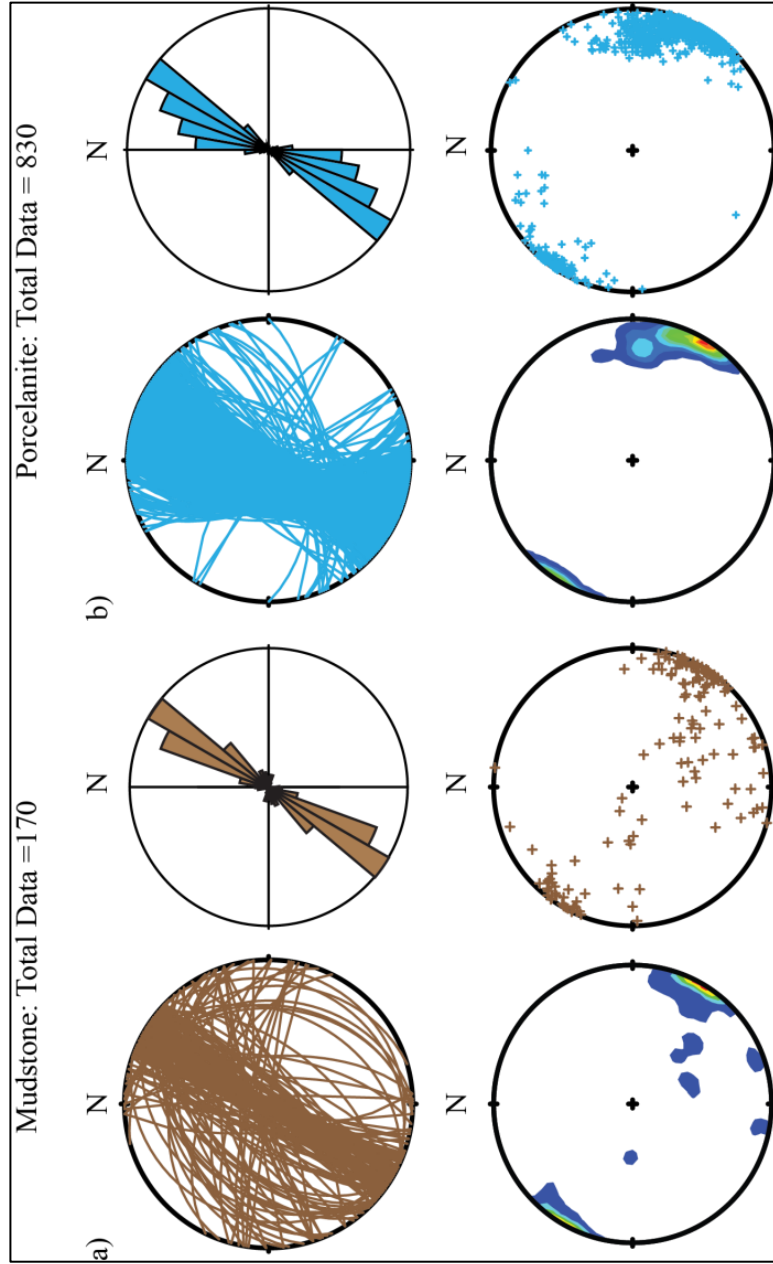


FIGURE 23. Mudstone and porcelanite stereoplots. Fracture orientation and distribution displayed as (clockwise from upper left) great circles, linear rose diagram, poles to fracture planes, and contour plot of the poles of fracture orientation. a) mudstone. b) porcelanite. Note fractures in mudstone have greater scatter in orientation. The average orientation of the porcelanite and mudstone fractures, however, are approximately parallel NE/SW.

Figures 25 and 26 are scatter plots of the median fracture spacing versus bed thickness for each 4<sup>th</sup>-order scan line in porcelanite and mudstone. The data has a great amount of scatter, so much so that a linear correlation cannot be made.

To continue consistency in our analysis, the 4<sup>th</sup>-order data was also separated between the upper (northern) and lower (southern) sections (Figure 27). The scatter plots shown in Figure 27 illustrate the difference in variability of porcelanite 4<sup>th</sup>-order fracture spacing in the upper (northern) and lower (southern) sections. The upper section data does not fall along a best-fit line as the data has a high amount of scatter. However, the lower section data does show a slight positive correlation indicating that the fracture spacing increases with increasing bed-thickness in the lower section.

The fracture spacing ratio (FSR) was calculated for each scanline and the results are shown in Appendix B. The calculated porcelanite FSR is plotted against stratigraphic depth in the field area to demonstrate variations in 4<sup>th</sup>-order fracture density between major units, and between upper and lower sections that correspond to the changes in gamma-ray character (Figure 28). Due to sparse data and higher variability in mudstone data, porcelanite data was used to analyze the spatial distribution of 4<sup>th</sup>-order fractures. Orientation, spacing and FSR of porcelanite in the upper (north) section and lower (south) section were compared and results are shown in Appendix D. The average FSR of the upper and lower sections were then calculated to compare their one-dimensional fracture densities in the porcelanite beds. The upper section average FSR is 1.15 and the average of the lower section is 0.55. This indicates that the one-dimensional fracture density of 4<sup>th</sup>-order fractures in the upper section is twice that of the lower section when normalized for bed thickness. The mudstone FSR dataset is not as robust (only 9 data



points), but it shows the same relationship of higher FSR in the northern section. The average mudstone FSR for the upper (northern) sections is 0.73 and the lower (southern) section is 0.56.

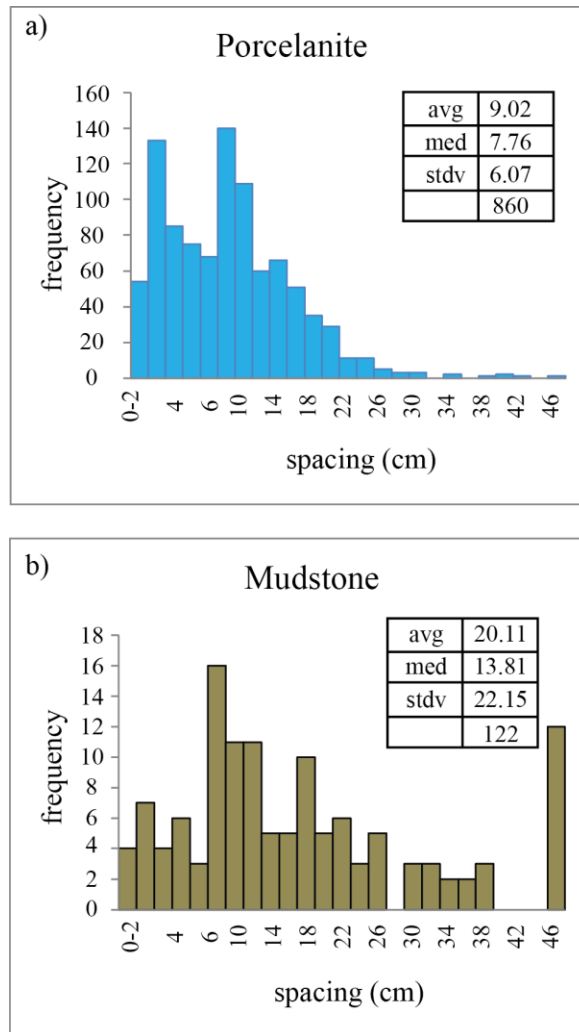


FIGURE 24. Histograms of fracture data for mudstone and porcelanite. a) histogram of all spacing measurements in porcelanite beds showing the distribution and average (avg), median (med), standard deviation (stdv), and total number of measurements (#). b) histogram of all spacing measurements in mudstone beds showing the distribution and average, median, standard deviation, and total number of measurements.

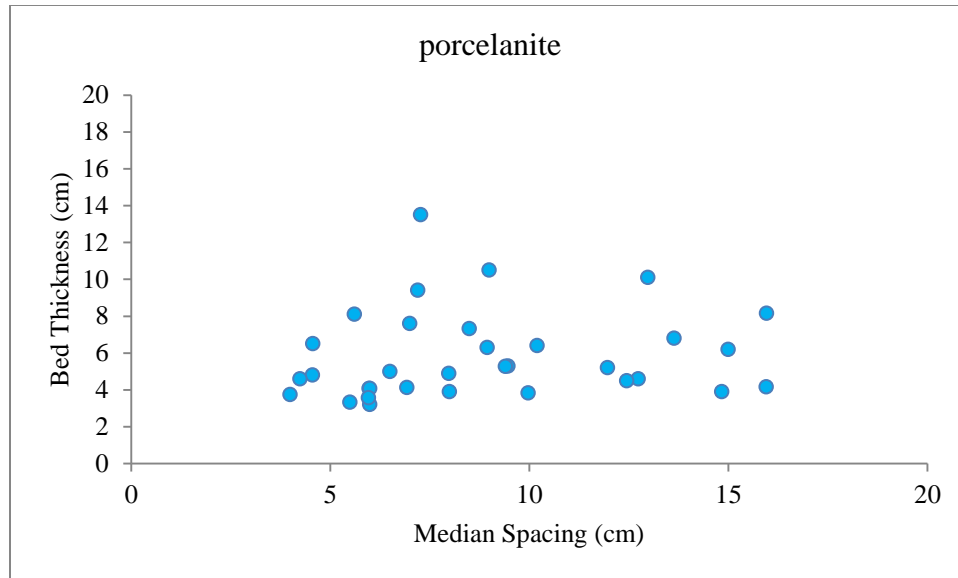


FIGURE 25. Scatter plot of 4<sup>th</sup>-order porcelanite scanline data. Median fracture spacing is plotted on the horizontal axis and bed thickness (cm) is plotted on the vertical axis.

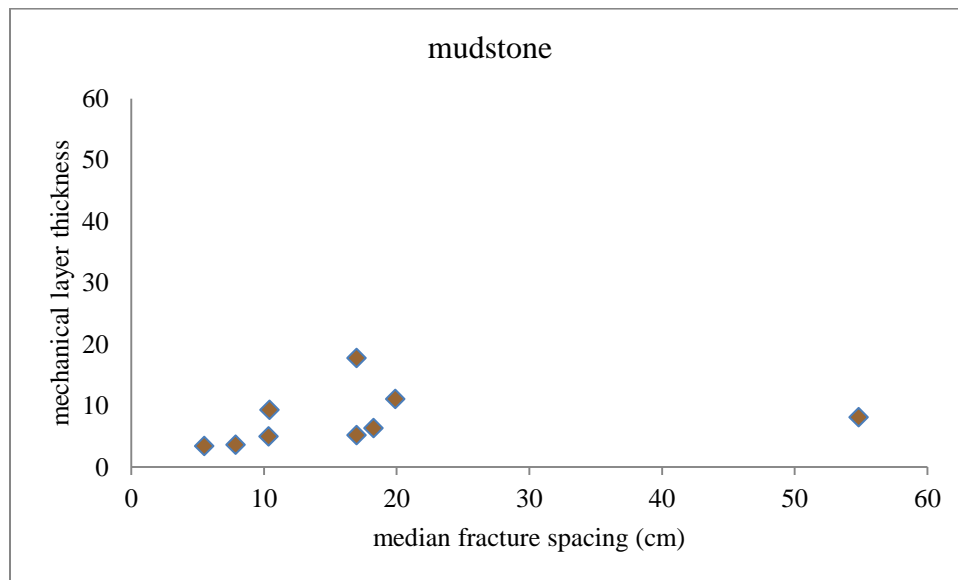


FIGURE 26. Scatter plot of 4<sup>th</sup>-order mudstone mudstone scanline data. Median fracture spacing is plotted on the horizontal axis and bed thickness (cm) is plotted on the vertical axis.

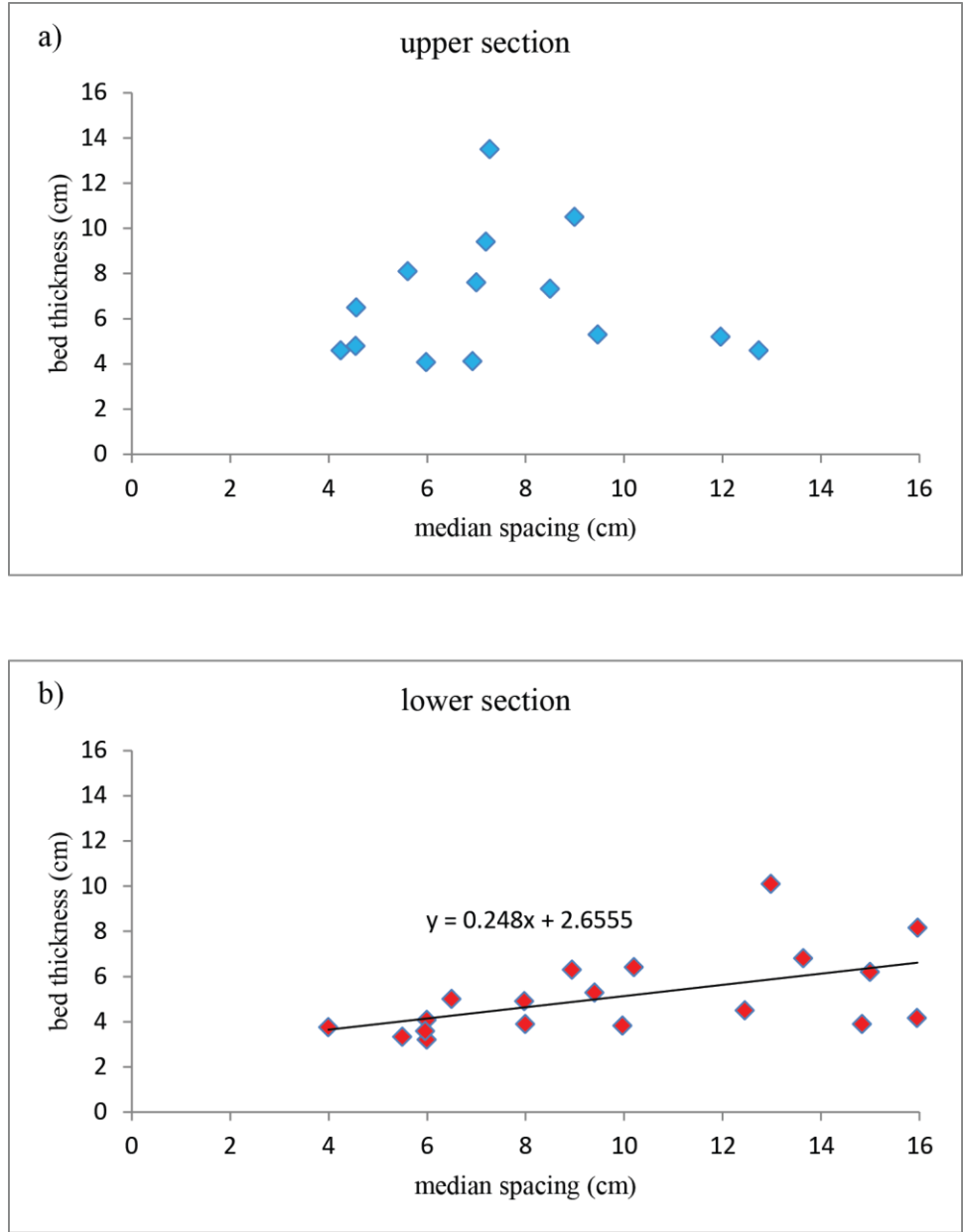


FIGURE 27. Scatter plots of 4<sup>th</sup>-order fracture spacing and bed thickness by upper and lower sections. a) scatter plot of porcelanite scanline of median fracture spacing (horizontal axis) to bed thickness (vertical axis) of the upper section of the field area. b) scatter plot of porcelanite scanline of median fracture spacing (horizontal axis) to bed thickness (vertical axis) of the lower section of the field area.

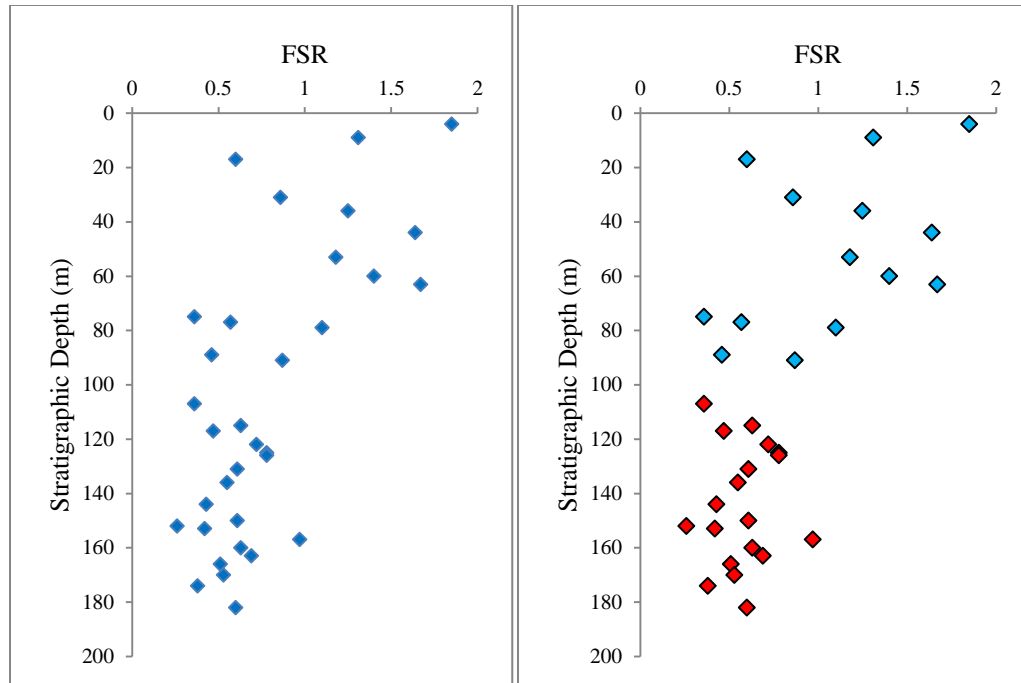


Figure 28: Fracture spacing ratio plotted with stratigraphic position. A) FSR (fracture spacing ratio) of each 4<sup>th</sup>-order scan line in porcelanite versus stratigraphic position throughout the field area. B) Highlights the upper section FSR in light blue and the lower section in maroon. Note the greater scatter and higher values in FSR in the upper section compared to the lower section.

### Fractures in Orders 1-3

A total of 109 features were mapped in the field area as fracture orders 1, 2, and 3; though only 106 had measureable strike and dip orientations. A few features had more than one segment as a splay to the main fracture trace, so there are a total of 111 features defined. There are 8 1<sup>st</sup>-order features, 46 2<sup>nd</sup>-order features, and 57 3<sup>rd</sup>-order features. A summary of measurements of the features in fracture orders 1–3 can be found in Appendix E, which includes their orientation, fracture order, *in situ length or trace* (horizontal length that was measured in the field, prior to angular correction), corrected

stratigraphic length, width, type of offset, and location in the major lithostratigraphic framework. Multiple fracture maps illustrate the spatial distribution, length, and terminations of the larger order fractures (Figures 29, 30, 31, 32, 33, 34). The maps are air-photo-based, detailing fracture orders 1–3, location of major unit boundaries, and location of tuff horizons. Histograms of fracture length, both measured trace length and corrected stratigraphic length, can be found in Figures 35 and 36.

Orientation data were then plotted to analyze the various fracture sets and to evaluate potential relationships between the mapped features and local structural elements and the regional stress regime. Orientations of the large features are presented in Figure 37, including the great circles of fracture planes, poles to fracture planes, contour plots of the poles, and a rose diagram. The linear rose diagram binned features every ten degrees. The contour plot of the poles is done every 10 counts using one percent area contouring. Further analysis of the orientation data indicates there are three distinct fracture sets (Figure 38).

Fracture Set A, which is the most dominant fracture set, has a total of 65 features and an average orientation of  $030^{\circ}/89^{\circ}\text{SE}$ . This orientation is approximately parallel to the systematic fracture set in the 4<sup>th</sup>-order fractures, and is perpendicular to the calculated regional fold axis of 295T-07P. Fracture Set B has a total of 17 features and an average orientation of  $064^{\circ}/89^{\circ}\text{SE}$ . Fracture C has a total of 16 features and an average orientation  $357^{\circ}/80^{\circ}\text{E}$ . The acute angle difference in azimuth between fracture sets B and C is 67 degrees.

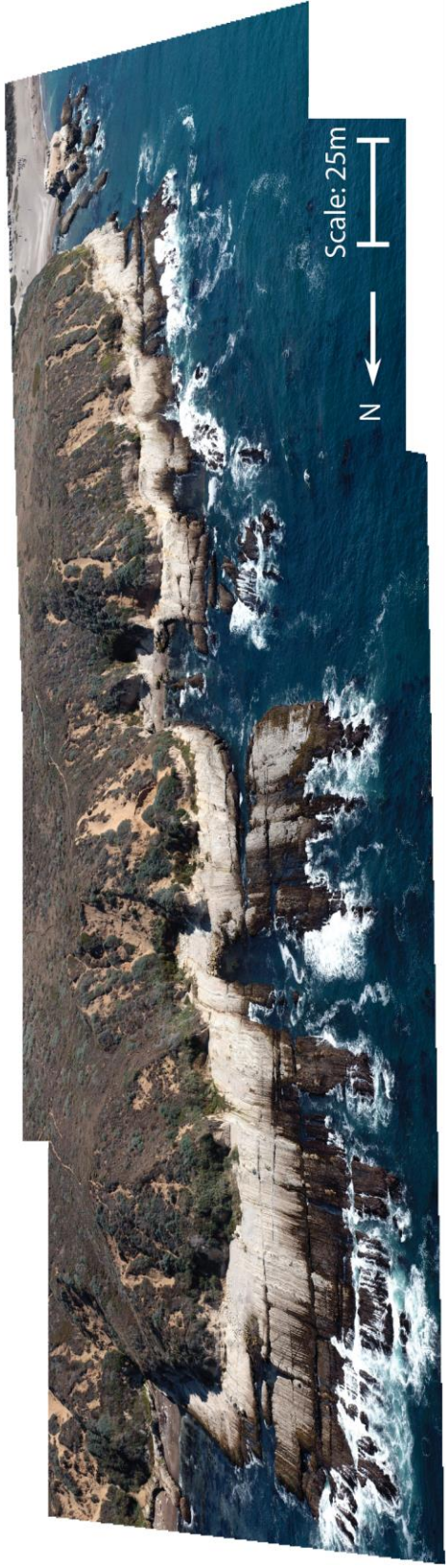


FIGURE 29. Base map for the following fracture maps in figures 30, 31, 32, and 33. Red bars indicate spatial coverages of the fracture maps.

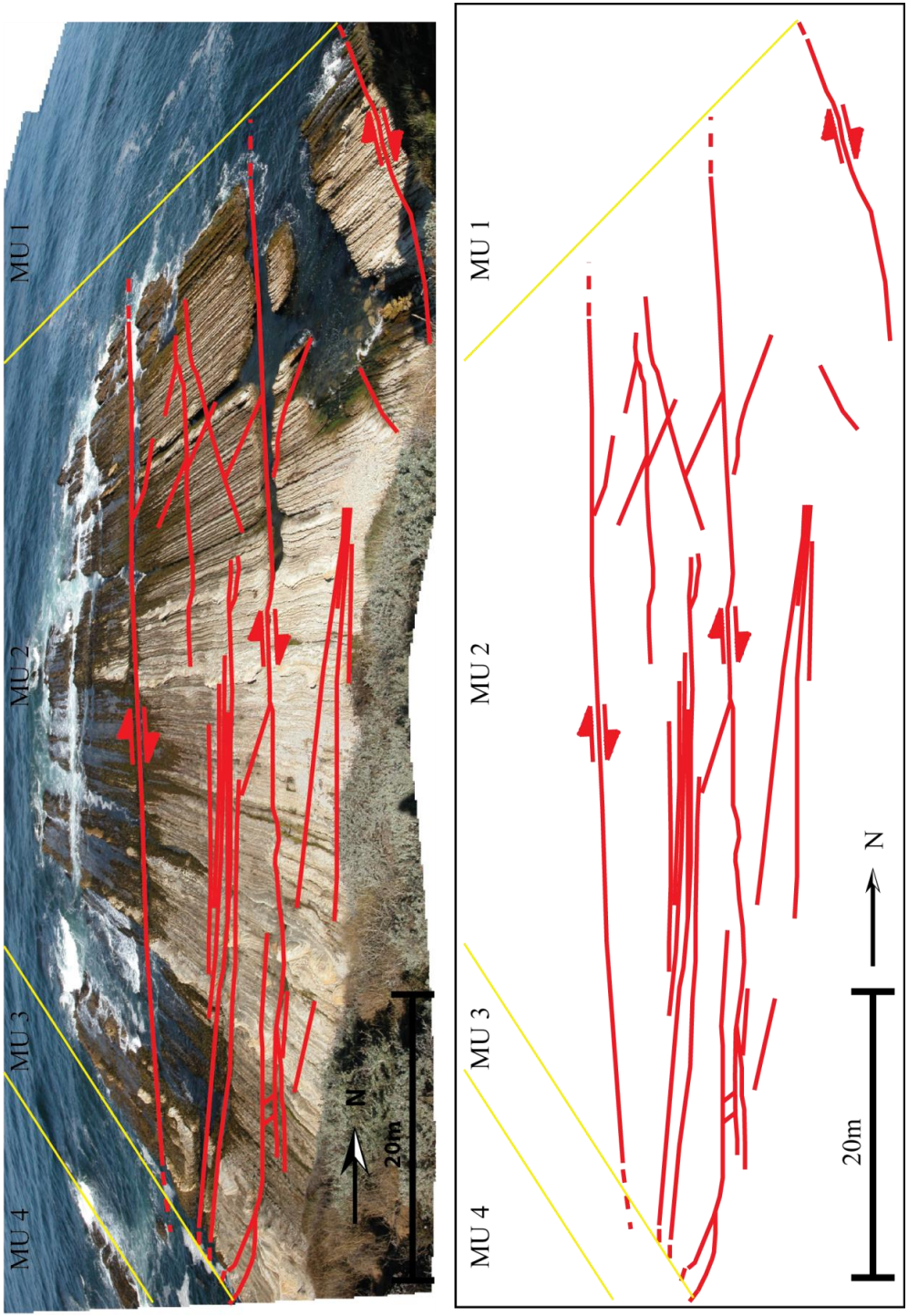


FIGURE 30. Fracture map of major unit 2. Red lines are mapped fractures in orders 1–3, yellow lines are major unit boundaries, and red arrows indicate direction of offset.



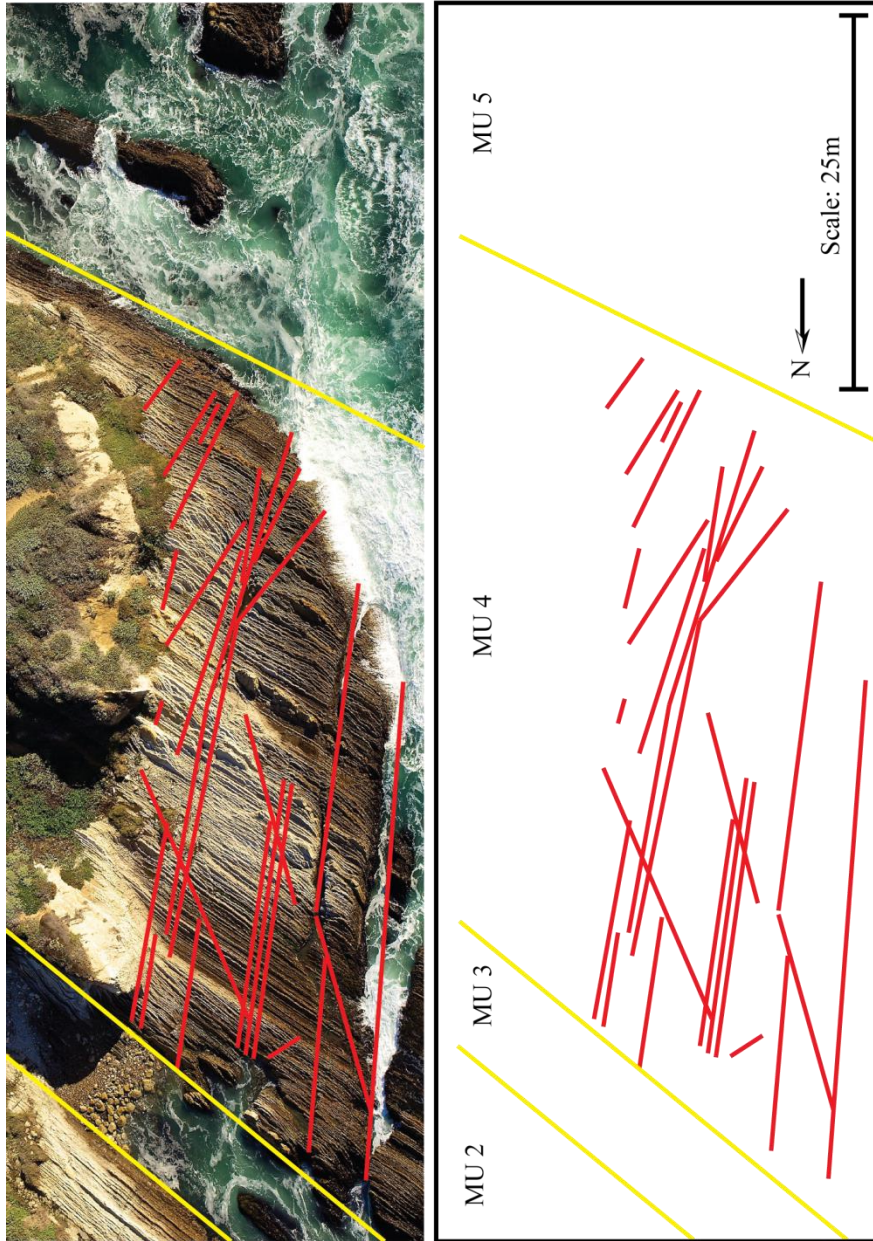


FIGURE 31. Fracture map of major unit 4. Red lines are fractures in orders 1–3, yellow lines are major unit boundaries, and red arrows indicate direction of offset.



FIGURE 32. Fracture map of major unit 4-8. Red lines are fractures in orders 1-3, yellow lines are major unit boundaries, blue lines are tuff horizons, and red arrows indicate direction of offset.

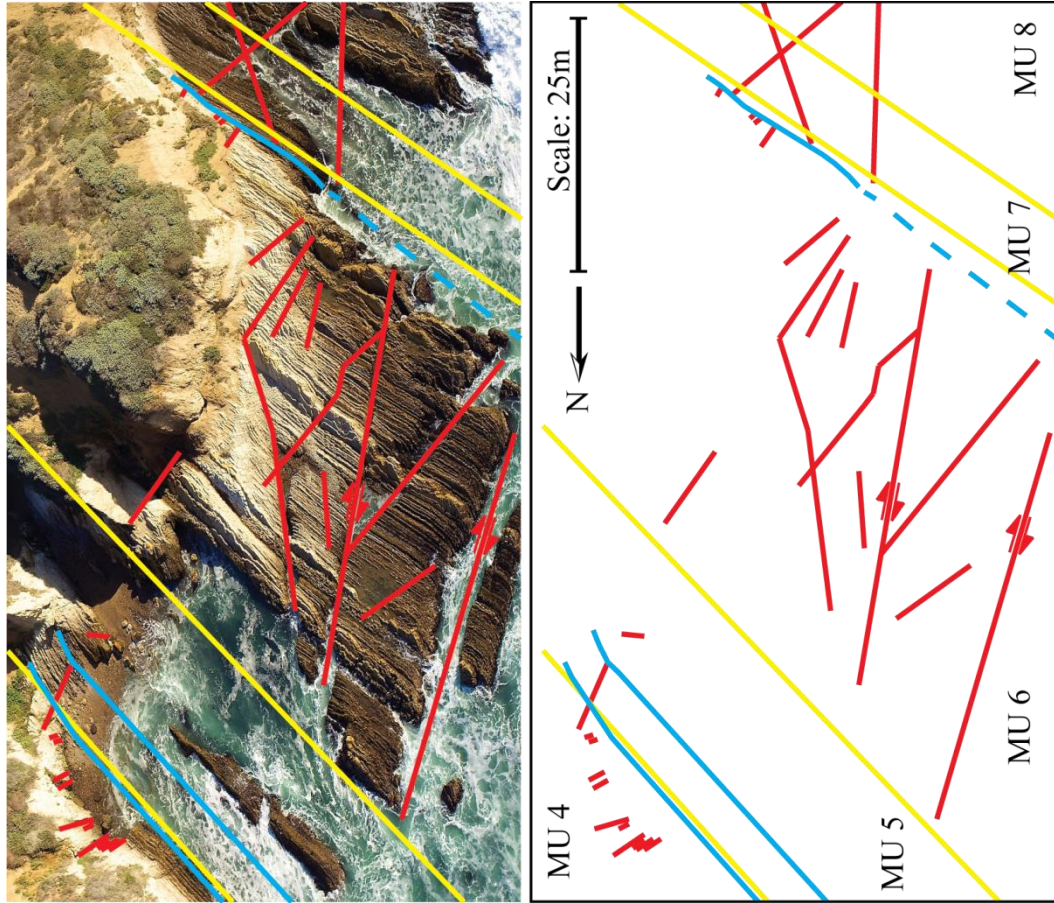
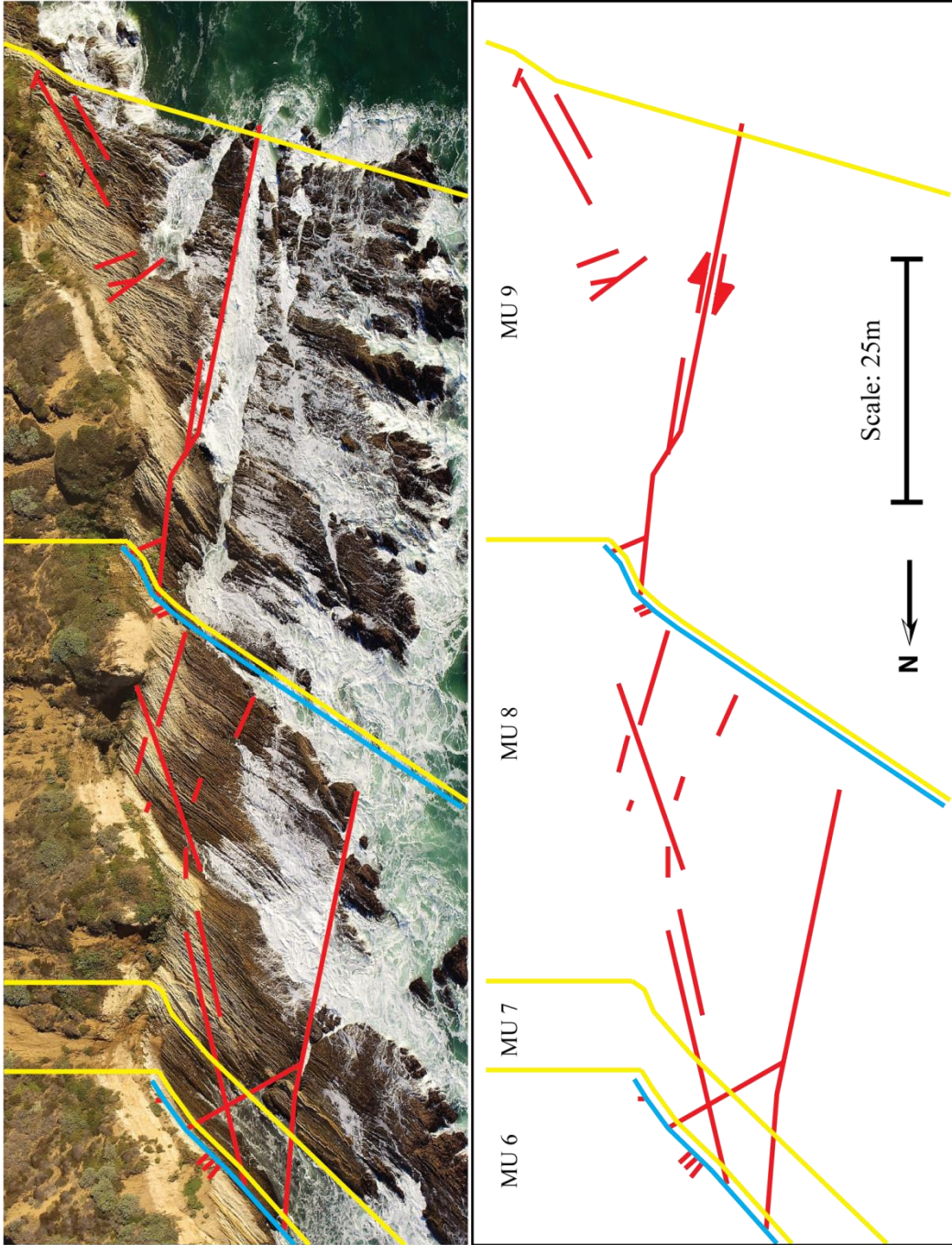


FIGURE 33. Fracture map of major unit 8–9. Red lines are fractures in orders 1–3, yellow lines are major unit boundaries, blue lines are tuff horizons, and red arrow indicate direction of offset.





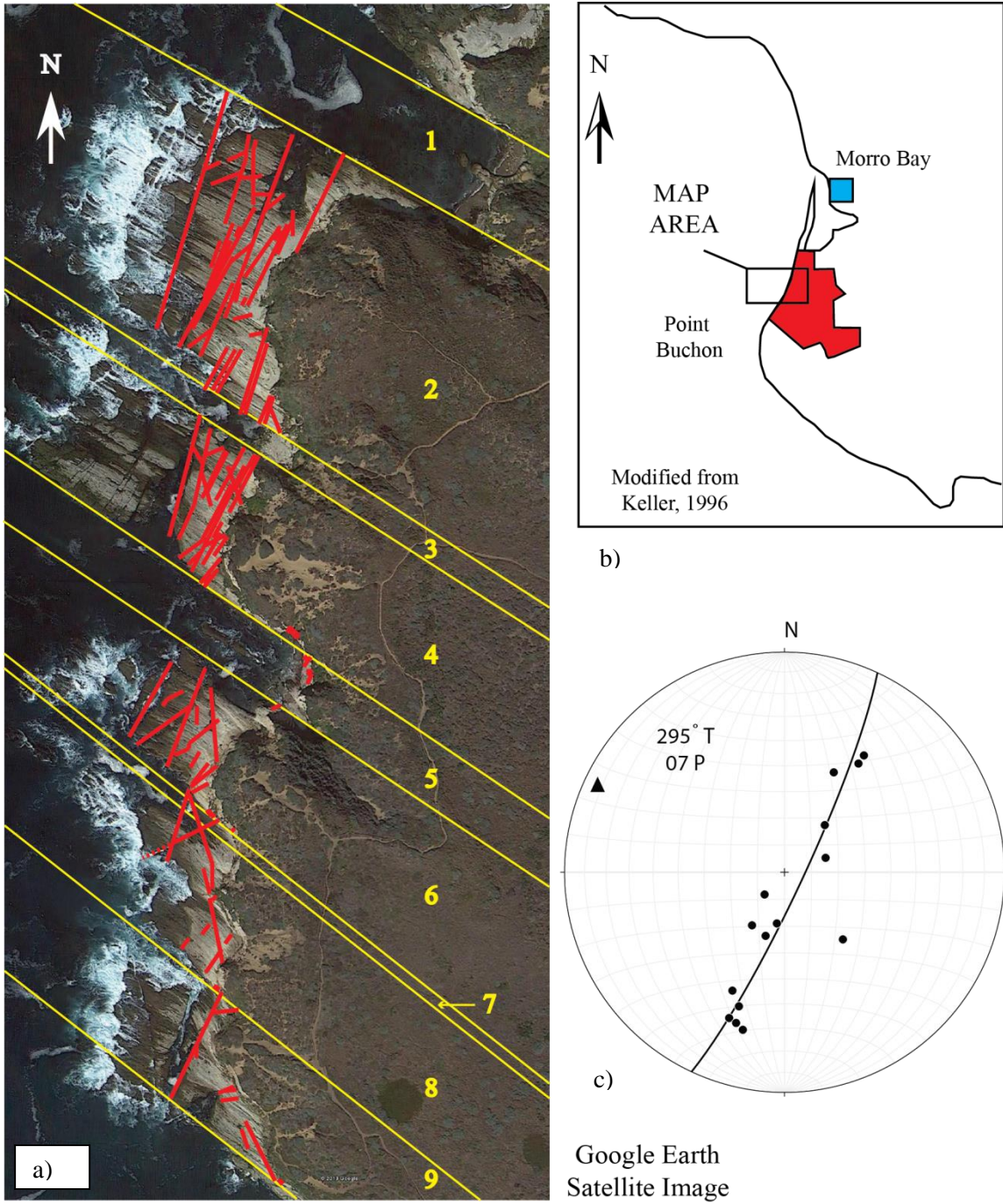


FIGURE 34. Composite fracture map of features in orders 1-3. a) Base map of mapped features in fracture orders 1–3 throughout the field area. Red lines are fractures and yellow lines are major unit boundaries. b) Location map of Montaña de Oro. c) Calculated regional fold axis.

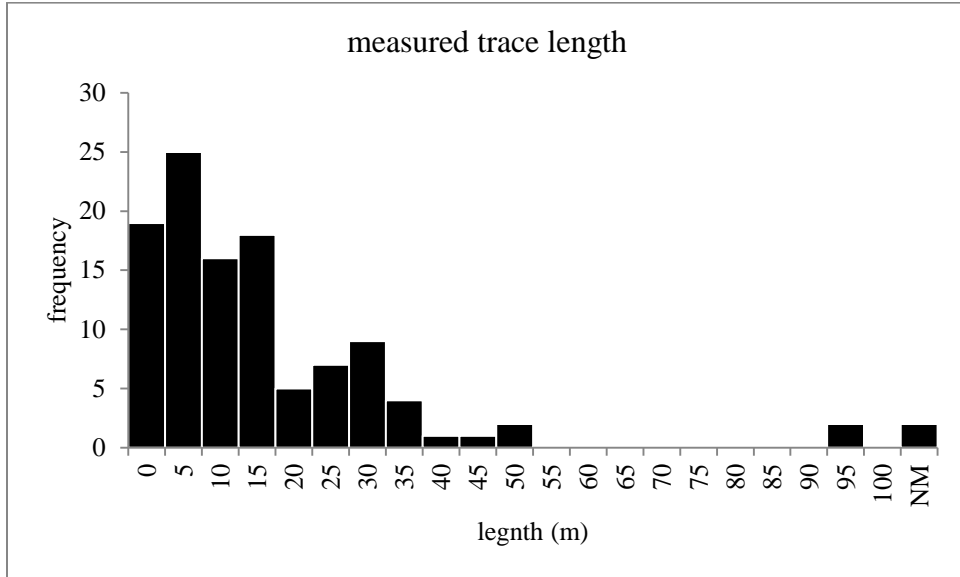


FIGURE 35. Histogram of measured trace length of fractures in orders 1–3.

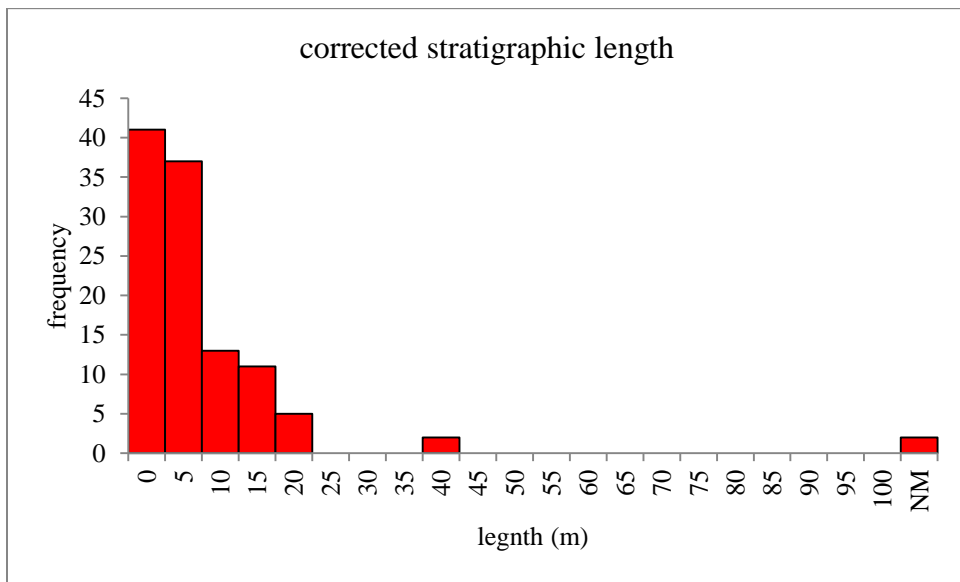


FIGURE 36. Histogram of corrected stratigraphic stratigraphic length of fractures in orders 1–3.

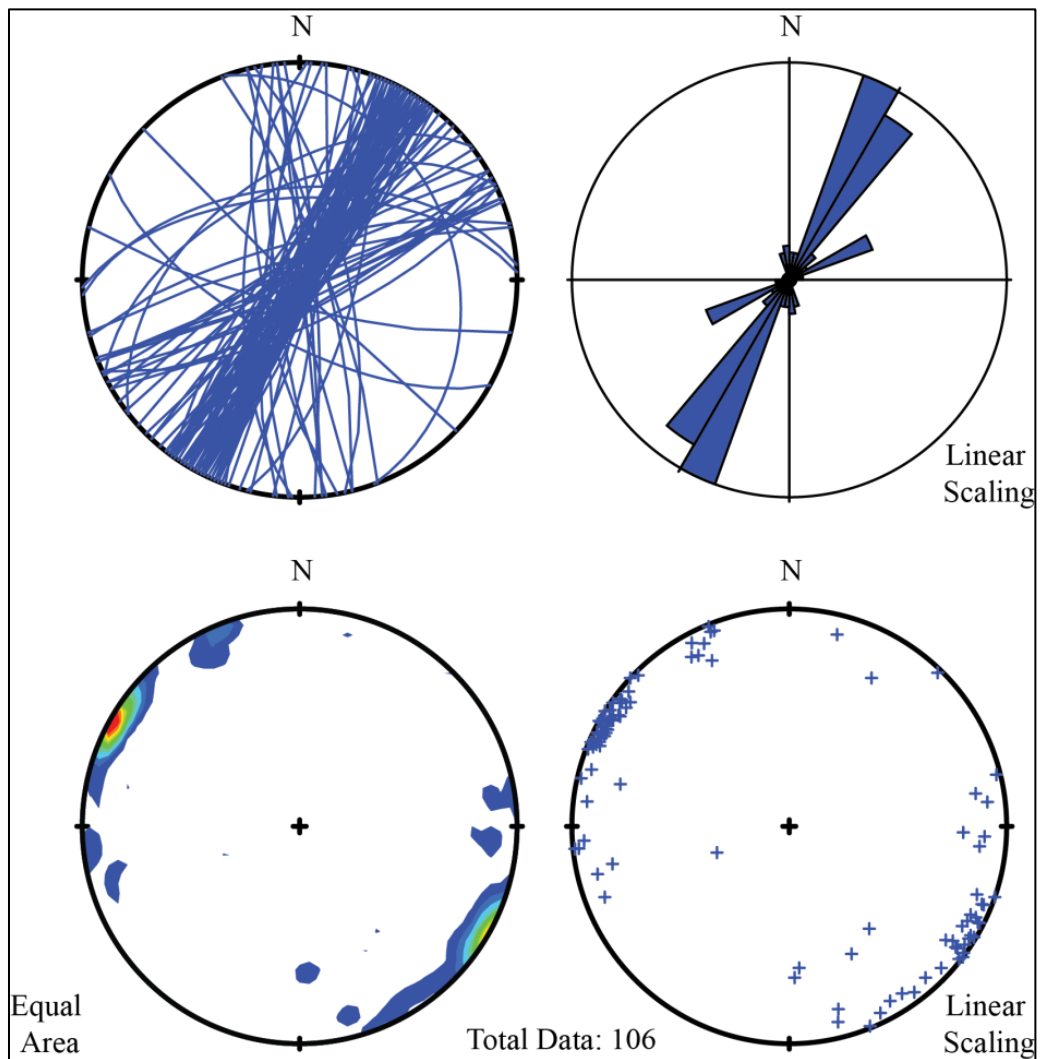
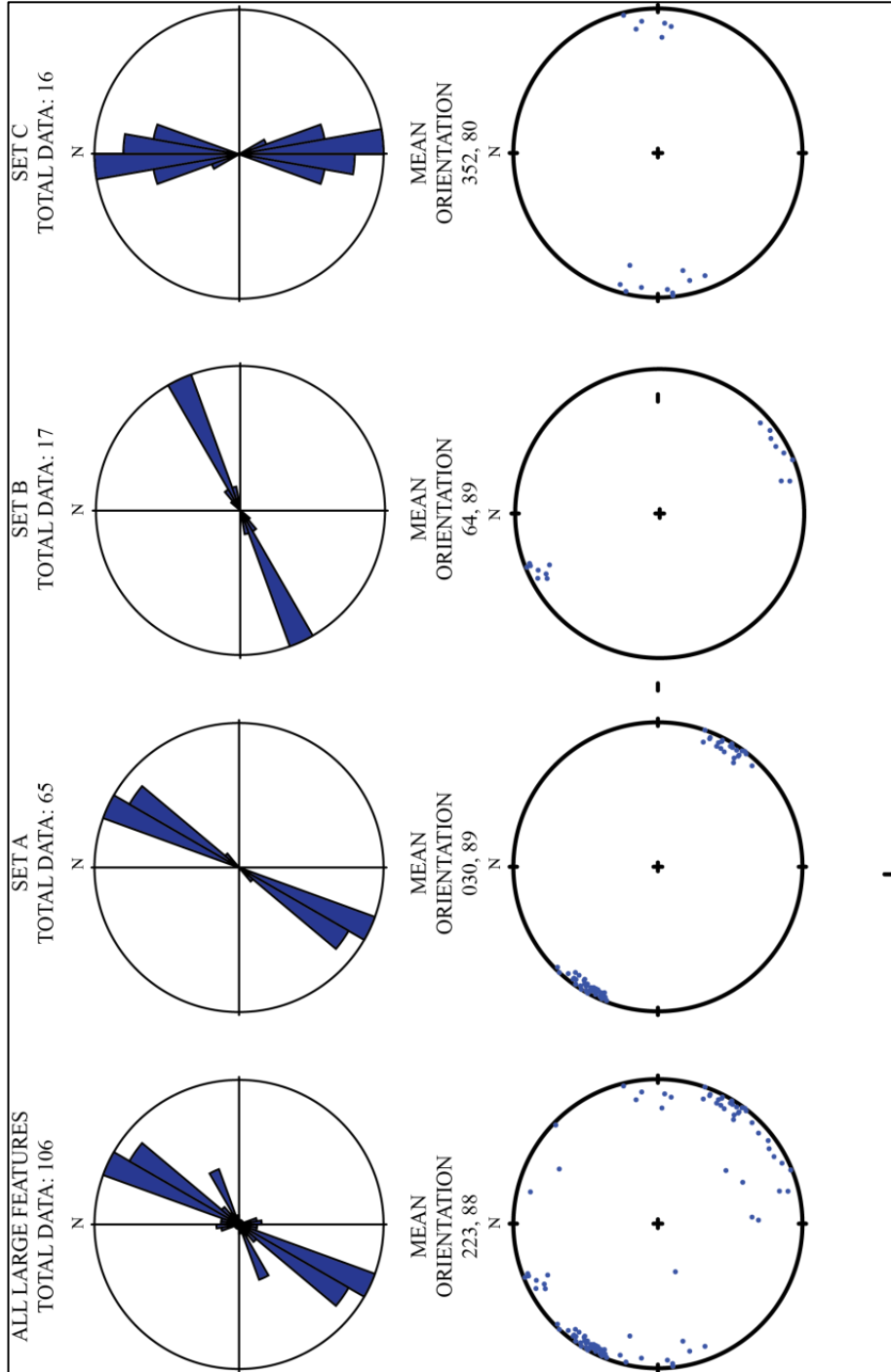


FIGURE 37: Orientation data of features belonging to fracture orders 1–3 for the entire field area. Clockwise from the upper left: great circles plotted on a stereonet; rose diagram of feature orientation; poles to fracture planes on a stereonet; contour plot of poles to fracture planes. Blue color is representative of features in fracture orders 1–3.

FIGURE 38. Fracture set analysis of features in fracture orders 1–3. There are 3 distinct fracture sets all oriented N/NE approximately  $30^\circ$  from each other.





For consistency, the fracture data for orders 1–3 are also compared between the upper (northern) and lower (southern) sections. Figure 39 shows the stereoplots of the upper and lower sections and illustrates the differences in orientation between the sections. Note the greater variability in fracture orientation of the lower section when compared to the upper section. The alpha-95 dispersion was calculated for the upper and lower sections to quantify the difference in fracture orientation between the sections. The upper section has an alpha-95 of  $7.3^\circ$  and the lower section has a value of  $17.3^\circ$ .

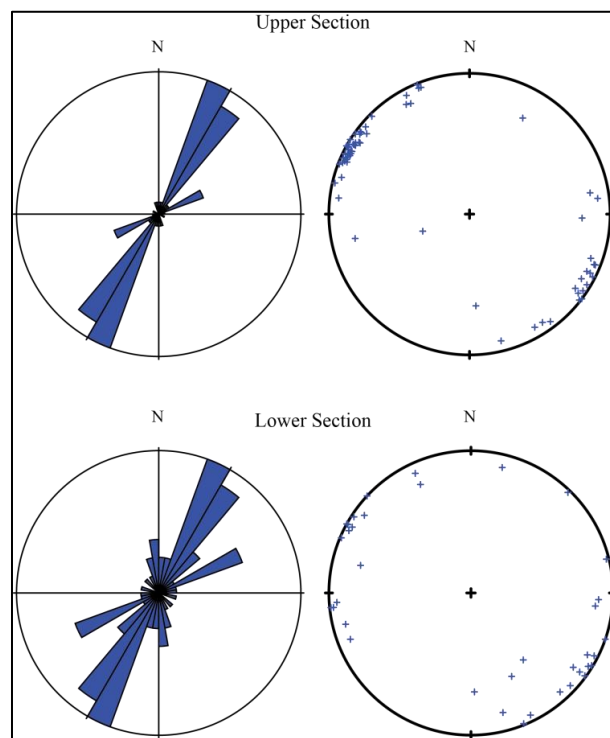


FIGURE 39. Linear rose diagram and poles to fracture planes of the upper (top) and lower (bottom) section. Note the lower section has a much greater variability in orientation and has more features in set B and C than the upper section.

There are 68 features in fracture orders 1–3 in the upper section that have orientation data. The lower section has 38. Both the lower and upper section have

fracture set A as the main fracture set, with lesser and variable number of features in fracture sets B and C. To address the frequency of fracture set A to the conjugate fracture set (sets B and C), the ratio of set A to B and C are calculated. The upper section has a ratio of 3.03, while the lower section is 1.35. These results show that set B and C are much more developed in the lower section relative to set A.

There are many more features mapped in the upper section due to greater area of exposed measurable terrace surface. In order to normalize these data and to assess the larger fracture density, another set of scanlines were measured parallel to the strike of bedding to intersect large features. Results of the large feature scanlines can be found in Appendix F. Large feature scanlines were not corrected for true spacing because there are multiple sets of fractures. Since there are multiple fracture sets, calculating the mean fracture orientation to correct for spacing would be inappropriate as it is not representative of each fracture set. The correction for true spacing along a single scanline is only valid when there is one fracture set being measured.

To be consistent in analysis, the scanlines were then compared between the upper and lower sections and the results are shown in Appendix G. The upper section has 2.5 features per 10 meters of scanline while the lower section has 1.9 features per 10 meters of scanline. The upper section has almost twice the cumulative length (both trace length and corrected stratigraphic) of features per scanline than the lower section and the average spacing is roughly two meters less than the lower section. This indicates that the upper section has a higher larger feature fracture density. However, many feature lengths are minimum lengths because upper and/or lower terminations could not be found; the cumulative length analysis must be noted as minimum length analysis.

The cumulative stratigraphic length of fractures per meters of scanline was calculated in an effort to normalize the fracture data due to the upper section having greater scanline lengths than the lower section (a product of better exposure). This was calculated by taking the cumulative measured trace length and the corrected stratigraphic length of each feature intersected by the scanline and then dividing that number by the scanline length. Figure 40 shows the normalized data by major unit scanline number, figure 41 shows the average cumulative length per meter scanline in each major unit, and figure 42 shows the data averaged between the upper (northern) and lower (southern) sections. The highest cumulative fracture length in the entire field area is unit 4, and the upper section has nearly twice the cumulative corrected fracture length of the lower section.

Figures 43 and 44 are histograms of cumulative measured trace length and corrected fracture length binned by orientation. The orientation data was corrected to quadrants 1 and 2 by subtracting  $180^\circ$  from any orientation that was between  $180^\circ$  and  $360^\circ$ . The data were then binned every 5 degrees. The features that were within each five degree bin had their stratigraphic lengths summed, resulting in cumulative corrected stratigraphic lengths per 5 degree bins. The data shows that the majority of features fall within  $20^\circ$ – $40^\circ$  (set A) and have the greatest combined length. The smaller clusters correspond to fracture sets B and C.

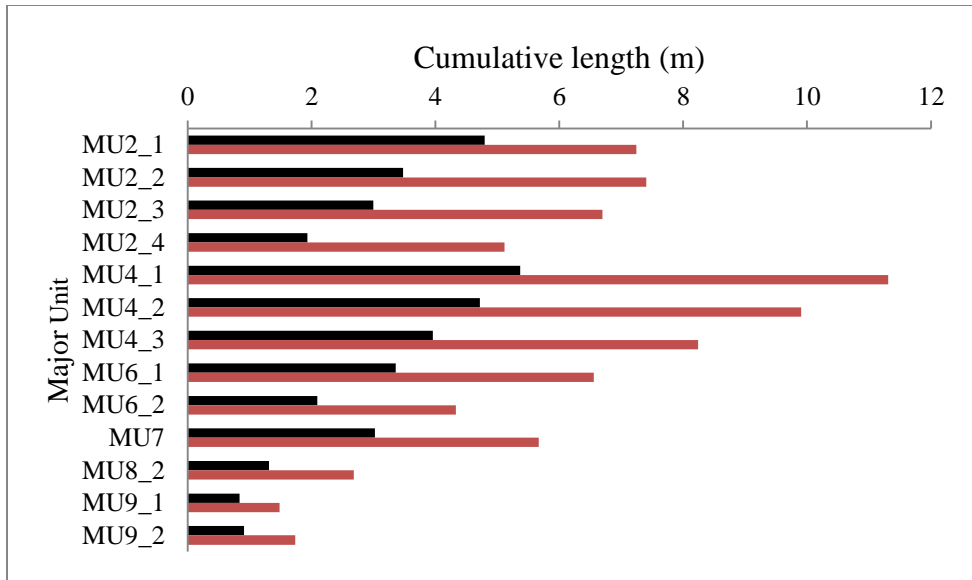


FIGURE 40. Bar plot illustrating the cumulative fracture length per meter scanline for each scanline. The data show major units 2, and 4 have the features with the highest cumulative fracture length both trace (red bars) and stratigraphic (black bars).

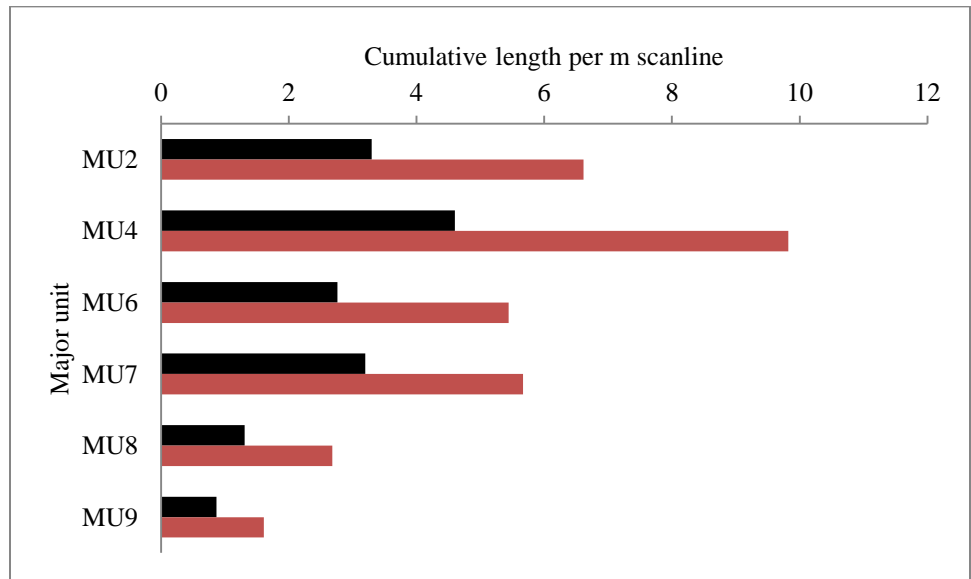


FIGURE 41. Bar plot showing the average cumulative corrected fracture length by major unit. Note major unit 4 has the highest cumulative fracture length in the entire field area. Trace length are red bars, black bars are corrected stratigraphic length.

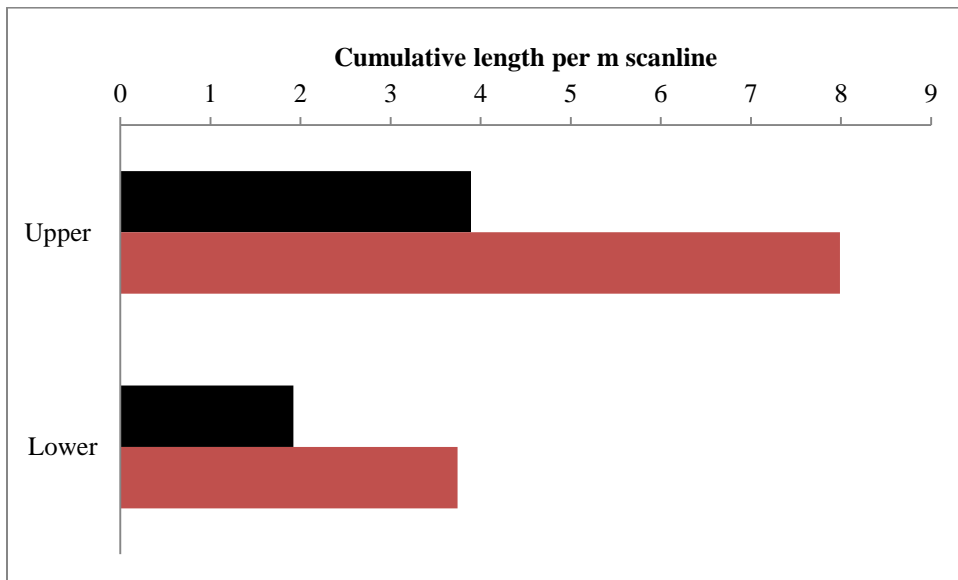


FIGURE 42. Bar plot showing the average cumulative corrected fracture length per m scanline in the upper and lower sections. Note that cumulative fracture length in the upper section is nearly twice the lower section for both trace (red bars) and corrected length (black bars).

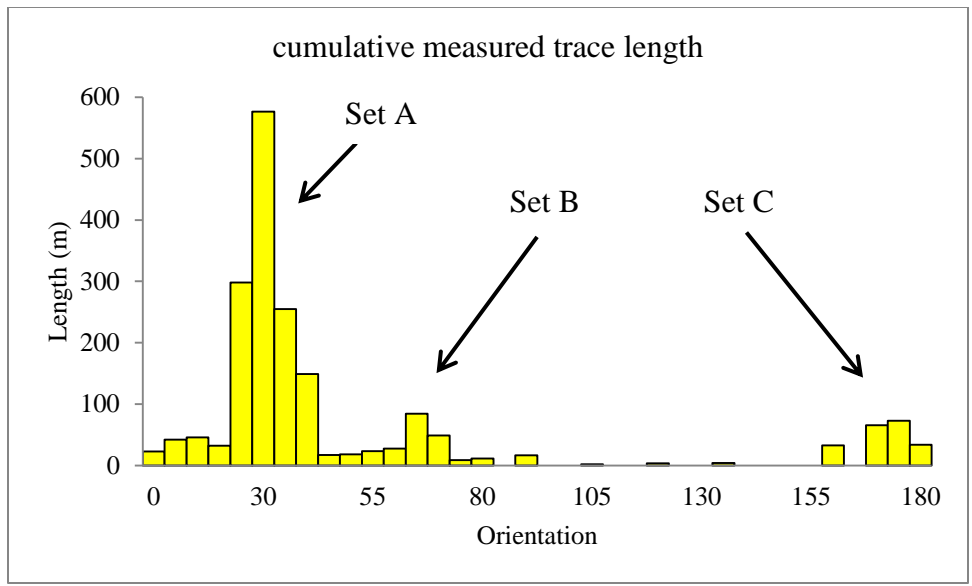


FIGURE 43. Graph of cumulative measured trace length per 5 degree orientation between 0 and 180°. Note the peaks around 30°, 70°, and 170°.

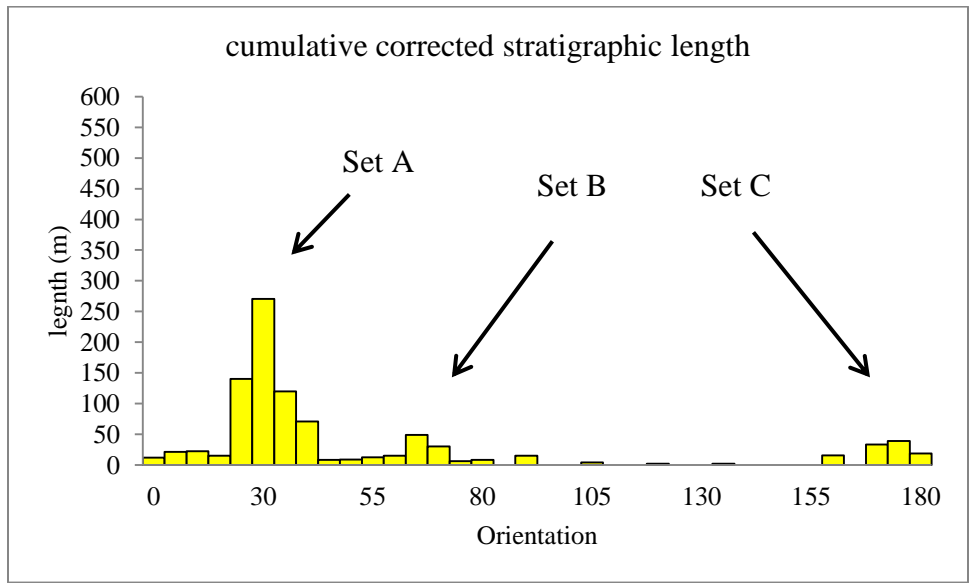


FIGURE 44. Graph of cumulative corrected stratigraphic length per 5 degree orientation between 0 and 180°. Note the peaks around 30°, 70°, and 170°.

The cumulative corrected length binned by orientation (every 10 degrees) was then broken down into the upper and lower sections (Figure 45). The histogram data show that the upper section has the highest cumulative stratigraphic length for set A, with the smaller peaks corresponding to sets B and C. The lower section also has the 3 fracture sets expressed, however their cumulative lengths are much smaller for A, B, and C. The difference in length between fracture set A and the conjugate set (set B and C) is much smaller in the lower section than it is in the upper section.

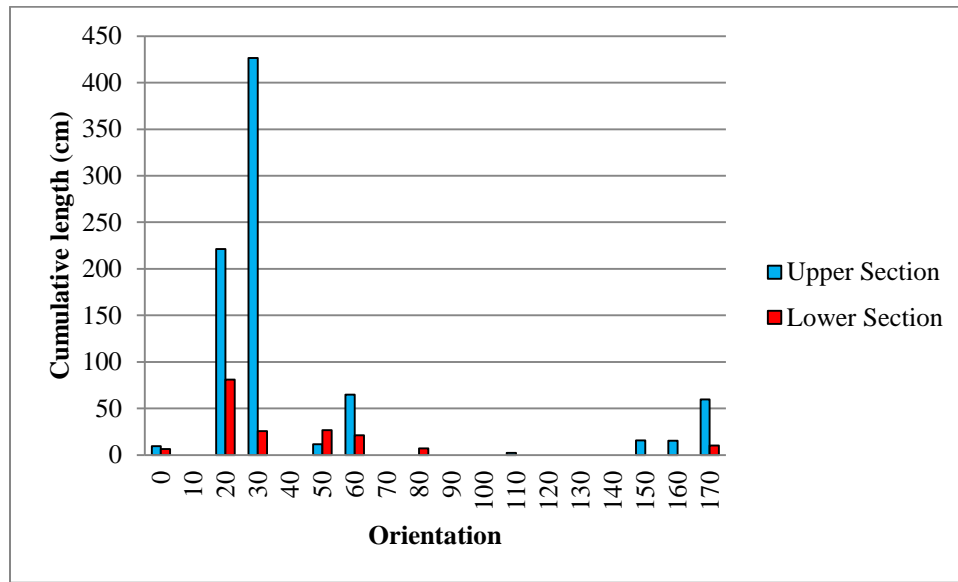


FIGURE 45. Graph of cumulative corrected stratigraphic length per 10 degree orientation between 0 and 180° in the upper section (blue) and lower section (red). Note the greatest length corresponds to set A in both sections and that orientations that correspond with sets B and C are much smaller.

The large features were also analyzed by frequency of fracture order. The data were separated by major unit and the number of features in each fracture order (1–3)



were then summed (Figure 46). Plotting the data this way shows the distribution of fractures orders throughout the field area. Fracture order 3 is the most abundant in all major units with the exception of unit 4, in which fracture order 2 is the modal order. In each unit, fracture order 1 is the least abundant.

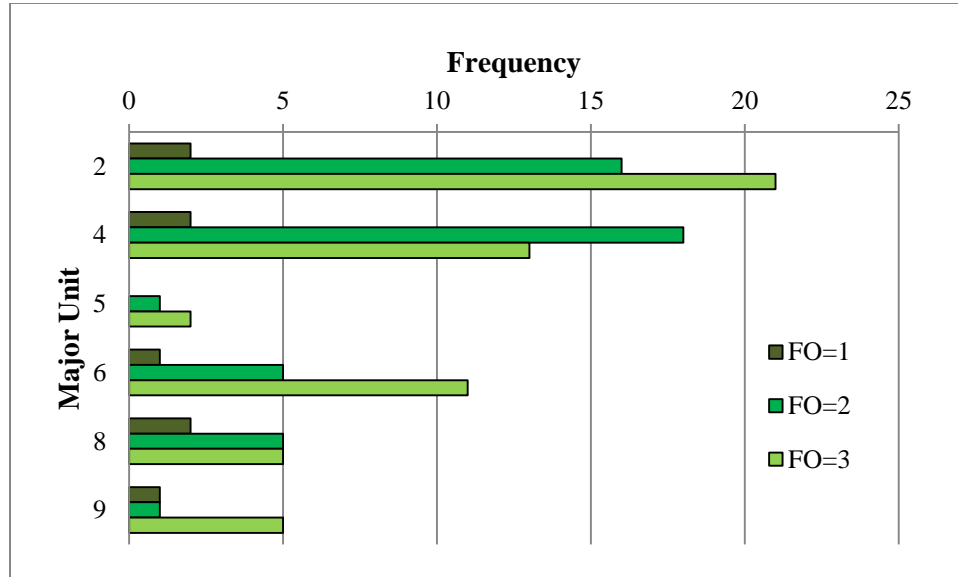


FIGURE 46: Bar plot showing the frequency of fracture orders 1–3 by mechanical unit. In all units, orders 2 and 3 are the majority and order 1 is the minority.

### Fracture Terminations-Orders 1–3

The final analysis of the features in fracture orders 1–3 focuses on the fracture terminations. Of the features mapped, their upper termination and lower terminations were separated into four categories: rock mass, set A, set B, set C, tuff, or unknown (unk). For example, if I was unable to map the feature termination (e.g., if it was covered or beneath the water line), then it would be classified as “unknown”. If a feature

terminated at a thick mudstone interface or mud-dominated unit or subunit, the termination would be designated as rock mass (Figure 47). Any feature that terminated at a tuff horizon was classified as “tuff.” If a feature terminated against another fracture, then it would be assigned that termination to the fracture set it terminated against. Fracture set A was the only fracture set that features terminated against (Figure 48). Fracture terminations for each feature are shown Appendix H, and the summary of fracture terminations are in Appendix I.

The total number (upper and lower) of fracture terminations were summed for each category and made a percent of the total fracture terminations (Figure 49). Of all upper and lower fracture terminations, 46 % of fractures terminated at or around a rock mass, 35% of fracture terminations are unknown, 12% of fractures terminated against set A, and 7 % of fractures terminated at a tuff horizon. This indicates that the major mechanical layer boundaries for all fractures are stratigraphic, and the minor mechanical layer boundaries are structural, abutting against a pre-existing fracture set (set A).

There are 4 features that have both their upper and lower termination against set A and 18 features that have their upper or lower termination against set A. There are 16 features in fracture sets B and C in the upper section with 12 features having at least one (upper or lower) termination against set A. In the upper section, 75% of features in set B and C terminate against set A fractures. Four of 14 features (28.5 %) in sets B and C in the lower section terminate against set A. There are 19 features in set B and C in the upper section that terminate against set A and 5 features in the lower section. There are 16 features in fracture sets B and C in the upper section with 14 features having at least one (upper or lower) termination against set A. In the upper section, 87% of features in

set B and C terminate against set A fractures. Four of 14 features (28.5 %) in sets B and C in the lower section terminate against set A. This difference in the number of terminations between the upper and lower sections is attributed to the upper section has many more set A features relative to the number of features in sets B and C.

Fracture terminations were also analyzed with stratigraphic depth (distance) in the field area. This was done by binning the data in 5 m intervals and summing the total number of upper and lower terminations in that interval (Figure 50). Plotting the data this way enables correlation of fracture termination horizons (mechanical layer boundaries) within the defined major and minor lithostratigraphic units.

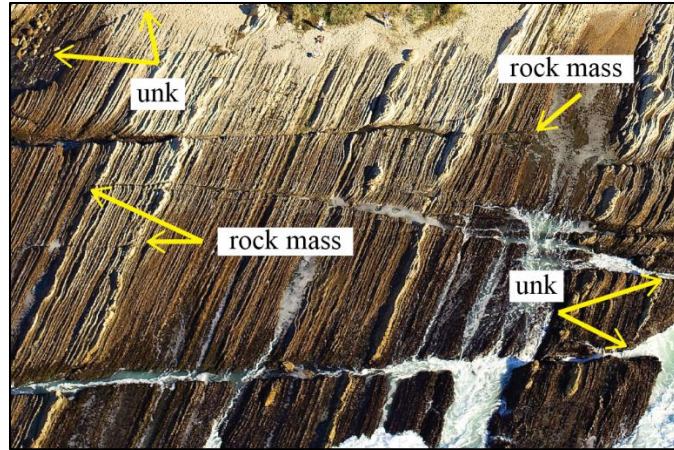


FIGURE 47. Field photograph illustrating “unknown” and “rock mass” fracture terminations in major unit 2.

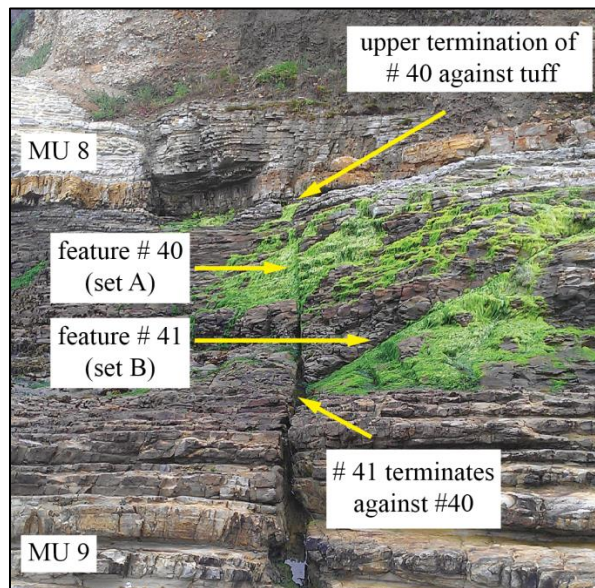


FIGURE 48. Field photograph of “set A” and “tuff” termination.

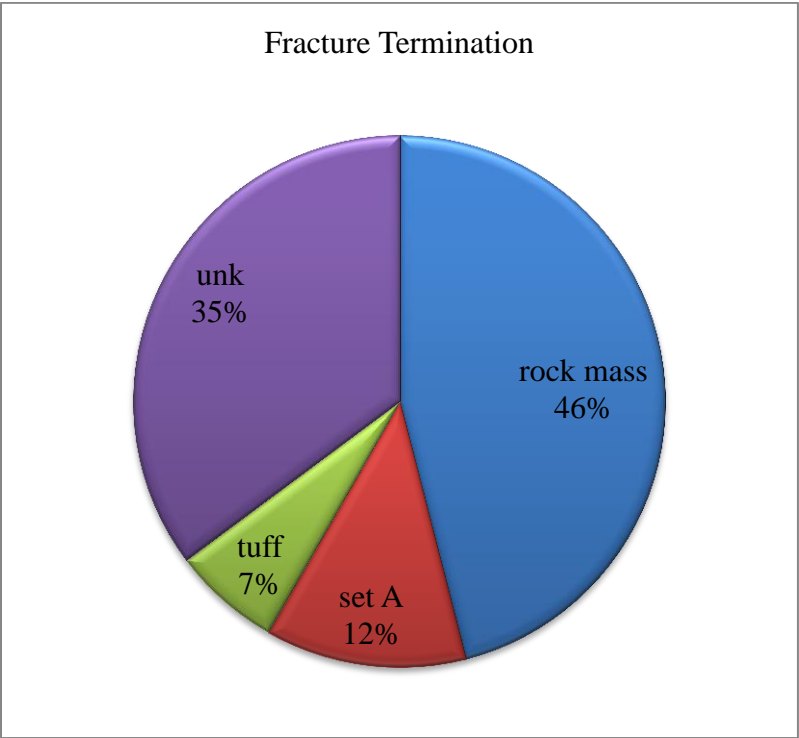


FIGURE 49. Pie chart of fracture termination horizons as a percent of the total number of terminations measured.

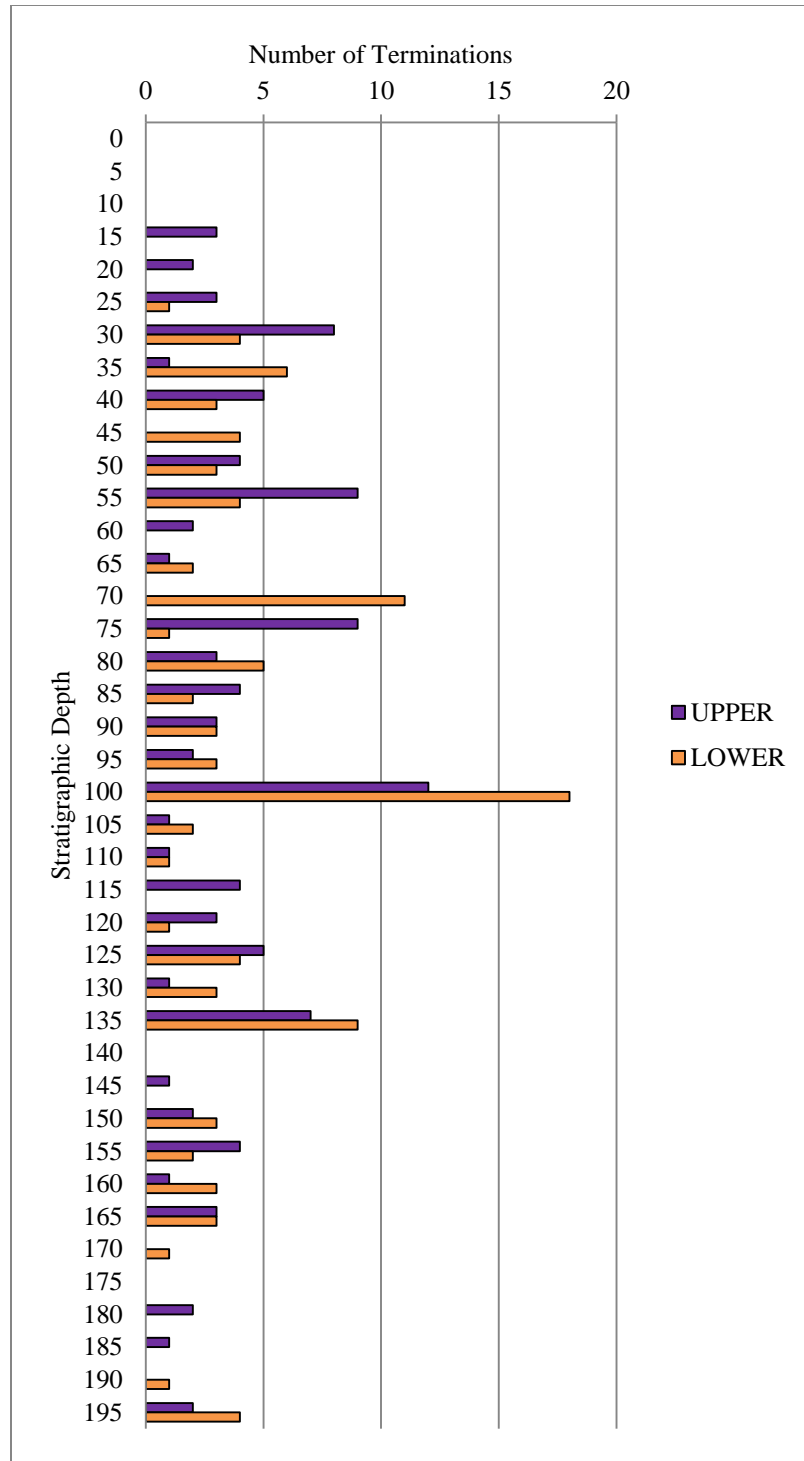


FIGURE 50. Histogram of number of fracture terminations plotted in stratigraphic depth. Note the area where there are high numbers of fracture terminations, such as, 30 m, 55m, 70m, 100m, and 135 m.

## CHAPTER 4

### DISCUSSION

The multiple types of structural and stratigraphic data collected at Montaña de Oro help to understand the complex relationship between stratigraphy and fracture development in the Monterey Formation at the reservoir scale. From the results presented in the previous chapter, it is evident that 4<sup>th</sup>-order fractures differ between lithologies and that all four orders of fractures differ in the northern (upper) section from the southern (lower) section. The following discussions will investigate various hypotheses for why the northern section has a greater degree of brittle deformation (fracturing) in comparison to the southern section (Table 1) and the defined mechanical stratigraphy (Figure 51).

TABLE 1. Summary of Data in the Northern and Southern Sections.

Data Type	Northern Section	Southern Section
FSR Porcelanite	1.1	0.57
FSR Mudstone	0.73	0.47
Normalized cumulative measured length (m)	1398 m	683 m
Normalized cumulative corrected length (m)	498 m	260 m
set A: B+C	3.06	1.35
Gamma-ray > baseline	11 m	32.5 m

List of abbreviations: FSR\_POR/MUD (fracture spacing ratio in porcelanite, mudstone); set A: B+C (ratio of fracture set A to fracture sets B and C); gamma ray > baseline (total meters of section with gamma-ray values higher than the 80 API baseline).

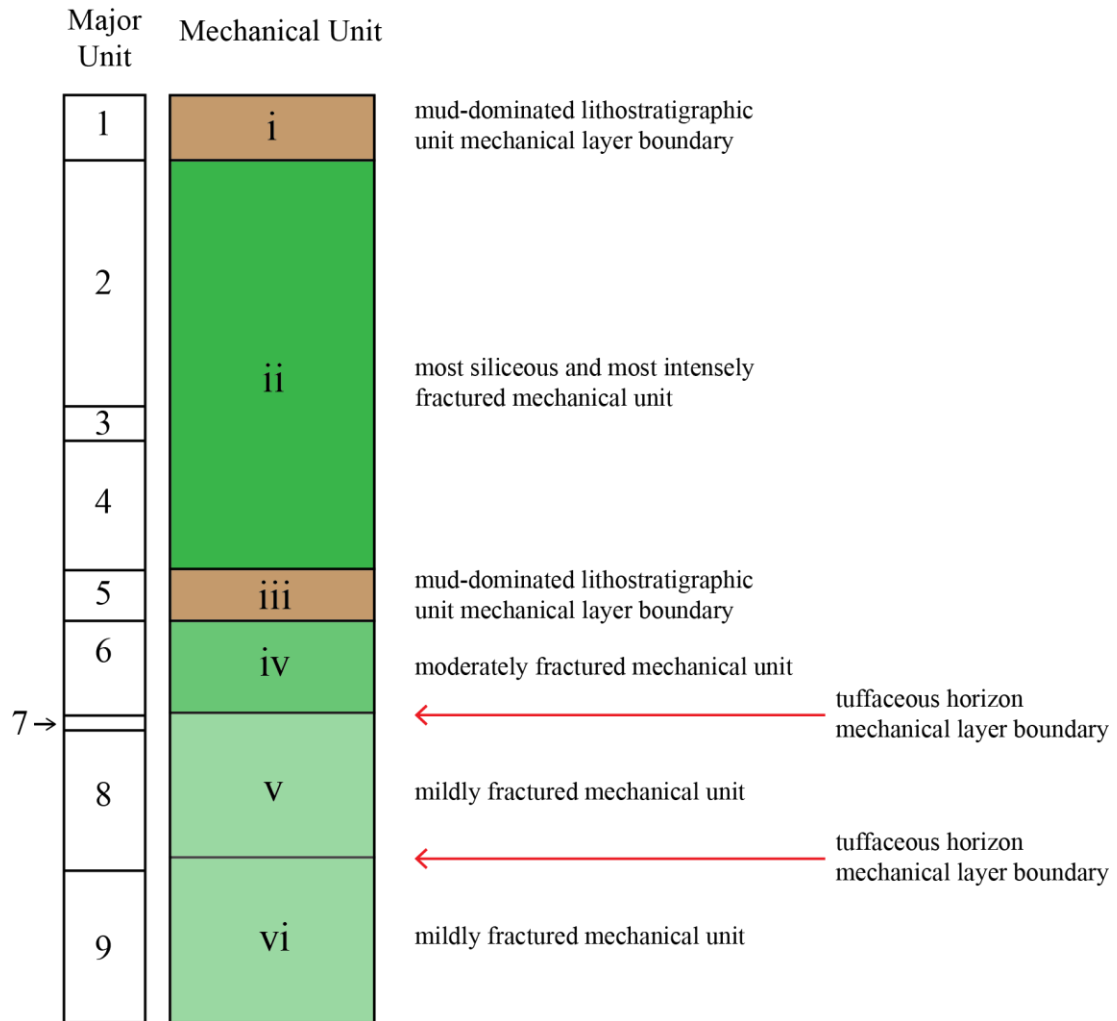


FIGURE 51. Mechanical stratigraphic column. There are 6 mechanical units (i-vi) defined by the fracture termination horizons and fracture intensity, which were delineated by the cumulative length plots, FSR data and fracture termination histogram.

### Effect of Lithology

The 4<sup>th</sup>-order fractures in porcelanite beds differ from those in mudstone by average fracture spacing, degree of variability in fracture spacing, and variability in orientation. The average mudstone one-dimensional fracture spacing as expressed by a FSR of 0.61, while the average porcelanite has a greater FSR of 0.79. These values



demonstrate that for a given bed thickness, mudstone beds will have less 4<sup>th</sup>-order fractures than porcelanite beds, which is consistent with previous studies (Gross et al., 1995).

Along a single scanline, 4<sup>th</sup>-order fractures in porcelanite have more consistent fracture spacing than those in mudstone, which is reflected in the standard deviation of the spacing measurements of 6.07 cm and 22.15 cm, respectively. The difference in standard deviation of the spacing measurements show that 4<sup>th</sup>-order fractures in mudstone are 4 times more broadly distributed from the mean fracture spacing than those in porcelanite. Mudstone beds also have a greater degree of variability in the orientation than does porcelanite. The difference in orientation between the lithologies is slight, but the alpha-95 of mudstone is 5, while the porcelanite is approximately 2, showing that the 4<sup>th</sup>-order fractures in mudstone beds have a greater variability in orientation than those in porcelanite beds.

#### Stratigraphy and Fracture Development

Identification of the 9 major lithostratigraphic units was based on the gross physical properties of the rocks that controlled resistance to erosion in the intervals. As described earlier, this chiefly reflects the relative amount of hard, siliceous lithologies (porcelanite, cherty porcelanite) compared to softer mudstones. However, resistance to erosion is also influenced by variations in bed thickness or the presence of dolostone beds and horizons. The spectral gamma-ray survey was used to quantitatively address the stratigraphy throughout the entire field area, both between and within major lithostratigraphic units.

Results from the gamma-ray survey show that the upper section has lesser amounts of gamma-ray-producing detrital clay and organic matter than the lower section. Applying the 80 API baseline to the total gamma-ray curve shows that the lower section has 30.25 m of section above the baseline, while the upper section has only 11 m of section above the baseline. Because the sections are of similar total thickness, these data indicate that the lower section has approximately three times the thickness of detritus/mud-dominated intervals than the upper section. Figure 21 shows the gamma-ray curves and it is evident by their character that there is not only overall higher values in the lower section, but also that the areas that are mudstone-dominated in the lower (southern) section are thicker than the mudstone-dominated intervals in the upper (northern) section.

Strata that have higher silica to detritus ratios will be more brittle than strata with lower silica to detritus ratios and more brittle strata will be more susceptible to jointing with applied strain (Gross et al., 1995). Therefore, it should be expected that the northern (upper) section will have a higher intensity of fracturing in comparison to the southern (lower) section. The 4<sup>th</sup>-order FSR scanline data at Montaña de Oro confirm this relationship by showing that the northern section average FSR is more than twice as high as the southern section (Table 1). The average FSR in porcelanite of the upper section is 1.15 and the average of the lower section is 0.55. This difference in 4<sup>th</sup>-order fracture intensity between the northern and southern sections is may be attributed to the higher amount of fine detritus relative to silica in the southern section by the gamma-ray data and field observations that indicate the northern section porcelanite beds are “chertier.”

Previous studies have shown that show fracture spacing is more or less proportional to bed thickness of the fractured layer (Helgeson and Aydin, 1991; Wu and Pollard, 1995; Gross et al., 1995; Bai and Pollard, 2000; Engelder and Gross, 1995) with fracture spacing ratios ranging from 0.1 to more than 10 in beds with consistent mechanical properties (Bai and Pollard, 2000). If a lithology is more brittle than another, it will likely have a higher fracture spacing ratio than less brittle lithology (Gross et al., 1995). However, the 4<sup>th</sup>-order fracture data collected at Montaña de Oro does not show such a linear relationship of median fracture spacing and bed thickness (Figure 24). The scatter seen in Figure 24 is likely due to highly variable compositions in porcelanite beds throughout the field area (suggesting that previous studies were based on datasets from more uniform lithologies), or increased strain in the northern section, or a combination of the two.

In addition to the gamma-ray quantification of the stratigraphy, bed-thickness data was measured throughout that field area. Using the bed-thickness data, an approximate porcelanite to mudstone ratio (porcelanite:mudstone) was calculated for each subunit to better constrain the relationship between FSR and relative amounts of porcelanite to mudstone. The average porcelanite bed thickness was divided by the average mudstone bed thickness to obtain porcelanite:mudstone ratio. This ratio attempts to relate the average bed thickness porcelanite and mudstone to FSR at the meter scale in order to test the influence of overall stratal stacking on one-dimensional fracture density. We hypothesize that a higher porcelanite:mudstone ratio will likely have a higher FSR, due to a lack of “strain buffering” of thinner or a lesser amount of mudstone beds within the subunit. To test this hypothesis, the FSR data were plotted with the corresponding

porcelanite:mudstone ratio calculated for that subunit (Figure 52). The data show a high degree of scatter, indicating that the FSR and porcelanite:mudstone do not have a linear relationship. However, because of the methods of calculation of porcelanite:mudstone (described above), it is likely that the ratio has some degree of inaccuracy. In order to reduce the amount of error in the porcelanite:mudstone ratio, a more detailed measured section would likely be necessary.

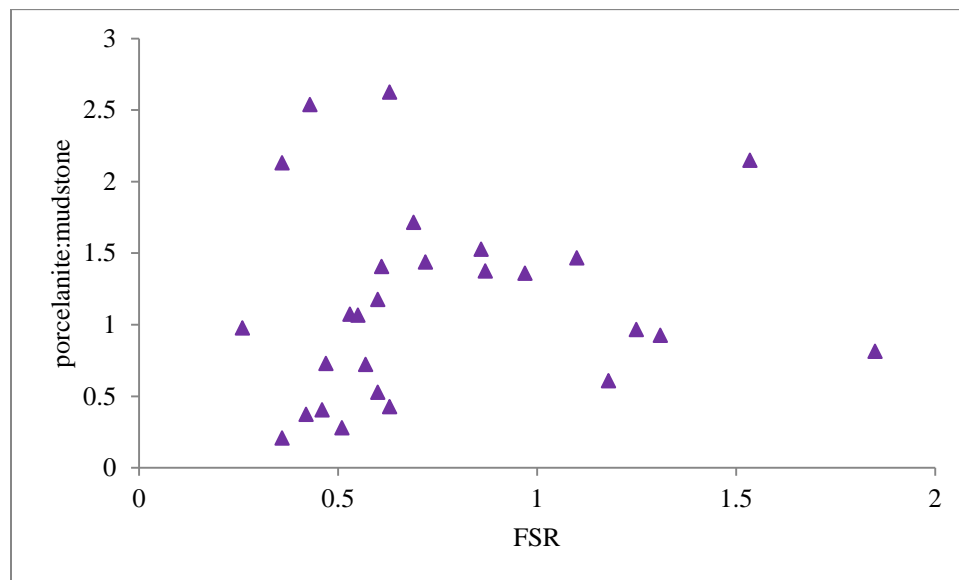


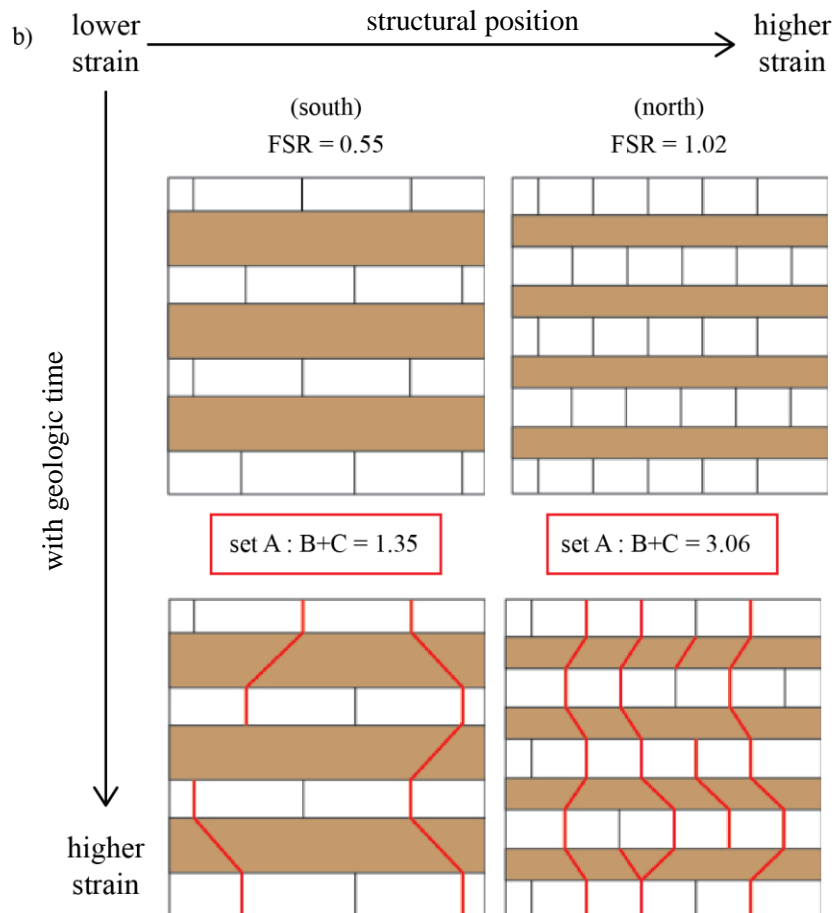
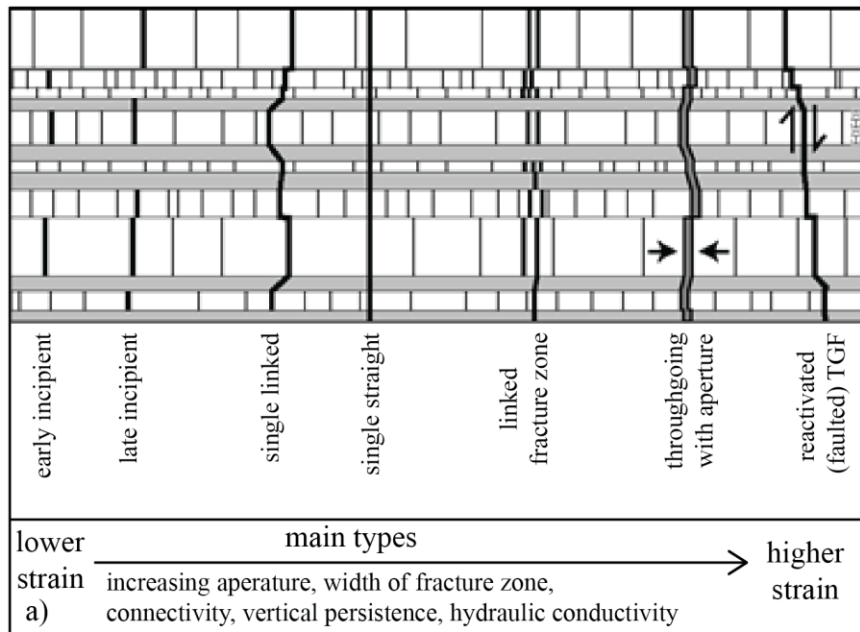
FIGURE 52. Scatter plot of porcelanite FSR and calculated average porcelanite:mudstone. Each triangle represents one scanline in the subunit.

The multilayer features that are parallel to the average orientation of the bed-confined fractures likely form through a continuum of development with applied strain through linkage of bed-confined fractures across bed-boundaries (Figure 53a; Gross and Eyal, 2007). Therefore, it should be expected that if one area initially had higher

amounts of 4<sup>th</sup>-order fractures than another, development of the larger fractures utilizing the pre-existing 4<sup>th</sup>-order fractures would be greater in the first. The FSR is a one-dimensional measurement of fracture intensity and the data shows the average FSR of the northern section (more siliceous) is nearly twice that of the southern section. It would then follow that the upper section should have a greater number of larger fractures that parallel the 4<sup>th</sup>-order fractures (set A). This is strongly supported by the data.

Overall, the upper section has more features (in all three fracture sets) mapped than the lower section due to greater amount of exposed area. To account for the discrepancy in the number of fractures (orders 1–3) in the northern and southern sections, the ratio of fracture set A to B and C were calculated for each section. The northern section has a ratio of 3.06 of set A to the conjugate fracture set, whereas the southern section has a ratio of 1.35. The data shows that the northern section has more than twice as large frequency of set A compared to the conjugate fracture set (sets B and C) than the southern section. It was likely easier for large features in set A to form in the northern section because of the higher intensity of parallel 4<sup>th</sup>-order fractures. To summarize, the more siliceous northern section (as reflected in gamma-ray) has a higher FSR in both porcelanite and mudstone, influencing the subsequent development of multilayer features (fracture orders 1–3) that parallel the 4<sup>th</sup>-order fracture orientation.

FIGURE 53. Composite fracture continuum diagram. a) Schematic of a “fracture continuum” with applied strain, or a hierarchy how fracture hierarchy in mechanically layered rocks may behave with continued applied strain (Gross and Eyal, 2007). Note the multilayer features are utilizing the pre-existing fractures as they begin to grow across bed boundaries. b) schematic representation applying the fracture continuum of Gross and Eyal (2007) to the development of 1) the increased 4<sup>th</sup>-order fracturing with strain, and 2) the linkage of multilayered features across bed boundaries with increasing strain in geologic time between the northern section vs. southern section.



## Fracture Development and Regional Tectonic Strain

According to Finkbeiner et al. (1997), the regional maximum horizontal stress in the southern-central California coastal areas is  $213^{\circ}$  (or  $33^{\circ}$  if plotted in the first quadrant) based on borehole breakout data from four offshore wells in the Santa Maria basin. Figure 54 shows a World Stress Map surrounding the field area. Data from the World Stress Map Project used to create the map can be found in Appendix J and has the average azimuth of the maximum horizontal stress ( $SH_{\max}$ ) to be  $41^{\circ}$ . The average orientation of the 4<sup>th</sup>-order fractures and larger order fractures belonging to set A is approximately  $30^{\circ}$ , making these fractures roughly parallel to the maximum horizontal stress. Fracture sets B and C are in the proper orientation for conjugate shear fractures related to the maximum horizontal stress (Figure 55).

Following the logic of the “fracture continuum” described above, the features that have right-lateral offset and are parallel to the bed-confined fractures likely represent the “oldest” (or most mature) of the larger features (Gross and Eyal, 1997). All 15 features in set A that have right-lateral offset belong to fracture orders 1 and 2, further supporting the concept that these features represent the more mature fractures in the fracture continuum. The presence of right-lateral offset is likely a manifestation of a slight clockwise rotation of the regional maximum horizontal stress. It is possible that locally, the field area has rotated counter-clockwise between two major right-lateral strike-slip faults, the Hosgri fault and the San Andreas fault, while the stress field has remained the same. However Sorlein et al. (1999) states there can only be clockwise rotation of this area due to the continual Pacific plate movement northward relative to the North American plate. Whether this rotation in regional maximum horizontal stress ( $SH_{\max}$ ) is



due to a rotation of the field area, or purely a rotation in the stress field, cannot be unequivocally determined at this time. However, this rotation in the stress field is likely syn-to-post formation of the main fracture set since there are relatively few features with offset in the same set.

Another explanation for right-lateral offset may be the presence of injectite (clastic dike) material in the fault. Of the 15 features with right-lateral offset, 6 of them contain injectite material. The injectite material is clastic, and often has deformation bands consistent with right-lateral movement. The material contains quartz and feldspars, is therefore allochthonous, and not cataclastic material from shear and grinding of opal-CT phase porcelanites or mudstones. It is possible that the weaker material between the fracture walls has a very low coefficient of friction, which allows the features to shear more easily than those features without injectite material.

Fracture sets B and C of the larger features are also related to regional tectonic shortening and  $SH_{max}$ , but their mechanism of formation is different from fracture set A. Fracture set A developed through the linkage of bed-confined fractures across bed boundaries; however, fracture set B and C did not have pre-existing fractures to utilize in their formation. These features often have a “halo” of 4<sup>th</sup>-order fractures that are parallel to them within a meter zone, but the fractures in orders 1–3 that belong to sets B and C do not utilize them. The orientation of fracture set B and C are roughly 60° apart and the bisector of the two sets is parallel to the regional tectonic strain and the strike of fracture set A. This angular relationship is consistent with Anderson Fault theory in which conjugate fracture/fault sets and/or normal faults develop 30° from the maximum stress direction (Davis and Reynolds, 1996).

Fracture sets B and C have 5 features with small normal offset (less than 10 cm) and fracture set A has 15 features with right-lateral offset with small to moderate offset of less than 1 m (Figure 56). The lack of significant offset for fractures in sets A and B indicates that these fractures are “incipient” shear faults related to tectonic shortening. They are incipient because they have little-to-no offset, however with continued applied strain these fractures would likely develop offset.

The regional fold axis ( $07^{\circ}\text{T}$ ,  $295^{\circ}\text{P}$ ) calculated from limited field mapping surrounding the field area is nearly perpendicular to the regional maximum horizontal stress. These angular relationships indicate that the calculated regional fold axis and the main orientation of all four orders of fractures formed in response to the regional tectonic shortening direction that is very close to current  $\text{SH}_{\text{max}}$ .

The timing of fracturing relative to regional folding is somewhat difficult to determine. The angular relationships show that the fractures and regional folding are related to regional horizontal stresses and tectonic shortening. However, nearly all fractures dip vertical to subvertical and when the data are rotated back to bedding horizontal, the fractures still are subvertical, adding no additional information to the timing of fracturing. Nonetheless, cross-cutting relationships can be used to establish relative timing. There are a total of 18 features in fracture sets B and C (out of 33) that terminate against fracture set A, that is 54 % of all conjugate fractures terminate against fracture set A. This relationship indicates that set A formed, at least in part, prior to formation of set B and C.

The intensity of all fracture orders (and fracture sets) is greatest in the northern section.

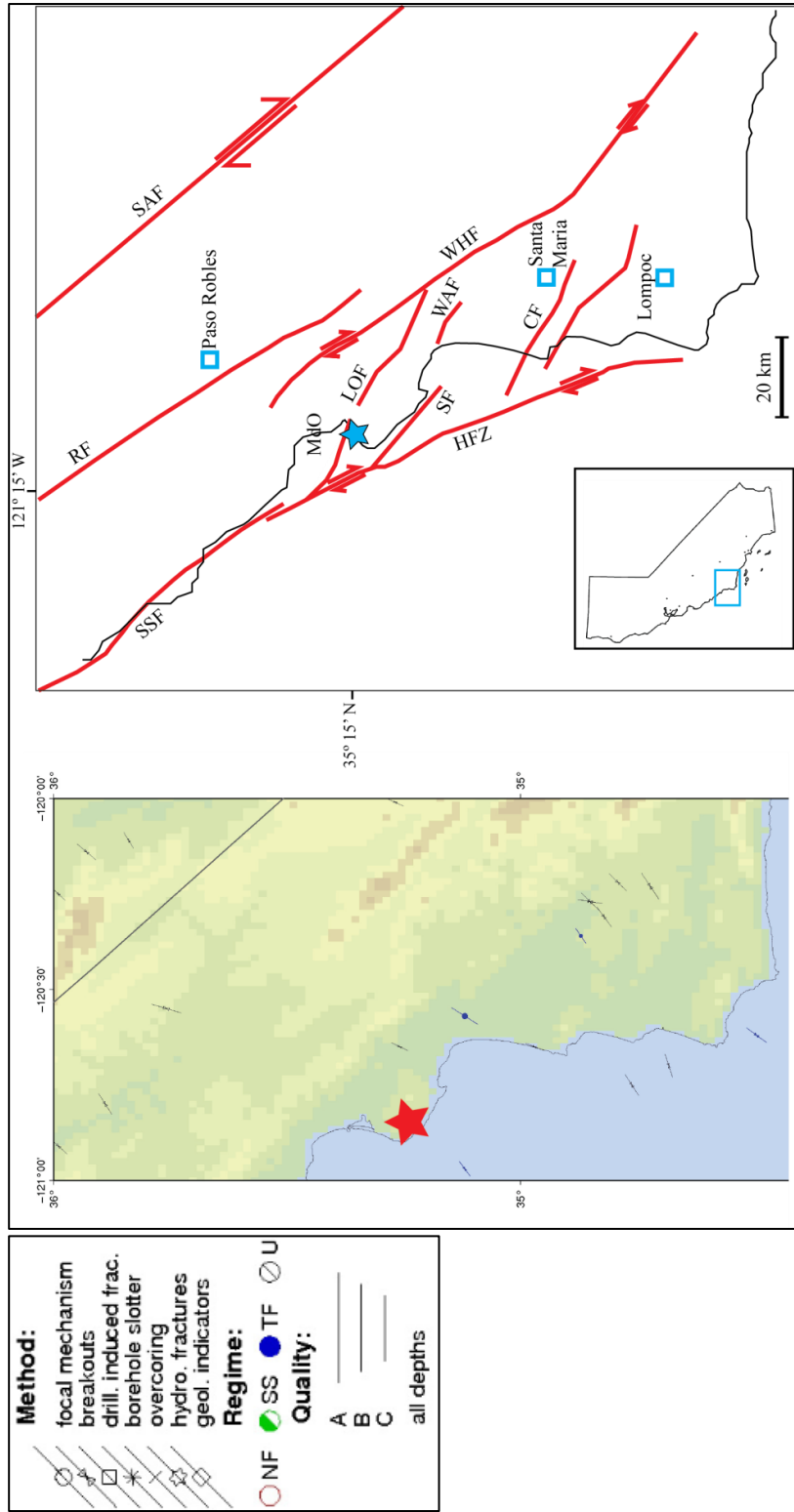


FIGURE 54. World Stress Map (World Stress Map Project, 2013) and regional fault map of the area surrounding the study site (abbreviations same as in Figure 6). The stars are the location of Montaña de Oro on each map.

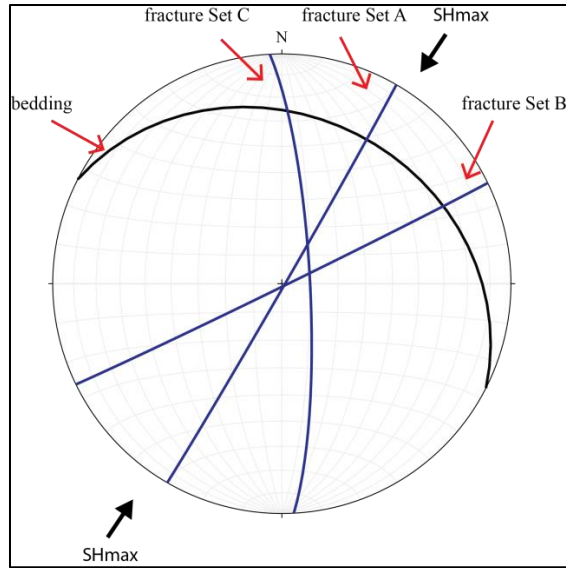


FIGURE 55. Stereoplot showing the angular relationships of average bedding (black great circles), fracture sets A, B, and C (blue great circles), and regional maximum horizontal stress (SHmax; black arrows).

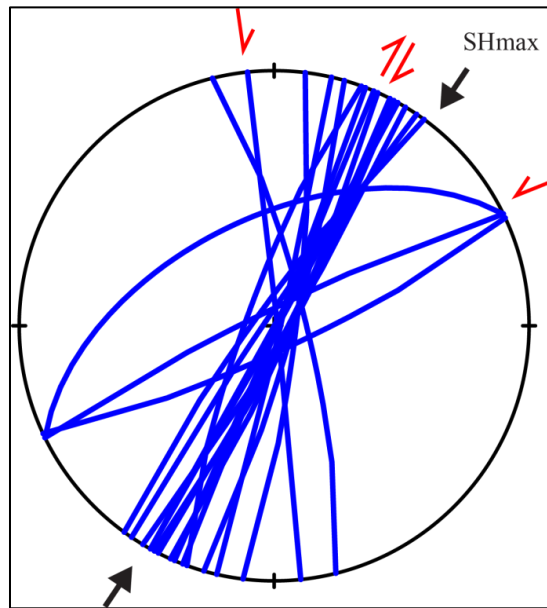


FIGURE 56. Stereoplot of the all features with offset relative to SHmax (regional maximum horizontal stress).

The significance of different lithologic compositions (as indicated by porcelanite:mudstone ratio and gamma-ray intensity) on the difference in fracture intensity between the northern (upper) and southern (lower) sections has been explored.

Another explanation for the greater intensity of brittle deformation in the northern section is that the area has experienced a greater amount of strain. The increased strain is attributed to structural position rather than increased silica content (increased brittleness) of the porcelanite. Just north of major unit 1 is the axis of the Pismo syncline, a major structural feature in the Pismo basin (Stanley and Surdam, 1984). The curvature of the syncline could impart strain on the rocks most proximal to the structure. In addition to the Pismo syncline, the Los Osos fault is also north of the field area (and north of the Pismo syncline). The Los Osos fault is a complex segmented fault with high-dip angles that converges with the Hosgri fault zone at its northern termination (Lettis et al., 1999). It is possible that the field area experienced increasing strain from south to north due to the presence of major structural features, such as the Pismo syncline and the Los Osos fault.

The other alternative to gradual increasing strain from south to north is that the northern section is under overall higher strain than the southern section, and major unit 5 acts as a strain “barrier,” or “buffer,” shielding the southern section (Figure 57). This is supported by the extreme multilayer fracturing present in major unit 4 reflected in the scanline measurements (Appendix F). Major unit 4 has the highest number of features (orders 1-3) intersected in each scanline, the highest normalized cumulative measured trace length, and the smallest spacing between large features. Figure 58 is a sketch of a multilayer “fracture swarm” in the lower section of unit 4 as it approaches a “strain

barrier” (unit 5). It is possible that the strain cannot cause an increase of length of multilayer fractures through unit 5, so the energy is partitioned to form new fractures, resulting in more 1-3 order fractures in unit 4.

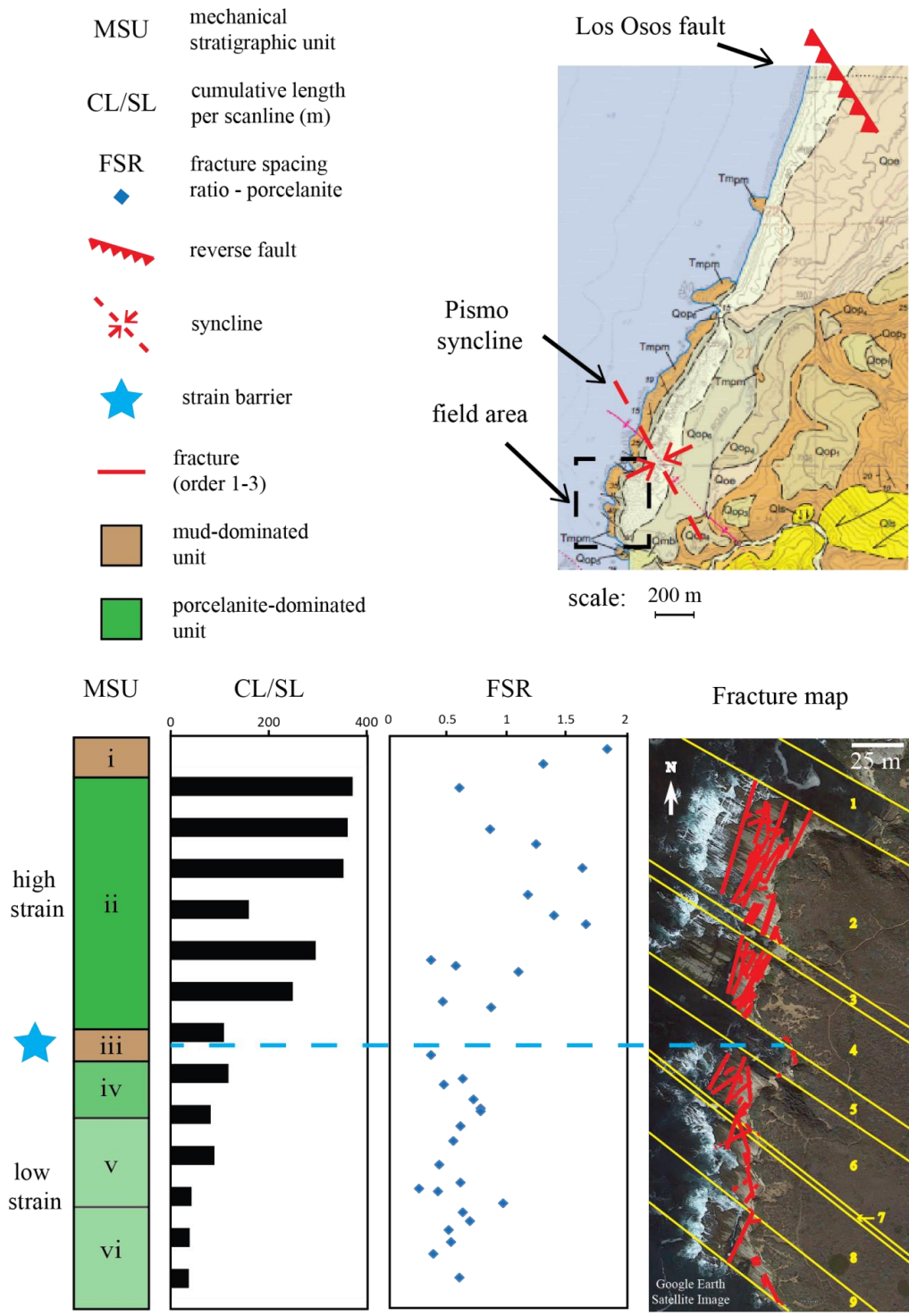


FIGURE 57. Composite diagram of fracture data in all four orders throughout the field area. All 4 orders of fracturing increases to the north due to increasing strain associated with the major structures of the Pismo syncline (accurate placement, with axis reflecting the regional fold axis calculated from this study) and Los Osos fault (rough placement).

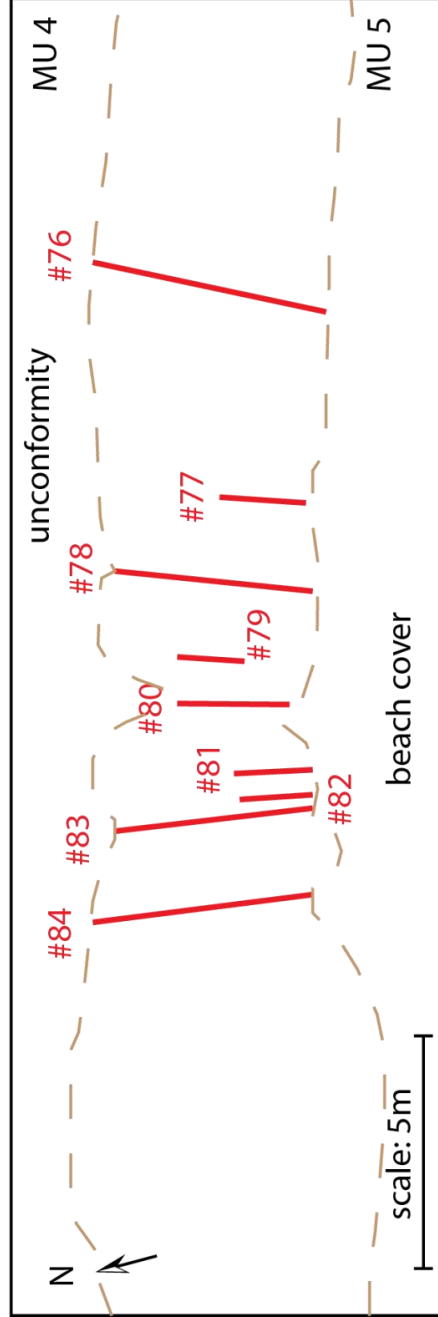
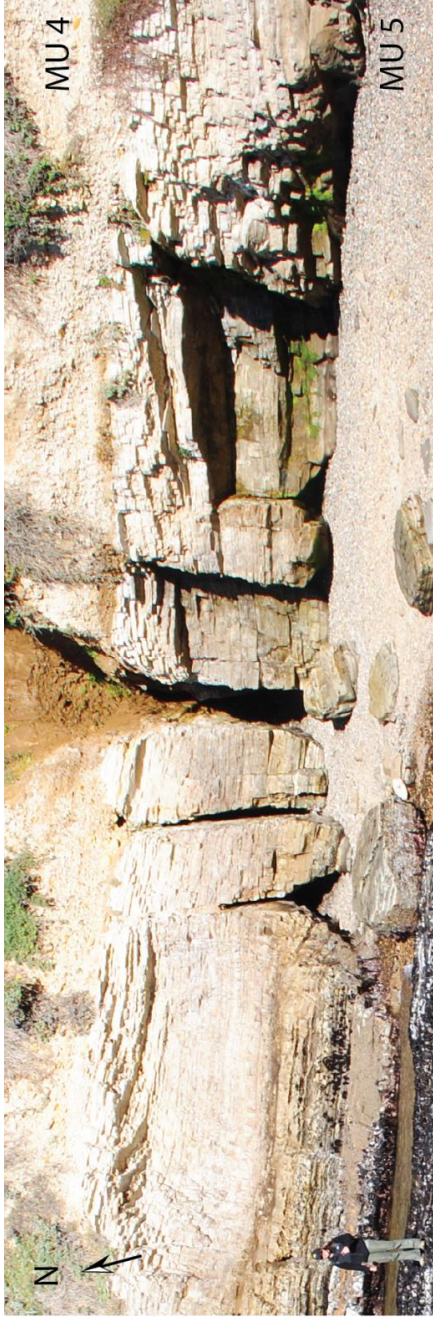


FIGURE 58. Sketch of multilayer fracture “swarm.” This swarm is located the lower section of major unit 4. Red lines are fractures (orders 1-3), dashed brown lines are unconformities, MU indicates major unit.



### Mechanical Layer Boundaries

Mechanical layer boundaries are surfaces, structural or stratigraphic, that a type of structural deformational style does not penetrate. Therefore, the mechanical units and mechanical layer boundaries cannot be delineated until all of the structural features are mapped. Since there are no major faults or folds within the field area, the only type of structural mechanical layer boundary is that formed by fracture set A to fracture sets B and C. Therefore, fracture set A inhibits the lengths of features in fracture set B and C (Figure 48). The stratigraphic mechanical layer boundaries are mudstone-dominated lithostratigraphic units and tuff horizons (Figure 51).

There are multiple horizons where many features terminate that correspond with higher excursions in the gamma-ray curve that lie within mudstone-dominated lithostratigraphic units, such as at depths around 70 m, 100 m, 110 m, and 130 m. However, there are also horizons where many fractures terminate that do not correspond to intervals higher gamma-ray values, such as depths around 30 m, 50 m and 125 m. These horizons are associated with erosional surfaces in which the fracture terminations that cannot be traced past a bed or surface too thin to be resolved by GR.

There are many thick mudstone beds ranging from 40-70 cm that do not act as mechanical layer boundaries in the field area, while others of the same thickness or greater do act as mechanical layer boundaries. The difference between these mechanical behaviors is likely due to variations in composition (e.g., clay amount or mineralogy) and texture, but this factor was not resolved due to limitations on sampling in the state park. From field examination alone, it is difficult to predict which mudstone beds will act as

mechanical layer boundaries to fracture propagation. Underwood et al. (2003) calculated that only 63% of mud horizons interbedded within the Silurian Dolomite, Wisconsin, acted as mechanical layer boundaries and that attempting correlate mechanical interfaces with stratigraphic layering yields a range of error from 13 to 33%.

The higher excursions in gamma-ray values correspond to zones that are more detrital-clay-rich or tuffaceous horizons, either of which can act as a mechanical layer boundary to fractures in more brittle strata due the mechanical contrast between the lithologies. Field maps show that tuff horizons are the most efficient single stratigraphic horizon that function as mechanical layer boundaries and range from 1–3 cm thick. All features that approach the tuff horizon at the bottom of major unit 6 and the bottom of major unit 8 terminate at the boundary. A 3-cm thick tuff bed near the top of major unit 5 terminates large feature 72; however, there are at least five additional features that may terminate at that same horizon, but are inaccessible for close inspection in the algae-covered intertidal zone.

Field observations show that in addition to tuff horizons acting as mechanical layer boundaries, they are also associated with zones of intense fracturing (Figure 59). A larger fracture that cannot propagate vertically through the tuff horizon distributes its energy laterally, creating a zone of intense fracturing. The intense fracturing around the tuff horizons could potentially be more effective in creating storage volume as fracture porosity, and may correspond to zones of higher production of fluids in the subsurface.

The tuff horizons may play a significant role in reservoir compartmentalization of fracture networks and act as mechanical layer boundaries to natural fracture propagation in many instances. It is possible that these tuff layers could also terminate induced

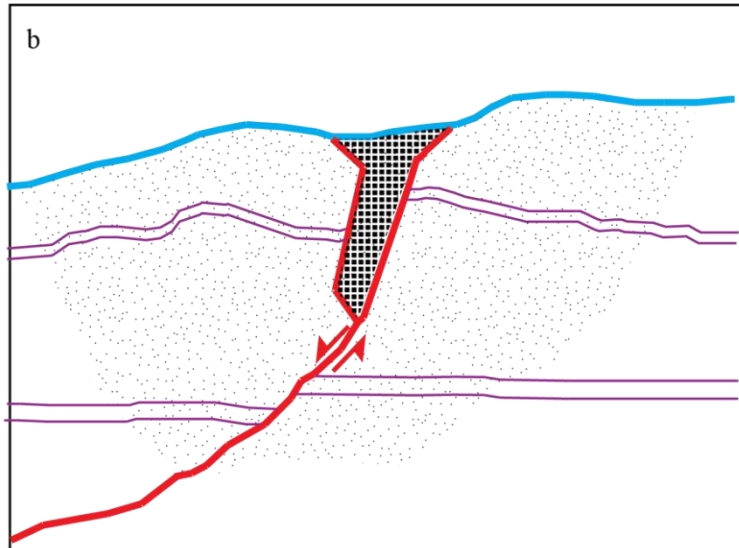
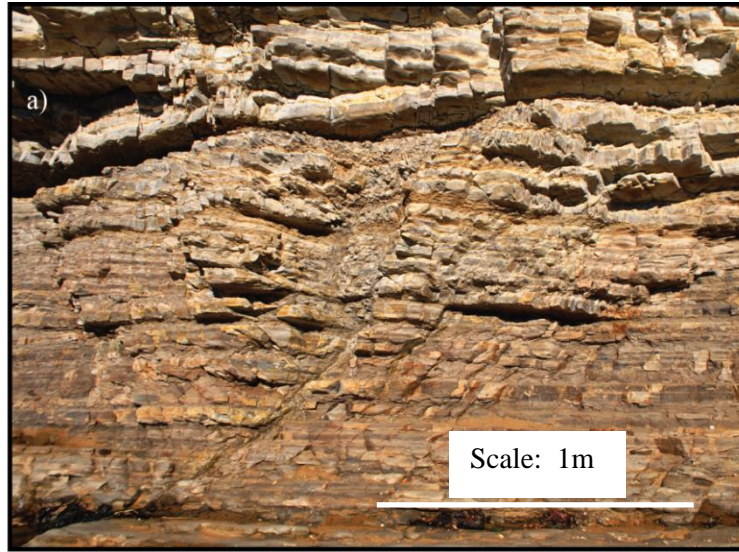
hydraulic fractures during well-stimulation. However, the rate of tectonic strain over millions of years is much, much less than the strain rate occurring during induced hydraulic fracturing, so the contrast that is geologically significant may not be as important when exposed to very short periods of high strain. Nonetheless, tuff horizons are significant mechanical interfaces and should be taken into consideration in fracture characterization (natural or induced).

As a single stratigraphic horizon, tuff is much more efficient than mudstone in terminating fractures in orders 1–3. However, the gamma-ray data suggests that areas that are mud-dominated with a minimum thickness of nine meters are also effective mechanical layer boundaries, such as units three and five. These boundaries form a more diffuse zone of fracture termination rather than a discrete interface, such as a tuff horizon or pre-existing fracture or fault. Unit seven and 8B are 7 meters or less in thickness and fractures in orders 1–3 pass directly through them. Figure 57 is a composite diagram showing fracture termination horizons compared to the defined major lithostratigraphic units, gamma-ray, and defined mechanical units.

There also seems to be a critical thickness for a single mudstone horizon to act as a mechanical layer boundary as suggested by Rijken and Cooke (2001). There are thick mudstone beds (approximately one-half meter) with phosphatic basal pebble conglomerates in major units two, five, and six that do not terminate high order features. However, there are a mudstone beds in 3 and 5B that are over a meter thick and may act as a discrete mechanical layer boundary. Unfortunately, it is difficult to conclusively determine its effect due to access, but projecting along strike of the mudstone, it seems that fractures in major units four and six do not cross this horizon.

The most important mechanical unit corresponds to major lithostratigraphic unit 5. No fractures in orders 1–3 in unit 6 can be traced northward of unit 5, and no fracture in orders 1–3 in unit 4 can be traced southward of unit 5. Major unit 5 is the thickest mudstone-dominated lithostratigraphic unit, with thick-bedded mudstones and two tuff horizons. This unit separates and compartmentalizes the fracture networks in the northern section from the southern section. In addition, major unit 4 has the highest frequency of fractures in orders 1–3. This intense brittle deformation could be due to a potential “buffering effect” of major unit 5. It is possible that the thick, mudstone-dominated major unit 5 is accommodating strain from the northern section and in effect shielding the southern section from the applied strain.

In the Monterey Formation, at the very basic level, mechanical properties of rocks vary according to the amount of silica and diagenetic grade (Gross et al., 1995). Strata with higher amounts of silica will be more brittle and therefore susceptible to fracturing. The higher intensity of 4<sup>th</sup>-order fractures will allow greater linkage along pre-existing fractures to form higher order fractures. The amount of higher order fractures paralleling the 4<sup>th</sup>-order fractures may inhibit the number and length of higher order fractures belonging to different sets (Figure 21). It is the primary stratigraphy that can dictate the intensity of bed-confined fracturing, which subsequently affects the propagation and development of larger fractures. Structural position, such as the proximity to the Los Osos fault and the Pismo syncline, cannot be ignored when discussing explanations for increase fracture intensity. Increasing strain and silica content northward is likely responsible for the more intense brittle deformation in the northern section. Figure 60 is a conceptual model of how the fracture system at Montaña de Oro formed.



LEGEND




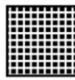


	Fault Plane		Sense of Offset
	Mechanical Layer Boundary		Fault Core
	Stratigraphic Unit		Fault Damage Zone

FIGURE 59. Field photograph and sketch of fracture damage zone associate with tuff horizons. This tuff functions as a mechanical layer boundary near the base of 6C.

FIGURE 60. Composite diagram of fracture data relative to major lithostratigraphic and mechanical units. illustrating (from left to right) the total gamma-ray, FSR (fracture spacing ratio), stratigraphic location of tuff horizons, fracture termination histogram (upper in purple, lower in orange) major units, and mechanical units.

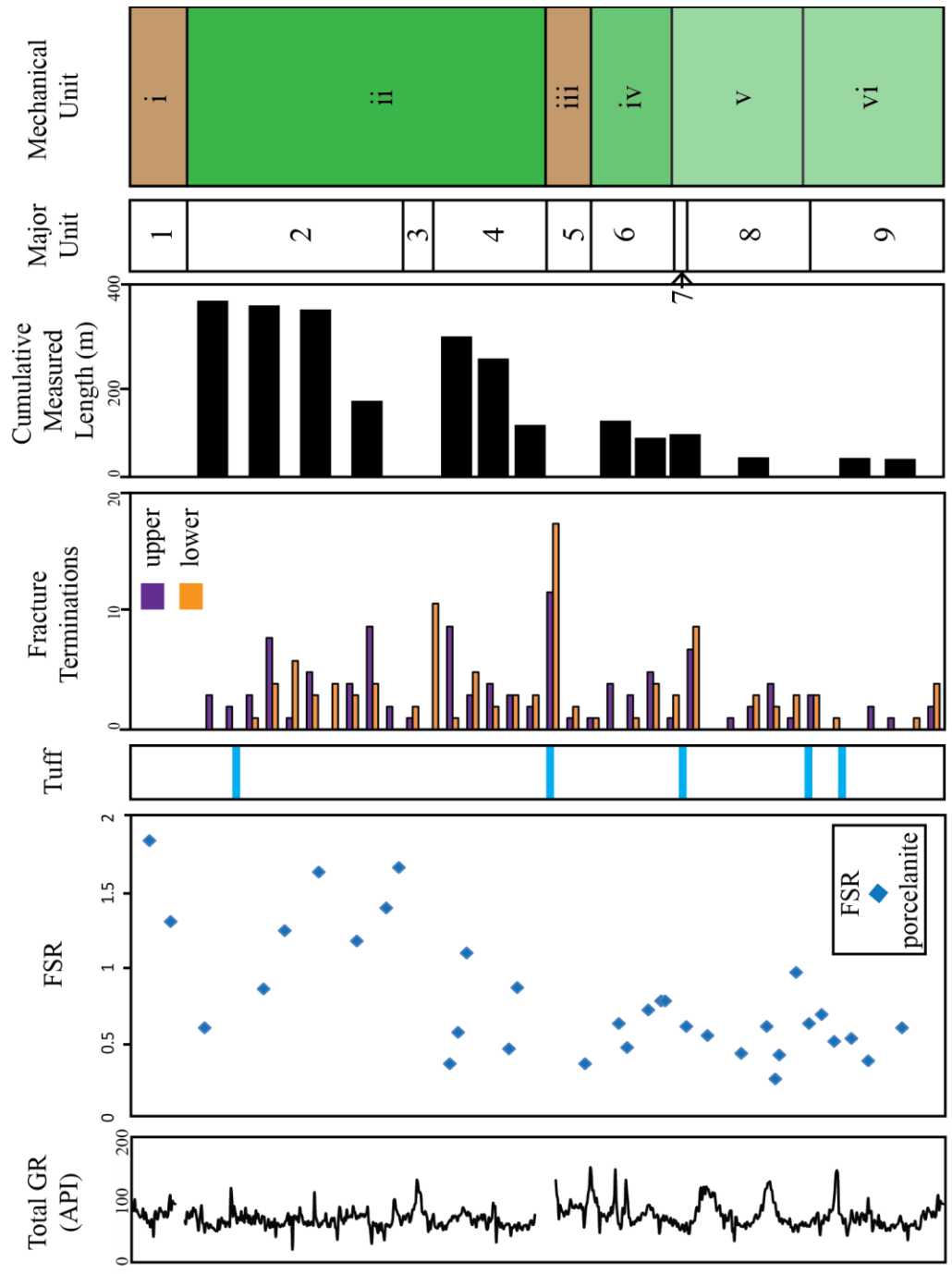
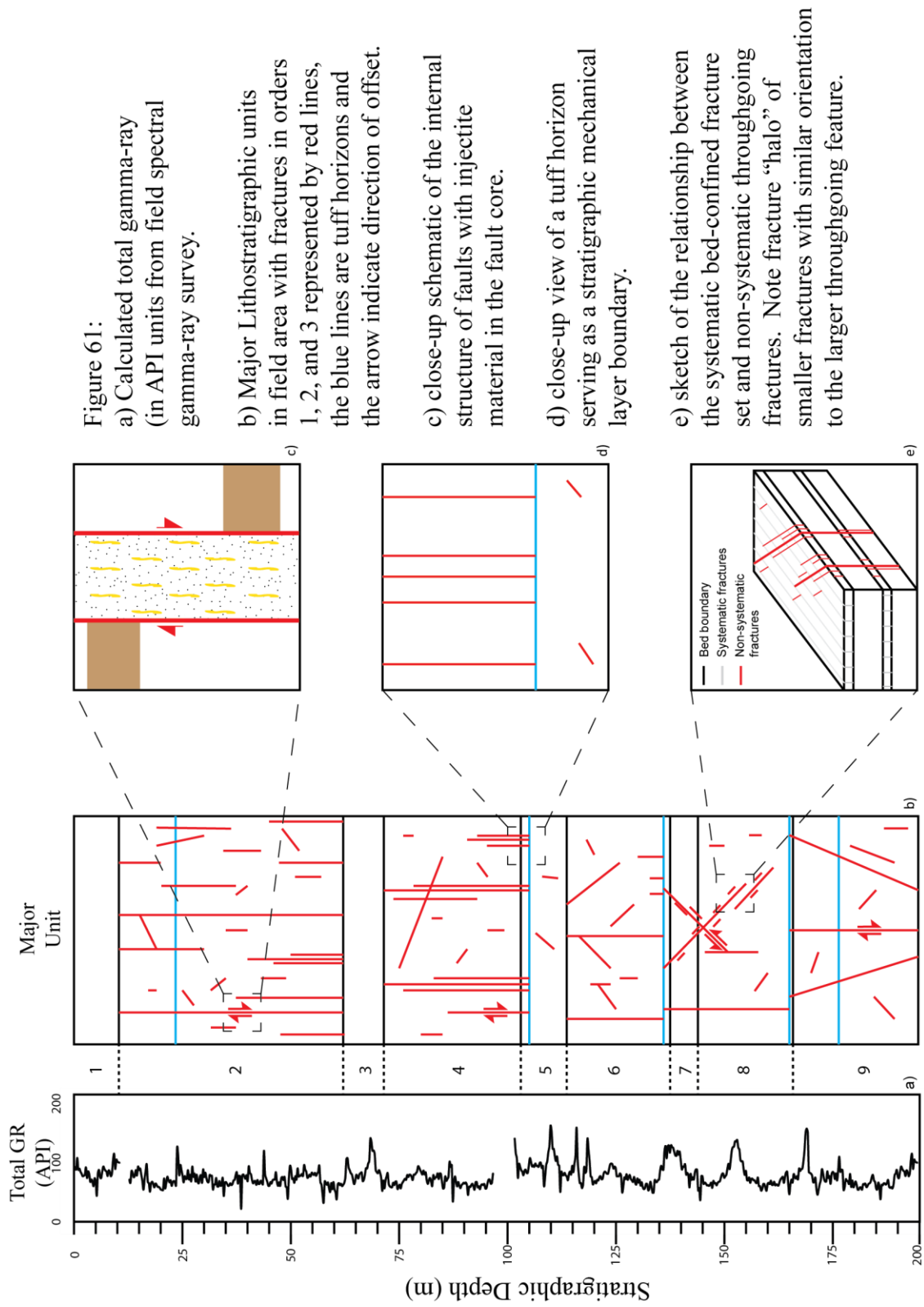


FIGURE 61. Conceptual model of the fracture network at Montana de Oro. The gamma-ray (left) is plotted on the left to show the correlation between major units and gamma-ray character.





## CHAPTER 5

### CONCLUSIONS

This study was undertaken to understand the relationship between mechanical and lithologic stratigraphy in the Monterey Formation at the reservoir level. The significant findings of this study at Montaña de Oro are: 1) gamma-ray results may be used to define stratigraphic architecture and related mechanical stratigraphy; 2) the delineation of three distinct fracture sets (A, B, and C) of multilayer fractures that are related to regional maximum horizontal stress; 3) bed-confined (4<sup>th</sup>-order) fracture intensity (FSR) variations due to primary stratal stacking can affect the subsequent development of multilayer fractures; 4) tuff horizons are the most effective single stratigraphic horizon that functions as a mechanical layer boundaries and are often associated with zones of intense fracturing; 5) and mudstone-dominated lithostratigraphic units greater than 10 m in thickness can compartmentalize fracture networks and may act as an important barrier to strain related to tectonic shortening; and 6) the northern and southern section express significant differences in multilayer fracture networks likely attributed to a combination of structural position (anisotropic strain) and stratigraphic character.

Implications of these findings to the petroleum industry will be valuable for characterization of naturally fractured reservoirs and in artificially induced hydraulic fracturing. For example, the application of correlating gamma-ray stratigraphy to potential mechanical stratigraphic units that may be more susceptible to multilayer

fracture development might be critical in prediction of fracture connectivity. Knowing the aspects of the stratigraphy that would likely terminate induced hydraulic fracturing (i.e. tuff horizons, thick mudstones, and thick mud-dominated intervals) can greatly affect landing zones and fracture stages in hydrocarbon reservoir exploitation.

## CHAPTER 6

### FUTURE WORK

This study has collected sufficient data to create a discrete fracture network model. Geocellular models of the fracture network may aid in understanding how this fracture network may behave in the subsurface. Fracture connectivity was not addressed in this study, and a discrete fracture model would address fracture connectivity and fluid flow through the fracture network. The orientation of the larger order fractures relative to the orientation of the bed-confined fractures could be critical in understanding which fracture set and what fracture length the most effective pathway for fluid to flow or be stored. It would be valuable to quantitatively assess the hydrologic properties of the fracture network at Montaña de Oro.

Another aspect that could be added to this study is to quantitatively assess the composition of the strata at Montaña de Oro. Sampling for quantitative compositional data could aid in the understanding of how much detritus mechanically affects the fracture system. This could be done by using a combination of x-ray diffraction (XRD), x-ray fluorescence (XRF), and Fourier transform infrared spectroscopy (FTIR) techniques. If samples were taken systematically in porcelanite beds throughout the area that had all ranges of fracture spacing ratios, a baseline may be established for the critical amount of detritus. This critical amount of detritus could aid in prediction of bed-confined fracture intensity, which subsequently affects the development of throughgoing

fractures. It may be valuable to try and calibrate the compositional data to the gamma-ray survey. If this were possible, then the values in the gamma-ray could be used to predict the amount of bed-confined fracturing and therefore possibly identify areas with the highest fracture intensity. Furthermore, geochemical and mineralogic compositional data could be correlated with measurement of rock properties that could then be used for correlation with observed fracture intensity and magnitude.

Field mapping the brittle deformation through the Pismo syncline northward towards the Los Osos fault would be useful to address whether or not these structural features are the cause of increased fracture density in the northern section. A quantitative and statistical analysis, similar to those of this study, could begin to assess areas of increased strain relative to structural position. Lastly, dolostone horizons should be sampled to analyze for included microfossils (diatoms, silicoflagellates) for biostratigraphic and paleomagnetism for improved dating of the stratigraphic succession. This will allow confident identification of the periodicity of the lithologic cycles and determination if they are Milankovitch-scale. Furthermore, paleomagnetic analysis will permit determination of any tectonic rotation that may be expected because of the field area's position between the Hosgri and West Huasna faults and also because of the suggestion from offset fractures that there may have been some Pliocene-Quaternary rotation of the stress field relative to the study area.

## APPENDICES

APPENDIX A

MAJOR AND MINOR LITHOSTRATIGRAPHIC UNIT MEASUREMENTS

A	B	C	D	E	F	G	H	I	J	K	L	M
1	13	A	6.9	11.3	4.5	25	13.9	7	32	0.81	1.85	5.61
		B	6.1	7.4	3	12	8	4	17	0.93	1.31	5.64
2	52	A	14.7	5.8	3	8	11	5	29	0.53	0.6	7.75
		B	12.1	5.5	2	9	3.6	2.5	6	1.53	0.86	18.49
		C	14.5	5.7	2.5	9	5.9	2.5	11	0.97	1.25	14.01
		D	4.6	5.9	4	10	9.7	3	23	0.61	1.18	2.80
		E	6.1	5.8	2	10	2.7	1	5	2.15	1.54	13.10
3	7	NA	NA	NA	NA	NA	NA	NA	NA	NA	NA	NA
4	29	A	4.8	4.9	1.5	10	2.3	1	3.5	2.13	0.36	10.23
		B	6.3	4.9	3	7	6.8	2	17	0.72	0.57	4.54
		C	6	5.5	2.5	12.5	3.75	3	9	1.47	1.1	8.80
		D	2.5	5.3	2	9	13.1	4	80	0.40	0.46	1.01
		E	9.4	4.4	2	7	3.2	2	5.5	1.38	0.87	12.93
5	12	A	5.1	2.8	1.5	4	4.2	2.5	7	0.67	NA	3.40
		B	6.9	5.6	1	11	27	6	105	0.21	0.36	1.43
6	24	A	8.1	5	2	10	11.7	2	55	0.43	0.63	3.46
		B	4.7	5.6	3	7	7.7	1	15	0.73	0.47	3.42
		C	11.2	4.6	1.5	7	3.2	1.5	5	1.44	0.72	16.10
7	6	NA	NA	4.8	1.6	10	4.5	4	10	1.07	0.55	6.40
8	22	A	1.5	6.6	3.5	13	2.6	1.9	3.4	2.54	0.43	3.81
		B	5.1	4.36	2.4	7.8	3.1	1.4	4.5	1.41	0.61	7.17
		C	2.1	4.1	1.8	7.8	4.2	1.8	5.4	0.98	0.26	2.05
		D	2.7	4	2	5.9	10.76	3.8	30.5	0.37	0.42	1.00
		E	2.7	4.35	1.5	10	3.2	0.6	4.4	1.36	0.97	3.67
		F	1.6	4.2	2.4	7.6	1.6	0.6	3.1	2.63	0.63	4.20

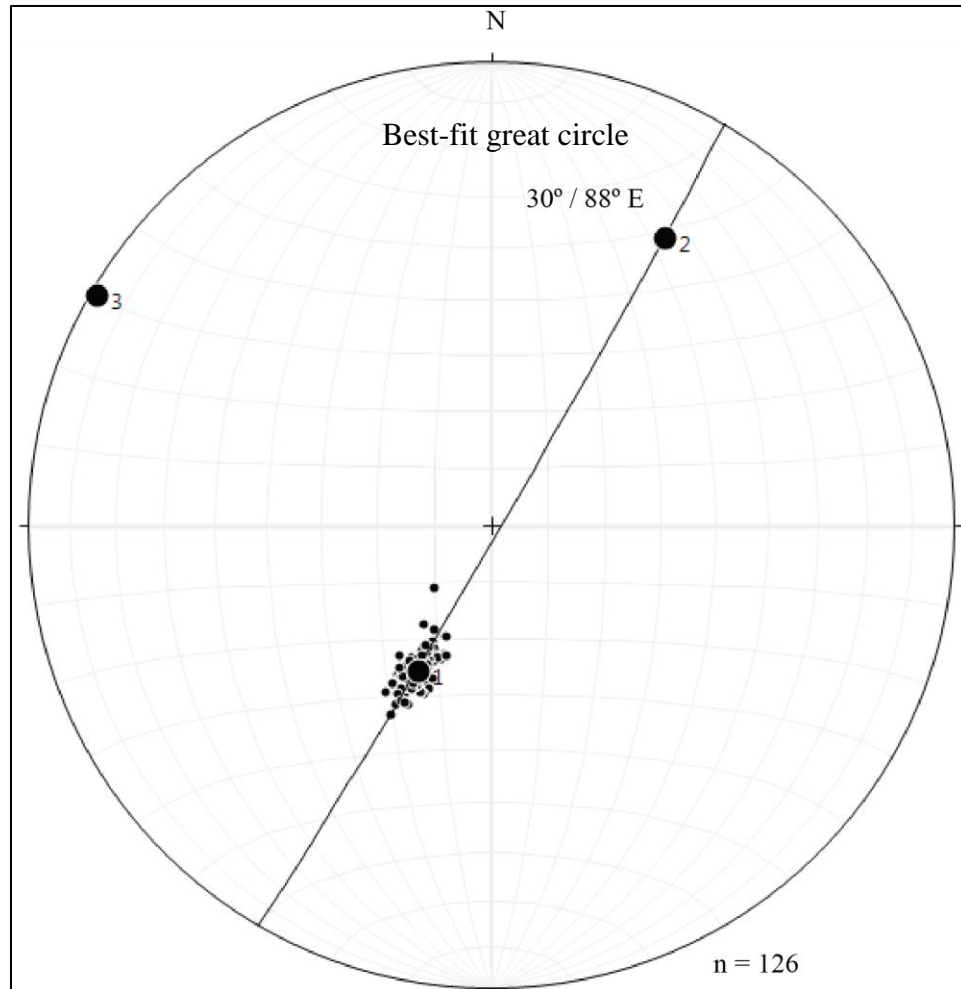


APPENDIX A. Continued

A	B	C	D	E	F	G	H	I	J	K	L	M
		G	6.3	4.8	1.9	7.9	2.8	0.8	6.6	1.71	0.69	10.80
9	29	A	3.1	4.5	2.5	8	16.2	3	83	0.28	0.51	0.86
		B	9.6	5.9	2	9	5.5	3	9	1.07	0.53	10.30
		C	16.3	4.7	3	8	4	1.5	7	1.18	0.6	19.15

Column description: A: major lithostratigraphic unit; B: major unit thickness (m); C: subunit; D: subunit thickness (m); E: average porcelanite bed thickness (cm); F: minimum porcelanite bed thickness (cm); G: maximum porcelanite bed thickness (cm); H: average mudstone bed thickness (cm); I: Minimum mudstone bed thickness (cm); J: maximum mudstone bed thickness (cm); K: porcelanite to mudstone ratio. NA: not available.

APPENDIX B  
STEREOPLOT OF BEDDING



The total number of bedding measurements taken is 126 ( $n = 126$ ).

APPENDIX C  
RESULTS OF 4<sup>TH</sup>-ORDER SCANLINE DATA FOR  
PORCELANITE AND MUDSTONE

Scan Line	Mean Fracture Strike	Mean Fracture Dip	Mean Spacing (cm)	Median Spacing (cm)	FSR	Number of Measurements
1A_POR	186	69	8.02	7.27	1.85	21
1B_POR	191	73	7.32	7.20	1.31	21
2A_POR	204	82	7.85	6.92	0.6	30
2B_POR	197	74	9.33	8.49	0.86	26
2C_MUD	210	84	15.67	15.92	0.71	20
2C_POR	244	75	5.00	4.55	1.25	24
2D_POR	185	60	6.85	5.61	1.64	108
2E_POR	191	72	5.00	4.24	1.18	20
2F_POR	199	74	10.49	8.99	1.4	24
2G_POR	196	69	5.00	4.56	1.67	25
4A_POR	200	78	12.65	12.74	0.36	23
4B_MUD	205	89	16.39	16.99	1.04	20
4B_POR	201	85	9.72	9.47	0.57	24
4C_POR	205	84	8.38	7.00	1.1	21
4D_MUD	210	89	5.75	5.50	0.62	20
4D_POR	207	86	12.46	11.96	0.46	24
4E_POR	208	85	7.80	5.98	0.87	23
5B_MUD	228	41	18.44	7.87	0.48	10
5B_POR	201	85	12.63	12.45	0.36	22
6A_POR	203	82	12.08	9.40	0.63	24
6B_POR	196	82	15.45	14.84	0.47	24
6C_MUD	195	84	21.88	10.43	1.1	9
6C_POR	217	81	9.98	8.95	0.72	23
6D_POR	212	88	10.29	6.50	0.78	24
6E_POR	218	87	16.42	12.98	0.78	16
6F_POR	26	86	10.36	7.98	0.61	23
7_MUD	215	73	72.49	54.83	0.15	7
7_POR	207	85	16.91	15.96	0.55	21
8A_POR	213	88	11.19	8.00	0.43	25
8B_POR	211	87	5.54	5.49	0.61	22
8C_POR	215	85	15.43	15.95	0.26	21
8D_POR	213	89	14.09	15.00	0.42	22
8E_MUD	21	89	21.42	16.99	0.31	21
8E_POR	216	86	5.59	3.99	0.97	23

APPENDIX C. Continued

Scan Line	Mean Fracture Strike	Mean Fracture Dip	Mean Spacing (cm)	Median Spacing (cm)	FSR	Number of Measurements
8E_POR_1	34	89	10.90	10.20	0.63	41
8G_POR	216	87	7.04	5.99	0.69	21
9A_POR	223	77	18.15	13.64	0.51	8
9B_MUD	31	81	21.21	10.36	0.48	6
9B_POR	211	87	6.23	5.99	0.53	21
9C_POR	211	86	9.80	9.97	0.38	29
9D_POR	208	84	7.82	5.96	0.6	24

List of abbreviations: scanline column represents the name of the scanline and its geographic position relative to the major and minor lithostratigraphic units. For example, 2A\_POR would be a scanline measured in major unit 2, subunit A, in porcelanite; 2A\_MUD would be a scanline measured in major unit 2, subunit A, in mudstone; fracture strike and dip are in degrees using the right-hand-rule described in the Methods section; fracture spacing ratio (FSR).

APPENDIX D  
SUMMARY OF 4<sup>TH</sup>-ORDER DATA IN THE NORTHERN (UPPER) AND  
SOUTHERN (LOWER) SECTIONS

Section	Average Fracture Strike	Average Fracture Dip	Average Spacing (cm)	Median Spacing (cm)	FSR	Number of Measurements
Northern	205	81	9.34	6.62	1.15	414
Southern	214	86	12.49	11.01	0.55	819

List of abbreviations: fracture spacing ratio (FSR).



APPENDIX E

MEASUREMENTS OF FEATURES IN FRACTURE ORDERS 1-3

Feature	Major unit	Strike	Dip	FO	Length (in situ)	Strat Length (m)	Type of shear	Mean width (cm)	Min width (cm)	Max width (cm)
1	8	42.5	90	2	9.79*	4.76*	Opening	27.3	24.0	30.5
2	8	32.5	88	2	13.09	6.17	Opening	9.3	1.8	17.5
3	8	165.5	80	2	23.18*	11.69*	Normal	3.7	0.5	7.0
4	8	42.5	85	3	4.43*	2.15*	Opening	5.1	2.2	8.0
5	8	31.5	87	3	7.75	3.65	Opening	8.0	3.0	16.0
6	8	2.5	79	3	3.8	1.96	Opening	4.4	2.4	8.0
7	8	165.5	88	3	14.06	7.09	Opening	9.1	3.0	16.2
8	8	173.5	89	2	38.9	20.98	Normal	11.2	1.2	22.0
9	8	63.5	85	1	26.8	15.65	Normal	36.1	2.0	117.0
10	6	18.5	90	3	3.75	1.78	Opening	5.8	4.0	7.5
11	8	28.5	90	1	25*	11.74*	Opening	NM	NM	NM
12	2	30.5	86	1	95.5*	44.91*	RT LT	19.5	8.0	27.0
13	2	15.5	84	3	5.8	2.78	SS	8.0	1.0	20.0
14	2	21.5	87	2	33.8	15.94	Opening	9.0	1.0	21.0
15	2	27.5	85	2	36.9*	17.32*	Normal	20.7	19.0	23.0
16	2	26.5	84	2	21.25*	9.97*	Opening	12.3	3.0	23.0
17	2	55.5	82	3	8.7	4.65	Opening	1.3	1.0	2.0
18	2	39.5	86	3	26.1*	12.55*	Opening	9.8	3.0	18.0
19	2	34.5	89	2	17.1*	8.09*	Opening	4.3	1.0	9.0
20	2	23.5	85	2	37.7*	17.73*	RT LT	15.8	3.0	33.0
21	2	54.5	NM	3	8.8*	4.65*	Opening	5.6	4.0	7.0
22	2	27.5	87	3	15.2	7.14	Opening	9.0	3.0	15.0

APPENDIX E. Continued

Feature	Major unit	Strike	Dip	FO	Length (in situ)	Strat Length (m)	Type of shear	Mean width (cm)	Min width (cm)	Max width (cm)
							SS +			
24	2	12.5	88	2	42.1	20.42	NORMAL	12.4	4.0	22.0
25	2	35.5	86	3	10.2	4.84	Opening	3.0	1.0	6.0
26	2	6.5	83	2	29.8*	14.93*	Normal	14.0	10.0	16.0
27	2	60	82	3	6.45	3.61	Opening	2.7	2.0	3.0
28	2	44.5	88	3	3	1.48	Opening	2.5	0.5	4.0
29	2	61.5	85	3	8.4	4.79	Opening	4.2	1.5	8.3
30	2	28.5	89	2	19.9*	9.345*	Opening	18.2	11.0	26.5
31	2	29.5	89	3	9.05*	4.25*	Opening	2.2	3.0	3.5
32	2	28.5	90	2	34.8*	16.34*	Normal +SS	7.1	4.5	10.0
33	2	21.5	85	2	31.6*	14.90*	Opening	24.6	9.5	60.0
34	2	22.5	84	2	12.6*	5.93*	Opening	18.1	3.5	42.0
35	2	27.5	84	2	12.6*	5.91*	Opening	16.3	10.0	27.0
36	2	169.5	76	3	13.7	7.13	Opening	4.7	2.0	9.0
37	4	23.5	88	2	18.6	8.75	Opening	11.6	2.5	21.0
38	4	31.5	85	2	25.5	12.01	Opening	6.0	3.0	11.0
39	9	87.5	59	2	7.35*	7.00*	Normal	7.0	7.0	7.0
40	9	28.5	90	1	21.7*	10.19*	RT LT	26.9	5.5	52.0
41	9	63.5	55	3	7.8*	4.55*	Normal	4.0	4.0	4.0
42	9	158.5	80	3	16.65	8.07	Opening	5.0	5.0	5.0
43	9	35.5	78	3	6.08*	2.88*	Opening	8.8	6.0	12.0

APPENDIX E. CONTINUED

Feature	Major unit	Strike	Dip	FO	Length (in situ)	Strat Length (m)	Type of shear	Mean width (cm)	Min width (cm)	Max width (cm)
45	9	51.5	50	3	10.55	5.44	Opening	1.8	0.5	3.0
46	4	29.5	81	2	49.5*	23.26*	Opening	20.5	9.0	32.0
47	4	59.5	79	2	12.4*	6.90*	Opening	7.5	7.0	8.0
48	4	36.5	90	2	27.6	13.14	Opening	12.0	6.0	22.0
49	4	25.5	82	3	16.1	7.56	Opening	5.7	3.0	9.0
50	4	37.5	89	3	9.6	4.58	Opening	3.8	2.0	5.5
51	4	31.5	90	2	17.8	8.38	Opening	5.8	2.0	8.5
52	4	35.5	85	3	14.2	6.74	Opening	7.5	7.0	8.0
53	4	36.5	87	3	14.4*	6.85*	Opening	4.0	3.0	5.0
54	4	85.5	55	3	9.4*	8.44*	Opening	3.2	2.5	4.0
55	4	159.5	29	2	16.15	7.87	Opening	2.0	0.5	3.5
56	4	21.5	86	2	27.5	12.97	Opening	13.0	5.0	25.0
57	4	1.5	69	3	19.1	9.93	Opening	3.0	3.0	4.0
58	4	19.5	81	2	22.8*	10.79*	RT LT?	13.8	7.0	19.0
59	4	32.5	83	2	36.05*	17.00*	Opening	10.3	5.0	18.0
60	6	67.5	89	2	8.85	5.46	Opening	4.5	3.0	6.0
61	6	35.5	84	2	16.1	7.64	Reverse	11.8	2.0	34.0
62	6	30.5	89	3	11.1*	5.22*	Opening	4.3	1.0	10.0
63	6	26.5	86	1	32.8*	15.39*	RT LT	67.0	52.0	82.0
64a	6	64.5	73	3	8.8	5.21	Opening	15.0	15.0	15.0
64b	6	26.5	87	3	2.7	1.27	Opening	19.0	10.0	28.0

APPENDIX E. Continued

Feature	Major unit	Strike	Dip	FO	Length (in situ)	Strat Length (m)	Type of shear	Mean width (cm)	Min width (cm)	Max width (cm)
64c	6	64.5	82	3	15.5	9.17	Normal	4.5	2.5	7.0
65	6	28.5	85	3	14.35	6.74	Opening	12.3	5.0	27.0
66	6	5.5	77	3	12.6	6.36	Opening	8.0	2.0	14.0
67	6	27.5	82	2	24.3*	11.40*	Opening	NM	NM	NM
68	6	175.5	84	2	34.1*	18.77*	Opening	2.0	1.0	3.0
69	6	47.5	83	2	18.4	9.22	Opening	7.0	4.0	11.0
70	6	35.5	89	3	6.16*	2.924*	Opening	16.3	5.5	24.0
71	5	103.5	80	3	2.1	4.22	Opening	2.5	2.5	2.5
72	5	133.5	88	3	4.2	2.01	Opening	2.5	2.0	3.0
73	5	28.5	89	2	12.55*	5.89*	RT LT	14.7	8.0	22.0
74	4	52.5	85	3	4.4	2.29	Opening	8.7	4.0	12.0
75	4	34.5	81	3	2.58	1.22	Opening	7.0	4.0	11.0
76	4	33.5	87	2	6*	2.83*	RT LT	6.0	6.0	6.0
77	4	37.5	82	2	6*	2.86*	Opening	9.0	8.0	10.0
78	4	26.5	88	3	4.5*	2.11*	Opening	4.0	2.0	7.0
79	4	30.5	87	2	6*	2.82*	Opening	27.0	21.0	32.0
80	4	25.5	86	2	6*	2.81*	Opening	NM	NM	NM
81	4	32.5	82	3	4.68	2.21	Opening	2.2	1.5	3.0
82	4	30.5	84	2	6*	2.82*	Opening	44.3	42.0	48.0
83	4	30.5	85	2	6	2.82	Opening	12.5	10.0	15.0
84	4	28.5	88	3	2.9*	1.36*	Opening	2.5	2.0	3.0

APPENDIX E. Continued

Feature	Major unit	Strike	Dip	FO	Length (in situ)	Strat Length (m)	Type of shear	Mean width (cm)	Min width (cm)	Max width (cm)
85	6	35.5	82	3	2.9*	1.37*	Opening	10.5	5.0	16.0
86	6	74.5	76	3	3.2*	2.22*	Opening	9.7	5.0	17.0
87	8	13.5	69	3	4*	1.93*	Opening	10.4	4.0	27.0
88	8	22.5	89	2	4*	1.88*	UNK	11.3	7.0	14.0
89	2	172.5	81	3	15.1*	8.06*	Opening	12.6	1.5	29.0
90	2	67.5	89	3	31.4	19.39	Opening	4.0	3.0	5.0
91	2	61.5	78	3	17.1	9.74	Opening	9.0	8.0	10.0
92	2	24.5	85	2	17.1	8.04	Opening	5.8	5.0	7.0
93	2	25.5	88	2	32.2	15.12	Opening	7.7	3.0	10.0
94	2	25.5	84	2	31.8	14.93	Opening	6.8	3.0	10.0
95	2	22.5	86	3	15.3	7.21	Opening	5.3	1.0	10.0
96	2	68.5	86	3	NM	NM	Opening	14.3	5.0	26.0
97	2	67.5	86	3	4	2.47	Opening	5.0	1.0	12.0
98	2	68.5	86	3	4.9	3.07	Opening	4.0	3.0	5.0
100	4	20.5	89	1	50*	23.62*	RT LT	15.3	4.0	39.0
101	4	167.5	72	2	15	7.68	Opening	6.0	2.0	11.0
102	4	24.5	NM	1	50*	23.49*	Opening	NM	NM	NM
103	4	74.5	NM	2	6	4.17	Opening	1.8	1.0	2.0
104	4	36.5	86	3	9.65	4.59	Opening	11.0	8.0	15.0
106	6	25.5	NM	3	NM	NM	Opening	NM	NM	NM
107	2	25.5	85	3	11.4	5.35	Opening	8.8	4.0	14.0

APPENDIX E. Continued

Feature	Major unit	Strike	Dip	FO	Length (in situ)	Strat Length (m)	Type of shear	Mean width (cm)	Min width (cm)	Max width (cm)
108	2	28.5	90	2	34.5	16.20	Opening	21.5	17.0	27.0
109	2	75.5	82	3	11.65	8.25	Opening	1.5	1.0	2.0

List of abbreviations: Heading: fracture order (FO); columns: not measureable (NM); \* minimum length; right-lateral strike-slip (RT LT); strike slip (SS); unknown (UNK); stratigraphic (strat).

APPENDIX F

RESULTS OF SCANLINE MEASUREMENTS FOR FRACTURE ORDERS 1-3



Scanline	# features /10m	# features	Scanline length (m)	cumulatve measured trace length (m)	cumulative trace length/m SL	Cumulative Stratigraphic Length (m)	Cumulative Stratigraphic Length per meters SL	Mean Spacing (m)
MU2_1	1.748	9.00	51.50	373.00	213.44	246.95	4.80	6.70
MU2_2	1.837	9.00	49.00	362.90	197.58	170.46	3.48	4.63
MU2_3	2.079	11.00	52.90	354.40	170.43	158.64	3.00	5.08
MU2_4	2.222	7.00	31.50	161.20	72.54	60.95	1.93	5.20
MU4_1	3.802	10.00	26.30	297.50	78.24	141.23	5.37	3.00
MU4_2	3.162	8.00	25.30	250.65	79.27	119.39	4.72	3.57
MU4_3	3.745	5.00	13.35	110.00	29.37	52.85	3.96	3.09
MU6_1	2.747	5.00	18.20	119.30	43.43	61.11	3.36	3.59
MU6_2	2.604	5.00	19.20	83.15	31.93	40.21	2.09	3.65
MU7	1.875	3.00	16.00	90.70	48.37	48.38	3.02	7.50
MU8_2	1.829	3.00	16.40	44.02	24.06	21.52	1.31	7.55
MU9_1	1.481	4.00	27.00	40.10	27.07	22.63	0.84	8.70
MU9_2	1.364	3.00	22.00	38.20	28.01	20.08	0.91	8.70

List of abbreviations: # features/10m: number of features per ten meters of scanline length; # features: number of features intersected along a scanline scanline SL; MU2\_1: scanline name by major unit number and number of scanline from north to south; m: meter.

APPENDIX G

SUMMARY OF SCANLINE MEASUREMENTS FOR FRACTURES IN ORDERS 1-3 FOR  
THE NORTHER (UPPER) AND SOUTHERN (LOWER) SECTIONS

Scanline	# Features /10m	Cumulative Measured Trace Length (m)	Cumulative Trace Length/m SL	Cumulative Stratigraphic Length (m)	Cumulative Stratigraphic Length/m SL	Average Spacing (m)
northern	2.66	272.81	120.12	135.78	3.89	4.47
southern	1.98	69.25	33.81	35.66	1.92	6.62

List of abbreviations: # features/10m: number of features per ten meters of scanline length; # features: number of features intersected along a scanline scanline SL; MU2\_1: scanline name by major unit number and number of scanline from north to south; m: meter.

## APPENDIX H

### LIST OF UPPER AND LOWER TERMINATION IN FRACTURE ORDERS 1-3

Feature	Lower Termination	Upper Termination
1	unk	rock mass
2	rock mass	rock mass
3	unk	rock mass
4	rock mass	rock mass
5	rock mass	rock mass
6	rock mass	rock mass
7	rock mass	rock mass
8	rock mass	tuff
9	set A	tuff
10	rock mass	tuff
11	unk	tuff
12	rock mass	unk
13	rock mass	rock mass
14	rock mass	rock mass
15	unk	rock mass
16	unk	rock mass
17	rock mass	set A
18	rock mass	rock mass
19	rock mass	rock mass
20	unk	unk
21	set A	unk
22	rock mass	set A
23	unk	unk
24	rock mass	rock mass
25	rock mass	set A
26	rock mass	rock mass
27	set A	set A
28	rock mass	rock mass
29	rock mass	unk
30	unk	rock mass
31	unk	rock mass
32	unk	unk
33	unk	unk
34	rock mass	unk
35	rock mass	unk
36	rock mass	rock mass
37	rock mass	rock mass

APPENDIX H. Continued

Feature	Lower Termination	Upper Termination
38	rock mass	rock mass
39	unk	unk
40	unk	tuff
41	set A	tuff
42	rock mass	rock mass
43	tuff	unk
44	rock mass	rock mass
45	rock mass	rock mass
46	unk	rock mass
47	unk	set A
48	set a	unk
49	unk	rock mass
50	unk	rock mass
51	unk	unk
52	rock mass	unk
53	rock mass	rock mass
54	set A	unk
55	rock mass	rock mass
56	rock mass	unk
57	rock mass	rock mass
58	unk	unk
59	rock mass	unk
60	unk	unk
61	unk	unk
62	rock mass	rock mass
63	unk	unk
64A	set A	rock mass
64B	rock mass	rock mass
64C	rock mass	rock mass
65	rock mass	rock mass
66	rock mass	rock mass
67	unk	set A
68	unk	rock mass
69	rock mass	rock mass
70	tuff	unk

APPENDIX H. Continued

Feature	Lower Termination	Upper Termination
71	rock mass	rock mass
72	rock mass	tuff
73	tuff	unk
74	rock mass	rock mass
75	rock mass	rock mass
76	unk	unk
77	unk	unk
78	unk	unk
79	unk	unk
80	unk	unk
81	unk	rock mass
82	unk	unk
83	unk	rock mass
84	unk	unk
85	tuff	unk
86	tuff	unk
87	tuff	unk
88	tuff	unk
89	unk	unk
90	set A	rock mass
91	set A	rock mass
92	set A-splay	rock mass
93	set A-splay	rock mass
94	set A-splay	rock mass
95	set A-splay	rock mass
96	set A	set A
97	set A	set A
98	rock mass	unk
99	unk	rock mass
100	unk	unk
101	set A	set A
102	unk	unk
103	rock mass	rock mass
105	rock mass	rock mass
106	unk	unk

APPENDIX H. Continued

Feature	Lower Termination	Upper Termination
107	rock mass	rock mass
108	rock mass	rock mass
109	rock mass	set A

List of abbreviations: unknown fracture termination (unk); fracture set A (set A).



APPENDIX I

SUMMARY OF FRACTURE TERMINATIONS FOR ORDERS 1-3

Termination Horizon	Upper Termination	Lower Termination	Total
rock mass	51	47	98
set A	10	16	26
set B	0	0	0
set C	0	0	0
tuff	7	7	14
unk	37	38	75

List of Abbreviations: set A: fracture set A; set B: fracture set B; set C: fracture set C; unk: unknown.

APPENDIX J

STRESS DATA FROM THE WORLD STRESS MAP PROJECT

Latitude	Longitude	SHazimuth	Type	Quality	Regime	Depth	Site
35.12	-120.97	53	BOT	C	TS	1.7	SEA2477
34.49	-120.62	36	BOT	B	TS	1.7	SEA2479
35.26	-120.65	25	BO	C	U	0.8	SEA559
34.97	-120.65	21	BO	C	U	0.88	SEA560
34.76	-120.75	57	BO	B	U	0	SEA563
34.68	-120.7	72	BO	B	U	0	SEA564
35.12	-120.57	32	FMF	A	TF	8	USA1210
34.85	-120.27	9	BO	B	U	1.34	USA270
34.85	-120.27	44	BO	B	U	1.33	USA271
34.72	-120.23	56	BO	A	U	1.02	USA272
35.76	-120.55	16	BO	A	U	1.7	USA290
34.79	-120.22	44	BO	B	U	1.63	USA293
34.82	-120.31	53	BO	B	U	1.46	USA296
35.84	-120.11	58	BO	C	U	0.88	USA305
35.27	-120.01	24	BO	C	U	1.71	USA319
35.89	-120.8	57	BO	B	U	0.94	USA320
35.99	-120.91	42	BO	B	U	0.8	USA339
35.99	-120.25	43	BO	C	U	1.02	USA340
35.93	-120.14	40	BO	B	U	2.36	USA396
34.87	-120.36	55	FMS	C	TF	4.8	USA684

List of abbreviations: maximum horizontal stress azimuth (SHazimuth); borehole televiewer-imaged shapes of borehole breakout (BOT) borehole breakout (BO); focal mechanism, formal inversion (FMF); focal mechanism, single (FMS); thrust faulting with strike-slip component (TS); thrust faulting (TF); unknown (U); latitude and longitude in universal Mercator; Montaña de Oro State Park is located at 35.26, -120.26 (latitude, longitude).

## REFERENCES

## REFERENCES CITED

- Atwater, T., 1970, Implications of plate tectonics for the tectonic evolution of western North America: *Geological Society of America Bulletin*, vol. 81, p. 3513-3536.
- Aydin, A., 2000, Fractures, faults, and hydrocarbon entrapment, migration and flow: *Marine and Petroleum Geology*, v. 17, no. 7, p. 797-814.
- Bai, T., and Pollard, D.D., 2000, Fracture spacing in layered rocks: A new explanation based on the stress transition; *Journal of Structural Geology*, v. 22, p. 43-57.
- Barron, J.A., 1986, Paleooceanographic and tectonic controls on deposition of the Monterey Formation and related siliceous rocks in California; *Paleoceanography, Paleoclimatology, Paleoecology*, v. 53, p. 27-45.
- Behl, R. J., 1998, Relationships between silica diagenesis, deformation and fluid flow in Monterey Formation cherts, Santa Maria basin, California, *In* Eichhubl P., ed., diagenesis, deformation, and fluid flow in the Miocene Monterey Formation, Special Publication Pacific Section SEPM: Society for Sedimentary Geology, v. 83, p. 77-83.
- Behl, R. J., 1999, Since Bramlette (1946)-The Miocene Monterey Formation of California revisited: *GSA Special Paper* 338.
- Behl, R. J., and Garrison, R. E., 1994, The origin of chert in the Monterey Formation of California, *in* Proc, International Geologic Congress; 29<sup>th</sup>: Utrecht, VSP, part C., p. 101-1032.
- Blake, M.C., Campbell, R.H., Diblee, T.W., Howell, D.G., Nilsen, T.H., Normark, W.R., Vedder, J.C., and Silver, E.A., 1978, Neogene basin formation in relation to plate-tectonic evolution of the San Andreas fault system, California: *American Association of Petroleum Geologists Bulletin*, v. 62, no. 3, p. 344-372.
- Bramlette, M. N., 1946. The Monterey Formation of California and the origin of its siliceous rocks: *United States Geological Survey, Professional Paper* 212, p. 57.
- Crowell, J. C., 1987, Late Cenozoic basins of onshore southern California-Complexity is the hallmark of their tectonic history, *in* *Cenozoic Basin Development of Coastal California*: Eaglewood Cliffs, Prentice Hall, v. 6, p. 207-241.

- Davis, G. H., and Reynolds, S. J., 1996, Structural geology of rocks and regions: Eaglewood Cliffs, John Wiley and Sons, Inc., 4 p.
- Dibblee, T. W., Jr., (1982) Regional geology of the Transverse Ranges province of California, *in* Geology and Mineral Wealth of the California Transverse Ranges, New York, McGraw-Hill, p. 7-26.
- Ellis, D. V., and Singer, J.M., 2007, Well Logging for Earth Scientists, 2<sup>nd</sup> Edition, The Netherlands, Springer, p. 275.
- Eyal, Y., Gross, M. R., Engelder, T., Becker, A., 2001, Joint development during fluctuation of the regional stress field in southern Israel: *Journal of Structural Geology*, v. 23, p. 279-297.
- Fairbanks, H.W., 1904, Description of the San Luis Quadrangle, California : U.S. Geological Survey Geologic Atlas of the United States, San Luis folio, no. 101, 14 p., scale 1:125,000.
- Finkbeiner, T., Barton, C. A., Zoback, M. D., 2007, Relationships Among in-situ stress, fractures and faults, and fluid flow-Monterey Formation, Santa Maria Basin, California: *AAPG Bulletin*, v. 81, no. 12, p. 1975-1999.
- Finn, M. D., Gross, M. R., Eyal, Y., Draper, G., 2003, Kinematics of throughgoing fractures in jointed rocks: *Tectonophysics* v. 376, p. 151-166.
- Ghosh, K., and Mitra, S., 2009, Structural controls on fracture orientations, intensity, and connectivity, Teton anticline, Sawtooth Range, Montana: *AAPG Bulletin*, v. 93, no. 8, p. 995-1014
- Gross, M. R., 1995, Fracture partitioning: failure mode as a function of lithology in the Monterey Formation of coastal California: *GSA Bulletin*, v. 107, no. 7, p. 779-792.
- Gross, M. R., and Engelder, T., 1995, Strain accommodated by brittle failure in adjacent units of the Monterey Formation, U.S.A.: scale effects and evidence for uniform displacement boundary conditions: *Journal of Structural Geology*, v. 17, no. 9, p. 1303-1318.
- Gross, M. R., Fischer, M. P., Engelder, T., Greenfield, R. J., 1995, Factors controlling joint spacing in interbedded sedimentary rocks: integrating numerical models with field observations from the Monterey Formation, USA: *Geological Society of America special publication* No. 92, p. 215-233.

- Gutierrez-Alanzo, G., and Gross, M. R., 1997, Geometry of inverted faults and related folds in Monterey Formation-implications for the structural evolution of the southern Santa Maria basin, California: *Journal of Structural Geology*, vol. 19, no. 10, p. 1303-132.
- Hall, C. A., Jr., 1975, San Simeon-Hosgri fault system, coastal California: economic and environmental implications: *Science*, p. 190, 1291-1294.
- Hall, C. A., Jr., 1981a, San Luis Obispo transform fault and Middle Miocene rotation of the western Transverse Ranges, California: *Journal of Geophysics*, v. 85, p. 1015-1031.
- Hall, C. A., Jr., 1981b, Evolution of the western Transverse Ranges microplate: late Cenozoic faulting and basinal development, *in* the Geotectonic Development of California, Upper Saddle River, Prentice Hall, v. 1, p. 559-582.
- Hanson, K.L., Lettis, W. R., McKlaren, M. A., Savage, W. U., Hall, N. T., 1995, Style and rate of quaternary deformation of the Hosgri fault Zone, offshore south central California: *U.S. Geological Society Bulletin, Evolution of Sedimentary Basins/Offshore Oil and Gas Investigations-Santa Maria Province*, Chapter BB.
- Hardebeck, J. L., 2010, Seismotectonics and fault structure of the California Central Coast: *Bulletin of the Seismological Society of America*, v. 100, no. 3, p. 1031-1050.
- Hardebeck, J. L., 2013, Geometry and earthquake potential of the Shoreline fault, central California: *Bulletin of the Seismological Society of America*, v. 103, no. 1, p. 447-462.
- Hennings, P. H., Olson, J. E., Thompson, L. B., 2000, Combining outcrop data and three-dimensional structural models to characterize fractured reservoirs-an example from Wyoming: *AAPG Bulletin*, v. 84, no. 86, p. 830-849.
- Hill, P., 2005, Use of Milankovich cyclicity as a high-resolution dating and correlation tool in the upper Neogene sediments of the Monterey and Sisquoc formations of the Santa Maria basin of the central California margin, California State University.
- Imbrie, J., Boyle, E. A., Clemens, S. C., Duffy, A, 1992, On the structure and origin of major glaciation cycles 1. Linear response to Milankovitch forcing: *Paleoceanography*, v. 7, no. 6, p. 701-738.
- Ingle, Jr. J. C., 1981, Cenozoic depositional history of the northern continental borderland of southern California and the origin of associated Miocene diatomites, *in* Guide



to the Monterey Formation in the California Coastal Area, Ventura to San Luis Obispo: Menlo Park, Pacific Section AAPG, . 1-8.

- Issacs, C. M., 1981a Lithostratigraphy of the Monterey Formation, Goleta to Point Conception, Santa Barbara Coast, California *in* Guide to the Monterey Formation in the California Coastal Area, Ventura to San Luis Obispo: Menlo Park, Pacific Section AAPG, p. 9-23.
- Issacs, C. M., 1981b, Outline of diagenesis in the Monterey Formation examined laterally along the Santa Barabara coast, California, *in* Guide To the Monterey Formation in the California Coastal Area, Ventura to San Luis Obispo: Menlo Park, Pacific Section AAPG, p. 25-38.
- Issacs, C. M., 1981c, Field characterization of rocks in the Monterey Formation along the Coast Near Santa Barbara, California, *in* Guide To the Monterey Formation in the California Coastal Area, Ventura to San Luis Obispo: Menlo Park, Pacific Section AAPG, p. 39-54.
- Keller, M. A, 1992, Field guide to the Upper Miocene siliceous coastal sequence of Montana de Oro State Park, California, Menlo Park, Pacific Section AAPG, p. 67-80.
- Ladeira, F. R., and Price, N. J., 1981, Relationship between fracture spacing and bed thickness: *Journal of Structural Geology*, vol. 3, no. 2, p. 179-183.
- Laubach, St. E., Olson, J. E., Gross, M. R., 2009, Mechanical and fracture stratigraphy: *AAPG Bulletin*, v. 93. no. 11, p. 1414-1426.
- Lettis, W. R., and Hanson, K. L., 1992, Quaternary tectonic influences on coastal morphology, South-Central California: *Quaternary International*, v. 15/16, p. 135-148.
- Lettis, W. R., and Hall, N. T., 1994, Los Osos fault zone, San Luis Obispo County, California, *in* Alterman, I. B. McMullen, R. B., Cluf, L. S., and Slemmons, D. B., eds., *Seismotectonics of the Central California Coast Ranges*: Boulder, Colorado, Geological Society of America Special Paper 292.
- McCrary, P. A., Wilson, D. S., Ingle, J. C Jr., Stanely, R. G., 1999, Neogene geohistory analysis of the Santa Maria basin, California, and it's relationship to transfer of central California to the Pacific Plate: *in* Keller Margaret A. ed., *Evolution of sedimentary basins/onshore oil and gas explorations—Santa Maria Province*.
- Miller, K.C., 1992, Crustal structure along the strike of the offshore Santa Maria Basin, California: *Tectonophysics*, v. 219, p. 57-69.

- Narr, W., and Suppe, J., 1991, Joint spacing in sedimentary rocks: *Journal of Structural Geology*, v. 11, no. 9, p. 1037-1048.
- Pacific Gas and Electric Company, 1988, 2008, 2011, Long Term Seismic Program report.
- Pisciotta, K.A., and Garrison, R.E., 1981, Lithofacies and depositional environments of the Monterey Formation, California: *in* Garrison, R.E., and Douglas, R.G., eds., *The Monterey Formation and related siliceous rocks of California*, Society for Sedimentary Geology, p. 97-122.
- Rijken, P., and Cooke, M. L., 2001, Role of shale thickness on vertical connectivity of Fractures-Application of Crack-Bridging Theory to the Austin Chalk, Texas: *Tectonophysics*, v. 337, p. 117-133.
- Schwalbach, J. R., and Bohacs, K. M., 1992, Sequence stratigraphy of fine-grained rocks with special reference to the Monterey Formation, *in* *Sequence Stratigraphy in Fine Grained Rocks: Examples from the Monterey Formation*, Society for Economic Paleontologists and Mineralogists Pacific Section, no 70. p. 31-46.
- Schwalbach, J. R., and Bohacs, K. M., 1996, Stratigraphic sections and gamma-ray spectrometry from five outcrops of the Monterey Formation in southwestern California-Naples Beach, Point Pedernales, Lion's Head, Shell Beach, and Point Buchon, *in* Keller, M.A., eds, *Evolution of sedimentary basins-onshore oil and gass investigations-Santa Maria Basin Province*, U.S. Geological Survey Bulletin, p. 21-29.
- Schwalbach, J. R., Gordon, S. A., O'Brien, C, P., Lockman, D. F., Benmore, W. C., Huggins, C. A., 2007, Reservoir characterization of Monterey Formation siliceous shales-tools and applications, Pacific Section AAPG Miscellaneous Special Publication, MP 48.
- Sedlock, R. L., and Hamilton, D. H., 1991, Late Cenozoic tectonic evolution of southwestern California: *Journal of Geophysical Research*, v. 96, no. B2, p. 2325-2351.
- Snyder, W.S., Brueckner, H.K., Schweickert, R.A., 1984, Deformational styles in the Monterey Formation and other siliceous sedimentary rocks, *in* *Stratigraphic, tectonic, thermal, and diagenetic history of the Monterey Formation, Pismo and Huasna Basins*, SEPM Field Guide, no. 2: Society for Sedimentary Geology, p. 151-171.
- Southern California Earthquake Data Center, California Technical Institute, 2013, <http://www.data.scec.org/>

- Sorlien, C., Kamerling, M. J., Mayerson, D., 1999, Block rotation and Termination of the Hosgri strike-slip fault, California, from three-dimensional map restoration: *Geology*, v. 27, no. 11, p. 1039-1042.
- Stanley, K.O., and Surdam, R.C, 1984, The role of wrench fault tectonics and relative changes of sea level on deposition of Upper Miocene – Pliocene Pismo Formation, Pismo Syncline, California, *in* Stratigraphic, tectonic, thermal, and diagenetic history of the Monterey Formation, Pismo and Huasna Basins, SEPM Field Guide, no. 2: Society for Sedimentary Geology, p. 21-35.
- Surdam, R. C., and Stanley, K.O., 1984, Stratigraphic and sedimentologic framework of the Monterey Formation, Pismo syncline, California *in* Guide to the Monterey Formation in the California Coastal Area, Ventura to San Luis Obispo, Pacific Section AAPG, p. 83-91.
- Titus, S. J., Housen, B., Tikoff, B., 2007, A kinematic model for the Rinconada fault system in central California based on structural analysis of *en echelon* folds and paleomagnetism: *Journal of Structural Geology*, v. 29, p. 961-982.
- Underwood, C. A., Cooke, M. L., Simo, J. A., Muldoon, Maureen A., 2003, Stratigraphic controls on vertical fracture patterns in Silurian Dolomite, northeastern Wisconsin: *AAPG Bulletin*, v. 87, no. 1, p. 121-142.
- United States Geological Survey, 2012, Assessment of potential additions to conventional oil and gas reserves in discovered fields of the United States from reserve growth: U.S. Geological Survey fact sheet 2012-3108.
- Vittori, E., Nitchmen, S. P., Slemmons B. D., 1994, Stress pattern from late Pliocene to Quaternary brittle deformation in coastal central California, *in* Alterman, I. B. McMullen, R. B., Cluf, L. S., and Slemmons, D. B., eds., *Seismotectonics of the Central California Coast Ranges*: Boulder, Colorado, Geological Society of America Special Paper 292.
- Wu, H, and Pollard, D. D., 1995, An experimental study of the relationship between joint spacing and layer thickness: *Journal of Structural Geology*, vol. 17, no. 6, p. 887-905.